TDEM-15 Milestone Whitepaper

Threshold raw retrieved contrast in Coronagraphs Is limited by internal polarization

James B. Breckinridge[*], PI and Russell A. Chipman, Co-I
College of Optical Sciences
University of Arizona, Tucson, AZ

April 15, 2017

JPL Document # D-100127

[*] Visiting associate, GALCIT, California Institute of Technology

Signature Page

E-SIGNED by James Breckinridge
on 2017-05-05 14:55:40 GMT

1. James Breckinridge,
Principal Investigator
College of Optical Sciences
University of Arizona
Tucson, AZ. 85719

E-SIGNED by Brendan Crill
on 2017-05-04 21:19:20 GMT

2. Brendan Crill,
Deputy Technology Development Manager
Exoplanet Exploration Program
Jet Propulsion Laboratory
California Institute of Technology
Pasadena, CA, 91109

E-SIGNED by Nicholas Siegler
on 2017-05-04 21:21:39 GMT

3. Nicholas Siegler,
Program Chief Technologist
Exoplanet Exploration Program
Jet Propulsion Laboratory
California Institute of Technology
Pasadena, CA, 91109

E-SIGNED by Douglas Hudgins
on 2017-05-05 01:27:24 GMT

4. Douglas Hudgins
Program Scientist for Programs
Exoplanet Exploration Program
Science Mission Directorate
NASA Headquarters
Washington, DC

3. Table of Contents

4. Objective

The objectives of this TDEM are to provide the science community with

1. A quantitative understanding of the role of polarization in direct imaging exoplanet coronagraphs, including WFIRST-CGI
2. Requirements for the allowable spatial distribution of the vector complex reflectivity and transmissivity for telescope/coronagraph optical systems.
3. Polarization aberration mitigation methodologies and an assessment of contrast levels achievable with coronagraphs on LUVOIR and HabEx.

These objectives will be met by providing answer to these questions:

1. What is the contrast, transmittance, and chromatic aberration we expect from WFIRST-CGI telescope/coronagraph system optical prescription as provided by the flight project.

- The task that will answer this question is called **WFIRST-CGI polarization ray trace**.

2. What are the contrast, transmittance, and chromatic aberration we expect from the LUVOIR and HabEx optical systems as provided by the STDT members?

- The task that will answer this question is called: **Polarization ray trace LUVOIR/HabEx**

3. What is the role of thin film fabrication errors, which are manifest in anisotropic complex reflectivity changes across mirror surfaces on three key performance parameters: contrast, transmittance, and chromatic aberration within imaging telescope/coronagraph systems? Estimate the allowable tolerance to achieve a required contrast, transmittance and chromatic aberration performance?

- The task that will answer this question is called **Characterize form birefringence.**

4. What are the polarization aberration mitigation and balancing approaches that will increase contrast increase transmittance and widen the bandwidth?

- The task that will answer this question is called **ExoPlanet imaging polarization mitigation**

5. Introduction/background

5.1 INTRODUCTION

In this research task, we investigate fundamental technology for the end-to-end optical design and engineering of space-based exoplanet coronagraphs. In particular, the role of polarization aberrations in contrast, bandwidth, and increased transmittance will be investigated. Several space coronagraphs will be polarization ray traced and analyzed. The role of mirror-coating uniformity (form birefringence) on contrast will be investigated. This research is the basis for requirements development of the optical systems and devices for high-contrast ($C>10^{+9}$) space coronagraphy.

These high contrast requirements for exoplanet coronagraphs drive optical system PSF, resolution, and stray light specifications far beyond previous generations of any optical systems. The polarization ray trace algorithms for coatings and other elements, particularly as implemented in commercial software, like Code V and Zemax are relatively new, and may not be thoroughly tested and understood. The interpretation of such polarization aberrations is complicated and has not been widely applied.

In this research task, our team will employ the polarization ray-tracing program, Polaris-M[†], developed by R. Chipman, professor of Optical Sciences at the University of Arizona and Co-I on this research task. This software was designed specifically for polarization analysis of complicated optical systems. This software design tool has been successfully used in several industrial applications[‡]. Polaris-M will be used to analyze the WFIRST coronagraph optical design. In addition, this software will be used to analyze several other coronagraphs, including LUVOIR and HabEx.

We will coordinate our polarization simulations and insights with the WFIRST-CGI and LUVOIR and HabEx technology & science teams. We intend to perform these analyses such that others using different software, such as Code V or Zemax can directly compare our results with the calculation. Our polarization calculations will improve the ExoPlanet program office and the science community's confidence that coating polarization aberrations are correctly simulated. Based on our quantitative analysis and physical measurements we will recommend appropriate measures to increase contrast, bandwidth and transmittance.

An optical system corrected for geometric path difference errors is a necessary but not sufficient condition for the perfect image formation needed to directly image terrestrial exoplanets. Geometric (trigonometric) path difference errors are controlled using adaptive optics (tip-tilt & wavefront), active metrology and precision pointing. However, image quality is also determined by several physical optics factors: diffraction, polarization, partial coherence, and chromatism all of which degrade image quality and are not corrected through the control of geometric path difference. The source of these physical optics errors lies in the vector complex transmittance of masks and stops along with both the thin film coatings needed to obtain high transmittance and the opto-mechanical packaging of mirror surfaces used in the path from the primary mirror to the detector. Adaptive optics corrects wavefront errors described by geometric or optical path length errors caused by mechanical deformations and calculated using

---

[†] Commercial product of Airy Optics (Tucson, AZ.), @ http://www.airyoptics.com/

[‡] Industrial applications are reported here, in section 7. "Facilities"

trigonometry, but not those wavefront errors introduced by physical optics phenomena, which require a vector wave description.

In our work described here, we will integrate three optical-science modeling-tools to accurately predict the performance of space-based terrestrial exoplanet coronagraphs. These are: geometric ray trace, vector wave propagation/diffraction theory and statistical optics.

At least two astronomical science measurement objectives are affected by internal instrument polarization. These are: 1 Exoplanet characterization using coronagraphy and 2 Astrometry. Safonov[1] discovered that internal instrumentally induced polarization causes astrometric systematic errors. Polarization changes the centroid of star positions on an array detector to introduce position measurement errors. For our work described here, we will concentrate on applications to characterize terrestrial exoplanets using space telescopes.

In 1984, Breckinridge[2] first analyzed the use of the Lyot coronagraph to image distant exoplanets and modeled a system using the scalar approximation to the vector electromagnetic wave. They showed how scalar-complex apodization of the exit pupil reveals an exoplanet in the presence of mirror fabrication errors in a simple coronagraph. Breckinridge and Oppenheimer[3] showed that internal polarization, and thus vector E&M plays an important role in exoplanet coronagraphy[4]. Carson[5] provided a measurement of the polarization dependent PSF. Balasubramanian[6] examined a terrestrial planet finder (TPF) coronagraph design using vector electromagnetic (E&M) waves and concluded that for TPF designs vector-waves were not necessary to develop a system to control scattered light to the level required at that time. Breckinridge[7] alerted the WFIRST-CGI science and technology development team to contrast degradation caused by internal polarization.

Today, ground and space exoplanet coronagraphs are designed and built under the assumption that the scalar wave approximation to the vector electromagnetic wave[8,9] is adequate. Recently, Breckinridge[10] and Chipman[11] used vector E&M wave analysis with the polarization aberration tools developed by Chipman and others to model point-spread functions (PSF) for astronomical telescopes. They discovered that several physical optics effects are in reality very important for the design of high performance coronagraphs. In fact, these effects limit both contrast and system exoplanet yield.

The space-based exoplanet coronagraph performance requires an accurate end-to-end (object to detector) optical system reference model to guide science & program office decisions, technology development and also, to direct the optical system engineering needed to balance subsystem requirements and to define system ground & space calibration methodologies. This accurate model requires a comprehensive set of geometrical and physical optics tools along with an understanding of the physical interaction of incoherent, white-light (optical E&M) with matter (dielectrics and metals), and an appreciation for the role of partial coherence in image formation and knowledge of digital processing of speckle patterns.

Figure 1 below shows a schematic of the optical path or "circuit" for a typical Lyot coronagraph. Incoherent white-light from the primary star and its exoplanets, enters the optical system from the left and passes through the Fore-optics of the system which contain the primary and secondary mirrors, the A/O mirrors necessary to form the "dark-hole" at the detector plane and the fold mirrors needed to package the instrument into a volume to fit into a spacecraft. The region the fore-optics occupies is identified by the symbol **A**. This fore-optic system relays the white-light incoherent object space irradiance distribution, typically a star on axis onto a complex occulting mask located at a system image plane and positioned to mask or occult the bright parent star of the system understudy. There is no detector at this image plane to record the modulus squared of the field. It is the complex filed itself that is of importance. The off-axis exoplanet light (complex field) passes around the mask to continue through the system. The occulting mask has a complex transmittance indicated by **B**. Light from the star is attenuated by the complex transmittance of this occulting mask. Light passes through that

section of the post-optics, labeled **C** in Fig 1 before the Lyot stop at **D**. The Lyot stop is a complex apodizer located at an image of the primary and is used to control the phase and amplitude of the complex EM field that is diffracted around the sharp edge of the primary mirror, secondary support shadows and in the case of a segmented primary mirror, the segment gaps. After the Lyot stop the radiation reflects from the several mirrors needed for packaging into the spacecraft as it passes through region **E** of the post optics to strike the detector. The detector responds to intensity. The spatial distribution of the complex electric field at this plane is not recorded directly. The modulus squared of the field is recorded to represent the intensity image.

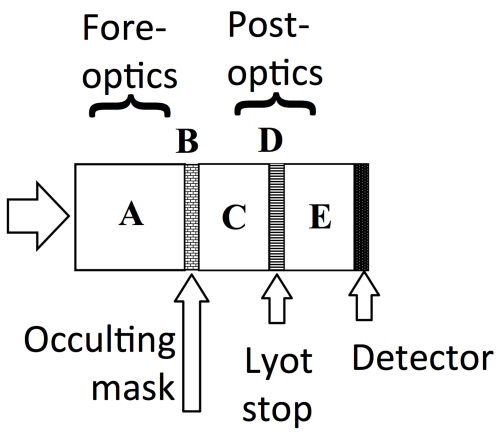

Figure 1. Optical schematic or circuit for a typical Lyot coronagraph. The source is to the left and light passes through regions A, B, C, D, and E before the detector absorbs it, where the modulus squared of the resulting field is recorded.

This work will significantly advance the state-of-the-art in polarization measurements and coatings for high performance optics. Space telescope mirrors have never been characterized to such levels against coating conditions. Several NASA programs that require high contrast and polarization preserving optics will benefit from this study. Physical optics, astronomical sciences and material sciences will all gain knowledge from this work.

The content of this white paper provides: 1. The physics background needed to understand image formation in high-contrast exoplanet coronagraphs and the role of white-light vector-wave E&M in image formation within exoplanet coronagraphs and 2. An outline of the work planned during the next 2 years under NASA Grant # NNX17AB29G for "Threshold raw retrieved contrast is limited by internal polarization" awarded to Dr. James Breckinridge (PI) and Dr. Russell Chipman (Co-I) at the College of Optical Sciences of the University of Arizona, Tucson.

5.2 BACKGROUND

5.2.1 Exoplanet optical imaging system coronagraph (EISC)

This section describes image formation in an ideal exoplanet imaging system coronagraph (EISC) to establish a basis for understanding optical image formation in the more complicated instruments needed for space instruments. Figure 2 shows the schematic of an ideal coronagraph optical system.

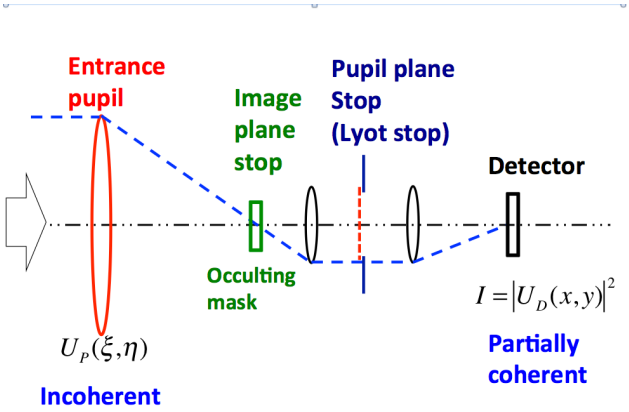

Figure 2. Optical schematic for a typical exoplanet optical imaging system coronagraph (EISC). The Star/planet complex electromagnetic field enters the system horizontally from the left and is focused onto a complex occulting mask located at an image plane stop. This image plane stop is at the front focus of a collimator lens. The optical power on the collimator is such that an image of the entrance pupil field is formed on the Lyot stop. The field is then focused on to the detector. Additional optics (not shown), in particular a pair of adaptive optics elements are inserted before the occulting mask to create a dark hole and the complex wavefront reflects from the several mirrors in the end-to-end optical path needed to package the system for flight.

The optical system shown in figure 2 is an abstract construct useful to describe the basic functions of a coronagraph but does not reflect the reality of a space-flight optical system. In the real world, the complex (real and imaginary part) electromagnetic field (wave) propagates from the left in Fig 2 through the entire flight-hardware build optical system comprised of many tilted fold mirrors and curved optical elements to the focal plane. At the focal plane the detection process records the modulus squared of the product of the amplitudes of the wavefronts that represent the complex vector electric fields and the sum of the phases of the wavefronts to create the intensity image recorded by an array detector. By the time this complex field arrives at the detector plane it exhibits partial temporal and spatial coherence. During propagation through the optical system the complex wavefront interacts with several highly reflecting metal surfaces, dielectric surfaces, windows, optical filters and the dispersive optics needed to produce a spectrum.

A few of the ways the optical system shown in Fig 2 differs from a real-world optical system are: 1. The powered optical element to the left is a curved metal mirror, 2. Often the flight packaging requirements will place several metal and dielectric surfaces between the curved optical element and the complex occulting mask, and 3. The masks and stops used to control unwanted radiation manipulate the complex (both real and imaginary) wavefront at image and pupil planes.

We will learn that each physical realization of a real-world exoplanet coronagraph needs to be analyzed for the effects of the sequence of optical elements, the mirror tilt angles along with their coatings and filters and re-optimized with its masks and stops to achieve the contrast needed for terrestrial exoplanets.

5.2.2 Geometric ray-trace (trigonometry) design

Classical geometric ray-trace (trigonometry) optical design[12,13,14,15,16] is used initially in the design process to calculate surface curvatures, separations and optical path ray-lengths. It provides information on image location, size and orientation as well as image brightness (through the calculation of étendue). The objective of all geometric ray trace design computer

programs is to minimize optical path length (OPL) errors among the set of rays that map a point from object space through the optical system onto a point in image space. Geometric ray trace provides the optical prescription for the manufacture of surfaces, the optomechanical surface separation, the mechanical fixtures and the fabrication and assembly tolerances. These tolerances form the basis of the thermal, structural and mechanical engineering of the instrument. Geometric ray-trace design provides little direct information about image quality and no information about the coherence of wavefronts, polarization or scattering from surfaces & coatings that affect characterization of terrestrial exoplanets.

Geometric ray-trace design provides information insufficient to estimate contrast & SNR for exoplanet characterization. Below we show that the analysis tools of physical optics are needed to provide an estimate of contrast and that the analysis tools of statistical optics are needed to provide an estimate of SNR.

5.2.3 Scalar-wave optical image formation (diffraction)

Maxwell[17] showed that all radiation could be represented as a vector electromagnetic wave. Many textbooks simplify the need to consider light in this more complicated vector form by making a scalar wave assumption. This assumption is useful to estimate the angular resolution of most space-based imaging systems. However, it fails to accurately describe high-performance space-based exoplanet characterization optical systems such as the WFIRST-CGI, LUVOIR and HabEx.

- **Fourier Transform relationship**

An analysis of optical systems using scalar waves provides an estimate of angular resolution. Goodman[18] derives the Fresnel-Kirchoff diffraction integral and invokes scalar wave theory to reveal those physical optics conditions that lead to the existence of a Fourier transform relationship between the electric field at the exit pupil and the electric field at an image plane.

Object space irradiance distribution can be decomposed into an ensemble of delta functions. The intensity or height of each delta function maps out the structure of the object. The optical system operates on the complex amplitude and phase associated with that intensity to form an image at the detector. Astronomical sources in the visible region of the spectrum radiate broadband, incoherent thermal light.

The theory of image formation is developed using the schematic shown in Figure 3 below, where we define the coordinate system. These coordinates are in standard use by modern textbooks[18,19] on the physics of optical image formation. The object plane, #1, is represented by Cartesian coordinates from the Latin alphabet x_1, y_1 and the pupil plane, #2, is represented by Cartesian coordinates from the Greek alphabet ξ_2, η_2 and the image plane, #3, is represented by Cartesian coordinates from the Latin alphabet x_3, y_3.

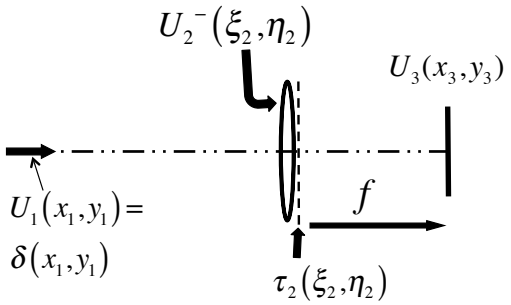

Figure 3 schematic of an optical system in the meridional plane. The object space complex field $U_1(x_1,y_1)$ is shown as a delta function $\delta(x_1,y_1)$ to represent a star on-axis. This object space field is propagated by Fresnel diffraction to just to the left of the entrance pupil and is shown by $U_2^-(\xi_2,\eta_2)$. The pupil is shown to have a complex transmittance $\tau_2(\xi_2,\eta_2)$ at plane 2. The optical system, shown here schematically has a lens of focal length f, and provides the optical power to create the field $U_3(x_3,y_3)$ at an image plane 3. This notation will be used in the text throughout this document.

The scalar complex amplitude and phase across the image plane is found by standing at the image plane (#3) in Fig 3 and looking to the left, or back through the system toward the object. The Fresnel-Kirchoff diffraction integral is used to model the propagation of scalar electromagnetic waves through the optical system shown in Fig. 3. The complex amplitude and phase field $U_3(x_3,y_3)$ at an image plane is given by

$$U_3(x_3,y_3)= \\ \mathrm{K}\int_{-\infty}^{\infty}\int_{-\infty}^{\infty}[U_2^-(\xi_2,\eta_2)]\cdot\tau_2(\xi_2,\eta_2)\cdot\exp\left\{-i\frac{2\pi}{\bar{\lambda}f}(x_3\xi_2+y_3\eta_2)\right\}d\xi\,d\eta \qquad \text{Eq. 1}$$

Where K is a constant, the integral is taken over the complex field as it appears across the exit pupil, $U_2^-(\xi_2,\eta_2)$ of the optical system whose focal length is f and $\bar{\lambda}$ is the quasimonochromatic wavelength of light. Eq 1 is written for scalar wave diffraction, which is a solution to Maxwell's equations and the not vector wave solution to Maxwell's equation. The amplitude and phase complex properties across the exit pupil are contained in the scalar transmittance term,

$$\tau_2(\xi_2,\eta_2)=A_2(\xi_2,\eta_2)\exp\{i\phi_2(\xi_2,\eta_2)\} \qquad \text{Eq. 2}$$

Where $A_2(\xi_2,\eta_2)$ varies between 0 and 1 and describes amplitude part of the complex wave as a function of position across the exit pupil. The phase properties (0 to 2π) at each point across the exit pupil are described by $\phi_2(\xi_2,\eta_2)$.

To the left in Fig 3, we have a point source represented by a delta function. This point source is mapped onto the image plane. We record intensity at the detector plane and define the detector plane irradiance distribution for this point source to be given by the Point Spread Function (PSF):

$$PSF \equiv \left|U_3(x_3, y_3)\right|^2, \qquad \text{Eq. 3}$$

Where $U_3(x_3, y_3)$ is given by Eq. 1.

Next if we let the object space irradiance be represented by $I_{\text{Object}}(x_1, y_1)$ and the image space irradiance represented by $I_{\text{Image}}(x_3, y_3)$ and use the theoretical development of Goodman[17], we write,

$$I_{\text{Image}}(x_3, y_3) = I_{\text{Object}}(x_1, y_1) \otimes PSF, \qquad \text{Eq. 4}$$

where the symbol $\otimes$ denotes the convolution operator and we have assumed the system to be linear in intensity. This analysis reviews the classical scalar approach to modeling linear, spatially invariant optical systems.

- **Linear system**

Equations 1 through 4 above are written under the assumption that our system is linear in complex field. If object space contains N sources, then image space contains N sources. If we multiply that number in object space by k, the number in image space is multiplied by k. We will learn below that exoplanet coronagraphs are not linear systems in this sense.

- **Light is a vector**

The development above is for a scalar representation of the electro-magnetic field. The correct solutions to Maxwell's equations require vector representations of electro-magnetic radiation. In a real-world optical system light reflects from tilted mirrors and dielectric surfaces. These surfaces cause polarization changes across the surface of the wavefront. What effects these changes have on the PSF are discussed in the next section.

Most astronomical sources are unpolarized. However, once the unpolarized radiation enters the telescope and light is concentrated to form an image within the volume of the telescope, the quality of that image is determined by internal instrument polarization, as we show in the next section.

5.2.4 Failure of scalar-wave theory

An experiment using linear orthogonal polarizers and a telescope shows the role of vector waves in image formation. Image formation is a phenomenon of interferometry. Figure 4 shows the effects of adding polarizers to an optical system: Top left shows an open, unmasked exit pupil of a telescope with zero geometric wavefront error. Top right shows the shape of the PSF recorded with the pupil on the top left. Bottom left shows the same telescope pupil as that shown in the upper left, with two linear polarizers over the top, one aligned orthogonally to the other. Horizontally polarized light is admitted to the left-hand side of the pupil and vertically polarized light is admitted to the right-hand side of the pupil. The bottom right shows the PSF recorded using the pupil on the bottom left. Note that with no polarizer the angular resolution is not position-angle dependent, however, with the polarizer the angular

resolution is position angle dependent. That is, with no polarizer, the angular resolution, or inner working angle (IWA) is given by the standard Airy diffraction pattern and independent of azimuth angle on the sky. In the lower pair, we see the resolution is higher in the vertical direction than in the horizontal direction. For the image in the lower right, the IWA is less in the vertical direction that it is in the horizontal.

Figure 4 PSF's shown for a telescope with zero geometric wavefront aberration without (upper) and with (lower) polarizers.

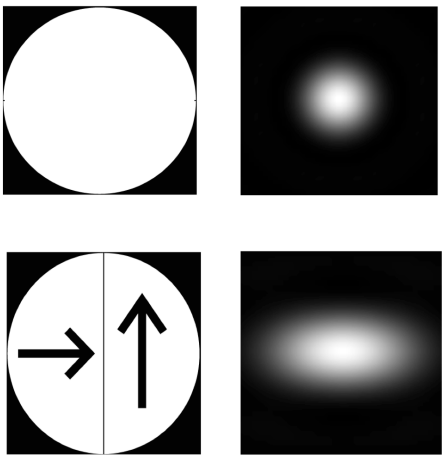

It is well-known that orthogonally polarized light does not interfere to create fringes at the detector. In Fig 4, the lower left image of the exit pupil the polarized radiation from the left portion of the exit pupil does not interfere with the orthogonally polarized radiation from the right portion of the exit pupil. Therefore, the PSF is elongated in the horizontal direction. In this case the PSF is the scalar sum (linear superposition) of two images from a "D" shaped aperture, not the vector sum across the circular aperture shown in the upper right panel in Fig 4. In Fig 4, we see that the inner working angle is larger in the horizontal direction than it is for the vertical direction.

Astronomers define position angle as the rotation angle in the plane of the sky, or in this case the plane of object space. The upper right in Figure 4 shows that the angular resolution is the same in all directions from the axis, whereas the lower right in Figure 4 the angular resolution is not the same in all directions from the system axis. Resolution in the horizontal direction is less than that in the vertical direction. This means that a coronagraph mask positioned at the image plane that is designed using scalar theory and applied to a system with polarization aberrations (like WFIRST-CGI), would leak large amounts of light around the occulting mask to flood the coronagraph and block light from exoplanets to reduce exoplanet yield.

Although this is a rather dramatic example and no one would intentionally place orthogonal linear polarizers over their telescope pupil, this shows that any source of polarization change across the exit pupil will result in distortion of the PSF at some level and result in light leakage around those occulting masks that are now designed using scalar theory only.

In the next section, we identify sources within the telescope/coronagraph optical system that polarize light. Current astronomical science measurement objectives require high transmittance optical systems, which in turn require high reflectivity broad-band optical thin films. As the white-light electromagnetic wave propagates through the optical system, reflecting from low absorption metal mirrors it becomes partially polarized. The Fresnel polarization equations give the magnitude and sign of this polarization and are described in the following section.

5.2.5 Vector waves & polarization aberrations

- **Fresnel polarization**

Here we examine the source of the phase and amplitude changes that occur across the wavefront within astronomical telescopes and instruments. Systems require mirrors coated with metals (e.g. Al or Ag) to give high surface reflectance and thus maximize system transmittance. These mirrors are overcoated with a dielectric material that serves two purposes: 1. It forms a transparent mechanical barrier coat to inhibit oxidation and surface abrasion 2. The coating enhances the reflectivity at select wavelengths. In the next section, we show that it is the metal surfaces, required from broadband high reflectivity that partially polarizes light. These dielectric overcoats contribute by either adding to or subtracting from the polarization aberrations caused by the metal mirror. Dielectric coatings add a degree of complexity that will affect coronagraph contrast and the inner working angle (IWA), and are not discussed further in this whitepaper other than to mention they can be used to a limited extent to mitigate polarization aberrations over a narrow bandwidth in real optical systems[20]. However, during the course of this work the effects of dielectric coatings on telescope/coronagraph system performance will be examined in detail as part of milestone # 1 described on page 48. The coatings which are specified in the design will be considered.

In figure 4, above we saw that the change in polarization across the exit pupil affects image quality. Broadband unpolarized white-light is a characteristic of nearly all-astronomical sources. Others have shown[21] that unpolarized (incoherent) white light can be divided equally into two orthogonally polarized beams. Here, we represent unpolarized light by two orthogonal Eigenvector states and, for convenience we select two orthogonal *linearly* polarized Eigenvector states.

In figure 5, below we show a beam of light (yellow) incident at an angle from the normal onto a typical astronomical mirror, which is a dielectric overcoated metal mirror. Radiation reflects off the surface at an angle given by Snell's law and a portion of the radiation is absorbed into the metal.

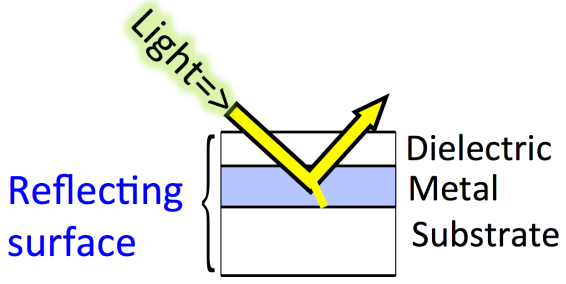

Figure 5 Unpolarized white-light strikes the mirror surface from the upper left and reflects up to the right according to Snell's law. A transparent dielectric overcoat is shown on top of the thin isotropic metal film, which has been deposited upon a substrate. The light penetrates the overcoat to strike the mirror and is partially absorbed before reflecting. Both the amplitude and phase are changed upon this absorption and the reflected radiation is partially polarized to change both amplitude and phase.

A-J Fresnel in 1823 described the theory for interactions of electromagnetic radiation with dielectrics and metals. The Fresnel equations[22,23] are used to model the behavior of a vector electromagnetic complex wave interacting with a homogeneous metal or dielectric surface (mirror). These relationships were developed further[24] and are the basis of the commercial field of ellipsometry[25]. Here we describe those relationships. Figure 6 below shows the coordinate system we will use.

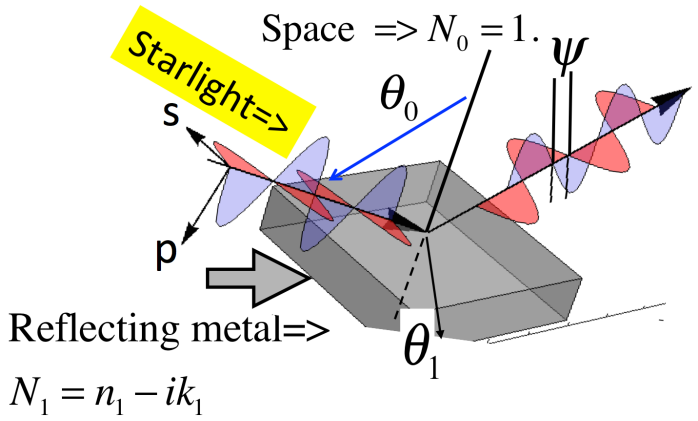

Figure 6. Broadband white-light (shown as yellow) traveling in free space ($N_0 = 1$) passes from the left downward to the right to strike a metal mirror, which has a complex index of refraction of $N_1 = n_1 - ik_1$ at angle of incidence θ_0. The incident, incoherent white-light is represented and decomposed into two orthogonal Eigenstates: parallel and perpendicular. The absorbed wavefront passes into the metal at a complex angle of refraction of θ_1. The incident light polarized perpendicularly to the plane of incidence is retarded, upon reflection by angle ψ, and the amplitude of the incident light is different upon reflection for each polarization state.

Consider incoherent white-light incident at angle θ_0, onto a metal mirror with isotropic properties. This homogeneous metal mirror has a wavelength dependent complex index[22] $N_1(\lambda) = n_1(\lambda) + ik_1(\lambda)$. Here we consider a perfectly homogeneous mirror and that $N(\lambda)$ does not change at different points across the surface. In reality the mirror fabrication process introduces anisotropic properties within the thin film mirror. The effect of anisotropy on terrestrial exoplanet coronagraphy is discussed in section 5.2.9 below and will be measured, for the first-time, as part of this effort.

The Eigenstates of reflection are the s (perpendicular) and p (parallel) polarized components. A portion of the beam reflects at the incidence angle θ_0 (Snell's Law) and another portion (a damped evanescent wave) penetrates a short distance into the metal at the **complex** refraction angle of θ_1 given by Snell's law[25] and is absorbed to heat the metal. This complex angle is given by

$$\theta_1 = \arccos\left\{\left(\sqrt{N_1^2 - N_0^2 \sin\theta_0^2}\right) / N_1\right\} \qquad \text{Eq. 5}$$

The complex reflectivities for light in the p and s polarizations are given by[33]

$$r_p = \frac{\tan(\theta_0 - \theta_1)}{\tan(\theta_0 + \theta_1)} \text{ and } r_s = \frac{\sin(\theta_0 - \theta_1)}{\sin(\theta_0 + \theta_1)} \qquad \text{Eq. 6}$$

Two polarization effects occur. 1. A phase shift and 2. A polarization-dependent absorption.

- **Phase shift - retardance**

Recall that each point (x,y) in object space maps into an array of points (ξ,η) in the exit pupil, and that unpolarized white-light can be decomposed into two linear orthogonal polarizations. Upon interaction of the incident beam with matter (mirrors) phase shift occurs between the two waves associated with each of the orthogonal polarizations. We use the notation $\psi(\xi,\eta)$ to express the angle of retardance of the s-polarized light relative to the p-polarized light for points ξ,η across the exit pupil. Equation 7, below, defines this polarization aberration we call retardance, $\psi(\xi,\eta)$.

$$\tan\psi(\xi,\eta) = \tan\left[\phi_s(\xi,\eta) - \phi_p(\xi,\eta)\right] = \left|r_s(\xi,\eta)\right| / \left|r_p(\xi,\eta)\right|. \qquad \text{Eq. 7}$$

Where (ξ,η) are coordinates across the pupil. And we see that we allow the retardance phase ψ to vary across the pupil ξ,η. We will find that this affects image quality.

- **Polarization dependent absorption - diattenuation**

The reflectivity is polarization dependent, with the result that reflection acts as a partial polarizer. The term diattenuation is used to remind us that there are two ("Di") measurements required here. The diattenuation, *D* at each point (ξ,η) across the pupil is given by

$$D(\xi,\eta) = \frac{\left|r_s(\xi,\eta)\right|^2 - \left|r_p(\xi,\eta)\right|^2}{\left|r_s(\xi,\eta)\right|^2 + \left|r_p(\xi,\eta)\right|^2} \qquad \text{Eq. 8}$$

Where *r* is the **complex** reflectivity for *s* and *p* light respectfully given in Eq 6 above. Metallic reflection acts as a weak polarizer, and *D* varies from zero (nonpolarizing) to one for ideal polarizers. Astronomical optical systems require large étendu (area times solid angle), which requires large area optics. However, the volume for spacecraft bus is required to be compact to fit inside launch shrouds. These two requirements conflict and often lead to many fold mirrors in the instrument which, unless designed properly will, in turn, lead to large internal polarization with the concomitant loss in transmission, caused primarily by diattenuation and loss in image quality, caused primarily by retardance.

Note there are two polarization aberrations: 1. Diattenuation is commonly used to model a polarization dependent reflectivity and 2. Retardance is used to model a polarization dependent change in the phase of the complex wave upon reflection. In the next section where we look at how an actual space instrument (telescope and coronagraph) differs from the theoretical discussion here. We will learn that the physical reflecting surfaces, which are

illuminated by light passing through the optical system exhibit both phase ψ and polarization reflectivity (r_s *and* r_p) changes across the these surfaces. This is particularly true of very large area primary mirror. This is a natural result of the way in which telescope and instrument mirrors are processed. The extent to which this phenomenon, called form birefringence affects contrast and SNR remains unknown and will be investigated as one of the tasks described here.

To summarize, our new approach, needed for high contrast optical systems is to model white-light electromagnetic radiation as a vector. To understand the need for vector-wave physical optics, we have reviewed the source of polarized light within an optical system and understand the complex (amplitude and phase) wavefront at the focal plane $U_3(x_3, y_3)$ where coronagraphers place the occulting mask to control scattered light to one part in 10^{11}. Correct design of the optimum occulting mask requires our new vector E&M approach.

Given a flat mirror coated with bare aluminum and illuminating it with polarized white-light we use the Fresnel equations given by Eqs. 6 and 8 to calculate the reflectivity and retardance as a function of angle. Figure 7 below shows (left panel) amplitude reflectivity as function as a function of angle of incidence for both s and p polarized light and in the right panel we see the phase change (retardance) as a function of angle of incidence for both s and p polarized light.

- Reflectivity changes with angle

Figure 7 left below shows a plot from Eq. 6 above, assuming an isotropic aluminum metal film. This is the amplitude reflection coefficient for s-light (light polarized perpendicular to the plane of incidence), shown as a solid line and also the amplitude reflection coefficient for p-light (light polarized parallel to the plane of incidence), shown as the dotted line. Figure 7 right below shows a plot using Eq. 7, assuming an isotropic aluminum metal film. The phase change upon reflection in radians is shown for s-light (light polarized perpendicular to the plane of incidence), and the phase change upon reflection in radians is shown for p-light (light polarized parallel to the plane of incidence).

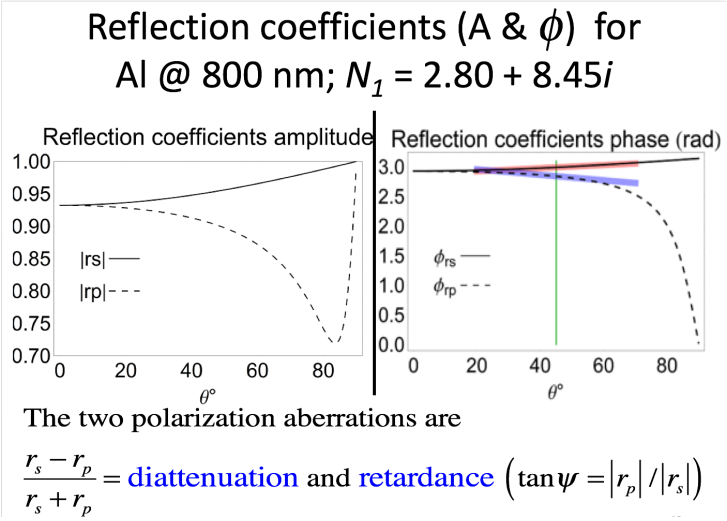

Figure 7 amplitude reflection coefficients and phase changes as a function of incidence angle for a bare Al coating at 800nm wavelength where we find the complex index of refraction to be given by N=2.80+8.45i.

- **Complex refractive index varies across mirror surfaces**

Equations 5 for θ_1 and 6 for the complex reflectivities r_s and r_p above are written assuming that the complex refractive index does not vary across the surface of telescope and instrument optics. That is, we have assumed that the electronic response of the optics to light in the 10^{+14} Hz range is perfectly isotropic. This assumption is adequate for classical optical design and engineering of ground and space instruments. However, to meet the high (10^{-11}) contrast requirement for terrestrial exoplanet characterization requires that we examine coating anisotropies and their effects on contrast and exo-planet characterization.

In section 5.2.9 we examine changes in complex refractive index across the surface of mirrors and look at $N(\xi,\eta) = n(\xi,\eta) + ik(\xi,\eta)$

5.2.6 How the space coronagraph differs from Lyot's coronagraph

Figure 2 (above) shows an optical schematic for a basic imaging system coronagraph. Figure 2 is based on the work of Bernard Lyot[26], who in 1934 designed the first ground-based coronagraph (a refracting system), which he applied to successfully image the solar corona outside eclipse. In this section, we look at how a "real-world" space instrument exoplanet imaging coronagraph needs to be designed to provide broad wavelength band (needs mirrors) to fit into the small volume provided by a spacecraft bus. A modern space instrument is the WFIRST-CGI whose spaceflight engineered optical system is shown in Figure 8, below.

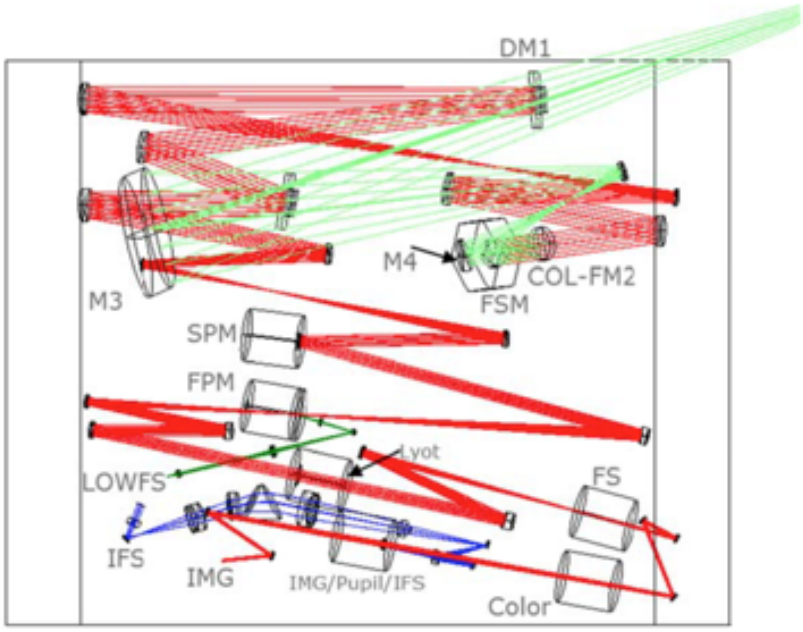

Figure 8. Copy of published sketch of the all-reflecting WFIRST-CGI baseline optical system[75] showing fold mirrors before the image plane. Counting the primary and secondary there are 18-reflections before the image plane occulting mask.

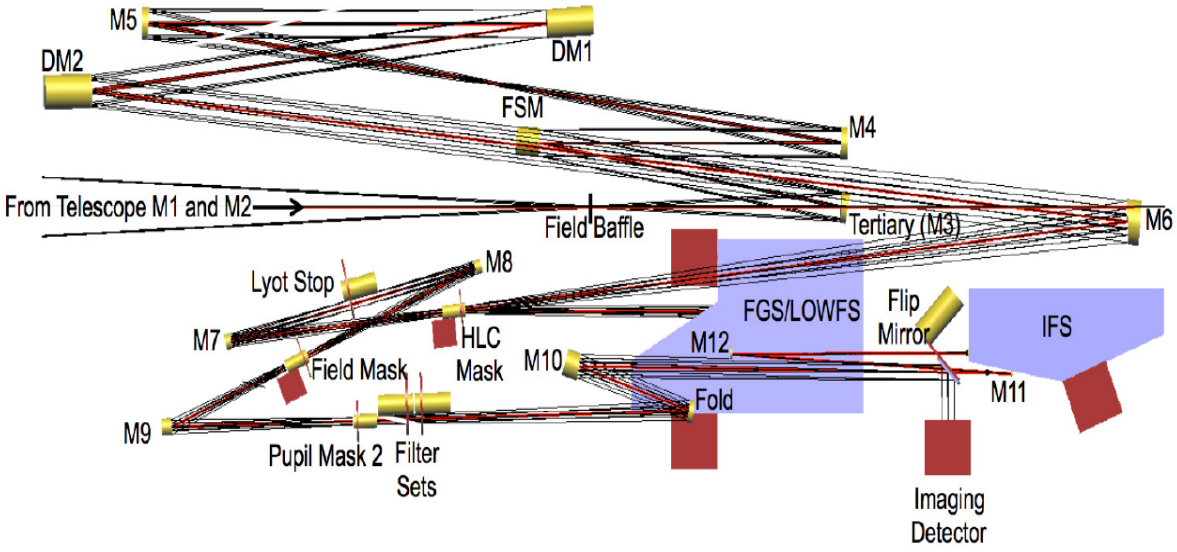

Figure 9. Drawing of the optical system of the Exo-C coronagraph system showing the 9-reflections before the image plane mask. From Exo-C STDT Final Report March 2015 page 5-7 Figure 5.5-1.

The space flight optical systems shown in Figs 8 and 9 differ from the system used by Bernard Lyot in several ways: curved and tilted flat metal mirrors overcoated with dielectrics, two coated metal mirrors in the A/O system, complex mask and Lyot stop. The opto-mechanical layouts are nearly co-planar and therefore the output will be strongly linearly polarized. The sources of internal polarization are far greater in space optics for exoplanet exploration than they are in the simple all refractive 3-surface coronagraphs used by B. Lyot[26].

5.2.7 Image formation in the presence of polarization

- **Vector wave image formation**

If the source is partially polarized and the telescope has (as we know) a polarization dependent transmission, then Eq. 1 is written (in its vector form) as:

$$\vec{U}_3(x_3,y_3) = \left. \mathrm{K}\int_{-\infty}^{\infty}\int_{-\infty}^{\infty}[\vec{U}_2^{-}(\xi_2,\eta_2)\vec{\tau}_2(\xi_2,\eta_2)]\cdot\exp\left\{-i\frac{2\pi}{\bar{\lambda}f}(x_3\xi_2+y_3\eta_2)\right\}d\xi\,d\eta \right\} \quad \text{Eq. 9}$$

Where we allow the both the electric field to the left of the powered optical element (the star and planet) in Fig 2 to be a vector $\vec{U}_2^{-}(\xi_2,\eta_2)$ as well as the spatially dependent transmittance, $\vec{\tau}_2(\xi_2,\eta_2)$.

The complex wavefront for unpolarized, incoherent astronomical sources become partially polarized upon propagation through an astronomical telescope and instrument that contains metal mirrors and dielectric surfaces. A Jones matrix[18,19] whose values change for different ray-paths across the exit pupil describes this wavefront. This spatially dependent matrix is called the Jones pupil[27] and we write this short hand for the complex field at each point (ξ,η) across the exit pupil:

$$\begin{bmatrix} A_{XX}(\xi,\eta)e^{i\phi(\xi,\eta)_{XX}} & A_{XY}(\xi,\eta)e^{i\phi(\xi,\eta)_{XY}} \\ A_{YX}(\xi,\eta)e^{i\phi(\xi,\eta)_{YX}} & A_{YY}(\xi,\eta)e^{i\phi(\xi,\eta)_{YY}} \end{bmatrix} = \begin{bmatrix} J_{XX} & J_{YX} \\ J_{XY} & J_{YY} \end{bmatrix}_{\xi,\eta} \quad \text{Eq. 10}$$

Where the Jones matrix contains complex (amplitude and phase) elements.

On the LHS of Eq. 10, A is amplitude and ϕ is phase of the electric field for each of the 4 component waves in an arbitrarily selected X, Y Eigen basis-set at points ξ,η across the exit pupil. Subscript XX refers to the complex field exiting polarized in X resulting from the incident field with X polarization, as matrix multiplication would imply. A similar convention extends to the subscripts YY, YX and XY. Ideally, the Jones pupil would be the identity matrix for all ray paths and no undesired polarization change would occur[27]. That is, the off-diagonal elements in the matrix shown in Eq.10 would be zero. During image formation with incoherent light, none of these four Jones pupil components form interference fringes with each other[27,28]. Each is diffracted separately by scalar diffraction theory to calculate the four components of the amplitude response matrix, which is the generalization of the amplitude response function of diffraction theory[29].

The vector transmittance of the telescope $\vec{\tau}_2(\xi_2,\eta_2)$ at each point ξ_2,η_2 in the exit pupil is written as,

$$\vec{\tau}_2(\xi_2,\eta_2) = \begin{bmatrix} J_{XX}(\xi_2,\eta_2) & J_{YX}(\xi_2,\eta_2) \\ J_{XY}(\xi_2,\eta_2) & J_{YY}(\xi_2,\eta_2) \end{bmatrix} \equiv \begin{bmatrix} J_{XX} & J_{YX} \\ J_{XY} & J_{YY} \end{bmatrix}_{\xi,\eta} \quad \text{Eq. 11}$$

Note that in Eqs 10, 11 & 12 we allow for the spatial anisotropy of deposited metal thin films. This aspect is discussed in section 2.9 below.

The telescope/coronagraph system complex transmittance across the exit pupil depends on the vector of the electromagnetic field at point ξ,η within the exit pupil. The complex electric field $u_3(x_3,y_3)$ at the image plane, for an on-axis unpolarized star of unit brightness follows from the Fresnel Kirchoff diffraction integral and is written:

$$\left.\begin{aligned} &u_3(x_3,y_3) = \\ &K\left\{\int_{-\infty}^{\infty}\int_{-\infty}^{\infty}\begin{bmatrix} J_{XX} & J_{YX} \\ J_{XY} & J_{YY} \end{bmatrix}\exp\left(-i\frac{2\pi}{\lambda f}\left[x_3\xi_2 + y_3\eta_2\right]\right)\right\}d\xi d\eta = \\ &K\left\{\int_{-\infty}^{\infty}\int_{-\infty}^{\infty}\left(J_{XX}+J_{YY}+J_{YX}+J_{XY}\right)\exp\left(-i\frac{2\pi}{\lambda f}\left[x_3\xi_2 + y_3\eta_2\right]\right)d\xi d\eta\right\} \end{aligned}\right\} \quad \text{Eq. 12}$$

Where *K* is a constant and we assume that the optical power of the system is not vector (polarization) dependent. We have multiplied out the matrix to emphasize that that each of

these 4 terms is independent and not correlated with any other of the four terms. To calculate the intensity $I_3(x_3,y_3)$ that we will measure, we take

$$I_3(x_3,y_3)=\left|u_3\left(x_3,y_3\right)\right|^2 \ . \qquad \text{Eq. 13}$$

From Eqs 12 & 13, we find the detector plane spatial intensity distribution to be

$$I_3(x,y)= \\ =\left|u_3(x,y)\right|^2=\left|K\left\{\int_{-\infty}^{\infty}\int_{-\infty}^{\infty}\left(J_{XX}+J_{YY}+J_{YX}+J_{XY}\right)\exp\left(i-\frac{2\pi}{\lambda f}\left[x_3\xi_2+y_3\eta_2\right]\right)d\xi d\eta\right\}\right|^2 \qquad \text{Eq. 14}$$

Since we are observing a star, which is a thermal broadband white-light source, it is reasonable to assume that the complex electric fields given by J_{XX}, J_{YY}, J_{YX} and J_{XY} are statistically uncorrelated and therefore incoherent[27,28]. The cross-product terms within the modulus squared shown in Eq 14 are therefore zero. Consequently, Eq. 14 can be expanded to give,

$$\begin{aligned} &I_3(x_3,y_3)= \\ &K^2\left|\int_{-\infty}^{\infty}\int_{-\infty}^{\infty}J_{XX}\exp\left(-i\frac{2\pi}{\lambda f}\left[x_3\xi_2+y_3\eta_2\right]\right)\right|^2 d\xi d\eta+K^2\left|\int_{-\infty}^{\infty}\int_{-\infty}^{\infty}J_{YY}\exp\left(-i\frac{2\pi}{\lambda f}\left[x_3\xi_2+y_3\eta_2\right]\right)\right|^2 d\xi d\eta+ \\ &K^2\left|\int_{-\infty}^{\infty}\int_{-\infty}^{\infty}J_{YX}\exp\left(-i\frac{2\pi}{\lambda f}\left[x_3\xi_2+y_3\eta_2\right]\right)\right|^2 d\xi d\eta+K^2\left|\int_{-\infty}^{\infty}\int_{-\infty}^{\infty}J_{XY}\exp\left(-i\frac{2\pi}{\lambda f}\left[x_3\xi_2+y_3\eta_2\right]\right)\right|^2 d\xi d\eta \end{aligned} \qquad \text{Eq. 15}$$

And we see that we have four point-spread functions, one each for the uncorrelated complex scalar fields J_{XX}, J_{YY}, J_{YX} and J_{XY} and the detector plane point spread function is the linear, incoherent superposition of four PSF's as shown in Eq. 16 below.

$$I_3(x_3,y_3)=\underline{I_3(x_3,y_3)}\Big|_{XX}+\underline{I_3(x_3,y_3)}\Big|_{YY}+\underline{I_3(x_3,y_3)}\Big|_{YX}+\underline{I_3(x_3,y_3)}\Big|_{XY} \qquad \text{Eq. 16}$$

The subscript XX means X light entering the system polarized in the X direction mapped into the X direction or X<=X, and similarly for light in the Y direction. The subscript XY refers to light entering the system polarized in the Y direction that exits the system in the X direction. Note that at the focal plane the terms $\underline{I_3(x_3,y_3)}\Big|_{XX}$ and $\underline{I_3(x_3,y_3)}\Big|_{XY}$ are intensities polarized in the X direction and that the terms $\underline{I_3(x_3,y_3)}\Big|_{YY}$ and $\underline{I_3(x_3,y_3)}\Big|_{YX}$ are intensities polarized in the Y direction.

5.2.8 Polarization ray trace (PRT) and polarization aberration theory (PolAbT)

- **Polarization ray trace (PRT)**

Polarization ray tracing (PRT) is a technique for calculating the polarization matrices for ray paths through optical systems[30,31,32,33,34,35]. Polaris-M[36] was built from the ground up to calculate polarization effects in optical systems. It is based on a 3x3 polarization ray tracing calculus[36]. Diffraction image formation of polarization aberration (PolAb) beams is then handled by vector extensions to diffraction theory[37,38,39,40]. A calculation of the polarization point spread matrix and optical transfer matrix can be seen in Section 4 of Ref. 42.

- **Polarization aberration theory (PolAbT)**

Polarization aberration theory (PolAbT) describes the polarization effects of diattenuation, retardance, and apodization in a series expansion, where a cascade of terms separate mathematically the largest effects, from smaller effects and associate these polarization related image defects with constructional parameters and coating performance metrics.[41,42] For example one term, retardance tilt, is strongly associated with fold mirrors and causes the XX and YY image components to shift with respect to each other, making the PSF slightly elliptical. Another term retardance-defocus causes astigmatism from primary and secondary mirrors, which is polarization dependent; the orientation of the retardance rotates with the orientation of an incident linear polarization.[43]

PRT generates very large files of numbers, at least eight times more than a conventional ray trace, leaving the designer and management a substantial data interpretation task of the aberrations represented in a higher dimensional polarization space. PolAbT is more difficult analytically than PRT, but it simplifies the ray tracing results into a small number of "terms" which are understood and addressed in an uncoupled manner. This enables us to manage polarization aberrations in more complicated systems, such as WFIRST-CGI.

A distinction between the two is seen in the comparison between classical geometric aberration ray trace (analogue to PRT) and the structural aberration coefficients[44] (analogue to PolAbT) used by advanced designers to arrive quickly at near-optimized designs. Thus, using PolAbT together with PRT is far more powerful than either method alone. PolAbT will be used here to validate our results obtained with PRT.

- **Polarization ray-trace process**

The output of a CAD ray-trace computer program, e.g. CODE V or Zemax is combined with Fourier optics to calculate point spread functions. Figure 10 shows a side view of a typical optical system with a fan of rays originating from a point on the object and passing through an optical system with k surfaces to the system exit pupil. Each ray strikes a real physical surface at a known angle of incidence (no paraxial approximation).

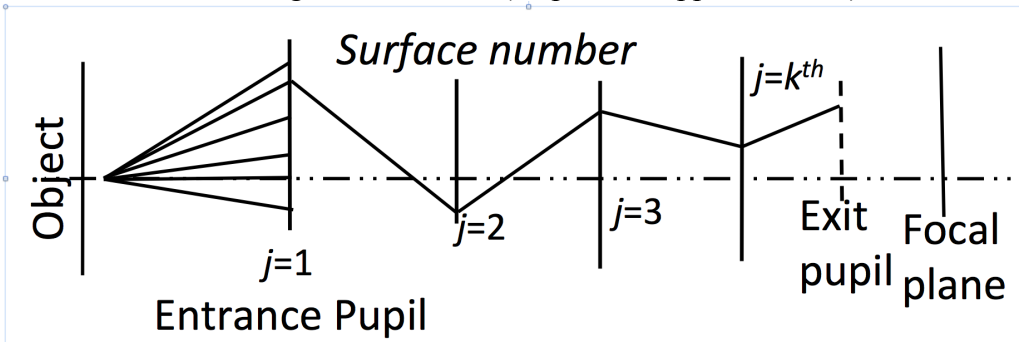

Figure 10 A fan of rays is shown passing from the object plane through an optical system with k surfaces before the exit pupil. For descriptive purposes a fan of rays is shown traced to surface j=1 and then a general single ray continues on to the optical system exit pupil at surface j=k+1.

We have estimates of the physical properties, which are values for $n(\lambda;\xi,\eta)+ik(\lambda;\xi,\eta)$ across each surface. Note that here we show the real and imaginary parts of the index of refraction as a function of wavelength and how they can change across each surface. Each surface in an optical system is either a reflecting metal or a dielectric.

Looking from the focal plane to the left in Fig 10, back through the optical system to object space we see the exit pupil face-on as shown in Figure 11, below.

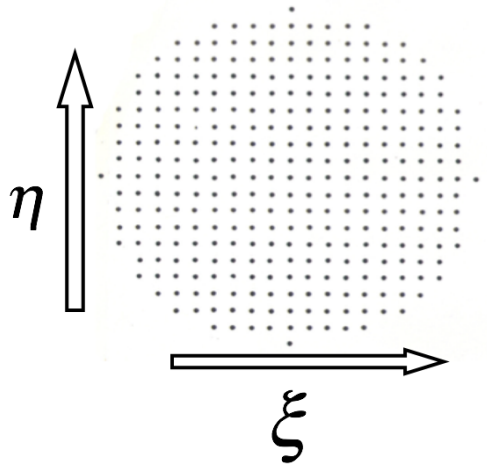

Figure 11 The exit pupil plane for the system in Fig 9 is shown looking from the focal plane at the right side of the figure 9, looking back to the left, through the optical system to object space where we see the exit pupil face-on. The electric field at each point is the incoherent sum of the four complex fields shown on the LHS of Equation 10.

Using the Fresnel equations, discussed earlier we calculate values for each of the four complex entries in Eq. 12, for each ray intercept through the system. We compute the multiplicative amplitude and cumulative phases for both perpendicular and parallel light and map these into four arrays of complex numbers across the exit pupil. We then take a digital FFT independently of each set of these 4 arrays of complex-field points to calculate the four complex PSF's, shown in Eq. 12.

5.2.9 Quantitative analysis of a three-mirror bent Cassegrain: An Example

- **The three-mirror Cassegrain specification**

To explain the effects of polarization aberration on the PSF and explore the implications for astronomical imaging, a generic telescope consisting of a primary, secondary, and fold mirror is analyzed. It is difficult to select a single fully representative astronomical high-resolution optical system as a polarization aberration example. Further, if an example system with many elements is chosen, it is more difficult to relate the individual surfaces to the features in the polarization aberration and polarized PSF, so a relatively simple system is analyzed. Quantitative values are calculated for this telescope's polarization. What is of particular interest is not these specific values but the functional form of the image defects and their order of magnitude. This should help the reader to assess whether these defects are of concern for various applications.

The example Cassegrain telescope and fold mirror is shown in figure 12. This system is far simpler and has far fewer optical surfaces than WFIRST-CGI, or LUVOIR or HabEx will have. It is illuminated on-axis. This curvature on the primary and secondary mirrors are optimized to minimize the geometric (trigonometry) ray aberrations. That is all of the rays that expand from a point source at infinity on axis in object space pass through a single point on axis at the image plane. There are no on-axis geometric wavefront aberrations; the OPL is equal for all on-axis rays. Thus, the on-axis image calculated by conventional ray tracing is ideal, so any deviations from ideal imaging are due to the polarization of the mirrors and are not mixed with the effects of geometric wavefront aberration. The mirrors are coated with bare aluminum and analyzed at 800 nm with a complex refractive index $N = 2.80 + 8.45i$.

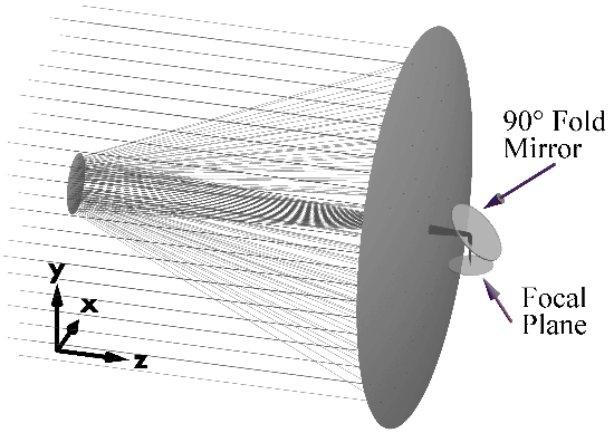

Figure 12. An example Cassegrain telescope system with a primary mirror at F/1.2, a Cassegrain focus of F/8, and a 90°-fold mirror in the F/8 converging beam. The 90°-fold mirror is folded about the *x*-axis. The primary mirror has a clear aperture of 2.4 meters. The operating wavelength is 800 nm. All three mirrors are coated with aluminum. The coordinates shown in the figure: *x* and *y* define the incident polarization states. The detector is placed at the bent Cassegrain image plane. The additional optics that form the coronagraph system, relay the complex wavefront past the occulting mask and the Lyot stop, onto the detector plane are not shown.

- **Diattenuation maps**

The polarization aberration of the example telescope of figure 12 will first be examined from maps of diattenuation and retardance and then as a Jones matrix representation at the exit pupil. The diattenuation contributions from the three mirror elements are shown in the first three panels of figure 13. The forth panel in figure 13 shows the cumulative diattenuation for the entire telescope as viewed looking into the exit pupil from the image plane. Each line inside the circle shows the diattenuation magnitude and the orientation of the maximum transmission axis at a point in the pupil. The primary and secondary mirrors (the first two panels in figure 13) produce rotationally symmetric, tangentially oriented diattenuation with a magnitude that increases quadratically[§] from the center of the pupil. The fold mirror introduces a horizontally oriented diattenuation with a linear and cubic variation along the vertical axis. The cumulative diattenuation map shown on the right is predominantly linear from top to bottom. Polarization

[§] When *linear* and *quadratic,* etc. are used throughout this document, *approximately linear* and *approximately quadratic* is implied as is standard in aberration theory.

aberration functions, which closely fit these diattenuation-maps are discussed in the appendix of another paper[8].

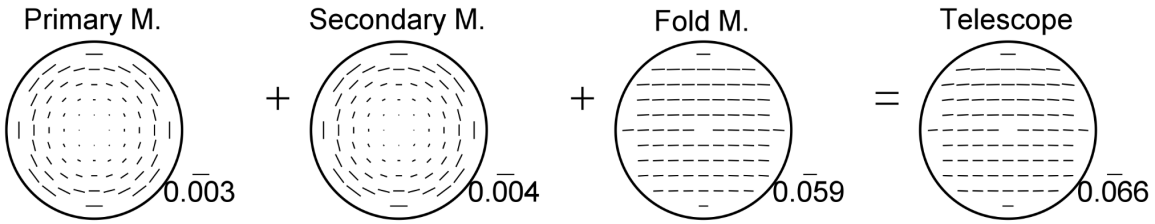

Figure 13. Diattenuation maps for each mirror element (the first three panels) and the cumulative diattenuation for the entire telescope (the last panel). The length of each line is proportional to the value of the diattenuation and the orientation of the line shows the axis of maximum transmission for a point in the pupil. The key in the lower right corner of each panel shows the scale of the largest diattenuation. For this example, telescope, the dominant source of diattenuation is the 90°-fold mirror.

- **Retardance maps**

The aluminum's retardance introduces a polarization dependent phase contribution to the OPL differently for the *s* and *p*-components of the light. Retardance aberration thus represents a difference in the metal coating's wavefront aberration contribution as experienced by orthogonal polarization states. Figure 14 shows the individual surface contributions to the retardance aberration in the first three panels and the cumulative retardance aberration through the system in the last panel. Each line shows the retardance magnitude and fast axis orientation at a grid of locations in the beam. The primary and secondary mirrors produce a rotationally symmetric tangentially oriented fast axis, which increases quadratically from the center, while the fold mirror introduces retardance with a vertically oriented fast axis. The fold mirror has a linearly varying retardance increasing from the bottom to the top of the pupil. Since the fold mirror has the largest retardance, the resultant retardance for the entire telescope shown on the right is similar to the fold mirror retardance with contributions from the primary and secondary mirrors. The cumulative linear retardance map (the fourth panel of figure 14) is primarily a constant retardance, with a linear variation from bottom to top, and a variation of retardance orientation from left to right. The cumulative retardances are shown as linear retardances (lines) but because the three-individual weak retardances in the first three panels are not strictly parallel or perpendicular, the fast and slow axes of the retardances in the last panel are slightly elliptical; however, the ellipticity, which has a maximum value of 0.0047, is much smaller than would be visible at this scale. Similarly, the diattenuation becomes slightly elliptical when the axes are not aligned, and in the map of figure 12 has a maximum ellipticity of 0.011.

Polarization aberration functions, which approximate these retardance maps, are discussed in the appendix of another paper[8]. Constant retardance is a constant difference in the wavefront aberration, a "piston" between polarization states; it changes polarization states but piston uniform across the wavefront is correctable by a simple translation (refocus). It is a first-order aberration that does not degrade image quality. The linear variation of retardance indicates a difference in the wavefront aberration tilt, *X* and *Y*-polarizations get different linear phases, and so their images are shifted from the nominal image location by different amounts.

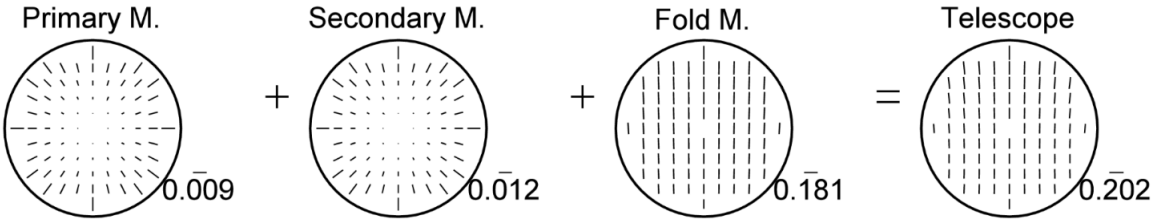

Figure 14. Retardance maps for each mirror element (the first three panels) and the cumulative retardance for the entire telescope (the last panel). The length of each line is proportional to the value of the retardance and the orientation of the line shows the fast axis. The key in the lower right corner of each of the four panels shows the scale of the largest retardance in radians. This figure shows that the dominant source of retardance at the exit pupil for the telescope of figure 12 is the 90°-fold mirror (third panel).

The spatial variation of the telescope's diattenuation (fourth panel of figure 13) and retardance (fourth panel of figure 14) is a low order variation, which can be characterized by simple polynomials[8]. The retardance from the primary and secondary mirrors has a quadratic phase variation; this pattern has been named "retardance defocus" by Chipman [45]. For *X*-polarized light, the relative phase is advanced quadratically moving along the *x*-axis from the center to the edge of the field, and is retarded quadratically moving to the edge of the field along the *y*-axis. This causes astigmatism arising from the different quadratic variations of ϕ_{rs} and ϕ_{rp} about the origin in figure 13. So, the *X*-polarized image, being astigmatic by 0.022 radians (0.012+0.010 or 3.4 milliwaves). Please see the scale of the primary mirror and secondary mirror retardances at the edge of the pupil in figure 14. This becomes slightly elongated in opposite directions on either side of the best focus. Similarly, for *Y*-polarized light, the relative phase is advanced moving along the *y*-axis from the center to the edge of the field, and is retarded moving to the edge of the field along the *x*-axis. So, the *Y*-polarized image is astigmatic with the opposite sign. This concave mirror-induced astigmatism is real and has been observed with interferometers.

Unlike conventional astigmatism, which on-axis would likely be caused by a cylindrical deformation in a mirror, this coating-induced astigmatism arises from the primary and secondary mirror's retardance defocus and is tied to the polarization state of the light. Coating-induced astigmatism rotates with the polarization state, whereas for a cylindrical deformation, the astigmatism would rotate with the mirror and not with the polarization state. For unpolarized light, the coating-induced astigmatic image is the average over the PSF of all polarization components, which is also the sum of the PSF for any two orthogonal components. So, the astigmatism which is seen in a single incident polarization state, such as *X*-polarized, when added to the astigmatism for *Y*-polarized light, where the astigmatism is rotated by 90° forms a radially symmetric PSF, which is slightly larger than the un-aberrated image. Inserting a polarizer will reveal the astigmatism in any particular polarization component.

Recall that the maps given in Fig's 13 and 14 are made assuming the reflecting surfaces are perfectly isotropic. That is the complex index of refraction is constant across each reflecting surface.

- **Amplitude and phase exit pupil maps.**

Within Eq 10, we define the amplitude response matrix (ARM) to be given by:

$$ARM = \begin{bmatrix} A_{XX}(\xi,\eta)e^{i\phi(\xi,\eta)_{XX}} & A_{XY}(\xi,\eta)e^{i\phi(\xi,\eta)_{XY}} \\ A_{YX}(\xi,\eta)e^{i\phi(\xi,\eta)_{YX}} & A_{YY}(\xi,\eta)e^{i\phi(\xi,\eta)_{YY}} \end{bmatrix} \quad \text{Eq. 17}$$

Equation 17 shows the amplitude response matrix (ARM) for the vector-wave ray trace of an imaging system. To provide an intuitive understanding, the amplitude response matrix for the 3-mirror bent Cassegrain, images of amplitude and phase across the exit pupil were created. Note that these were created assuming that the complex index of refraction does not change across the surface of the mirrors as it propagates through the system to the image plane. In the calculations for Figure 15 the index of refraction was assumed to be uniform across all the mirror surfaces.

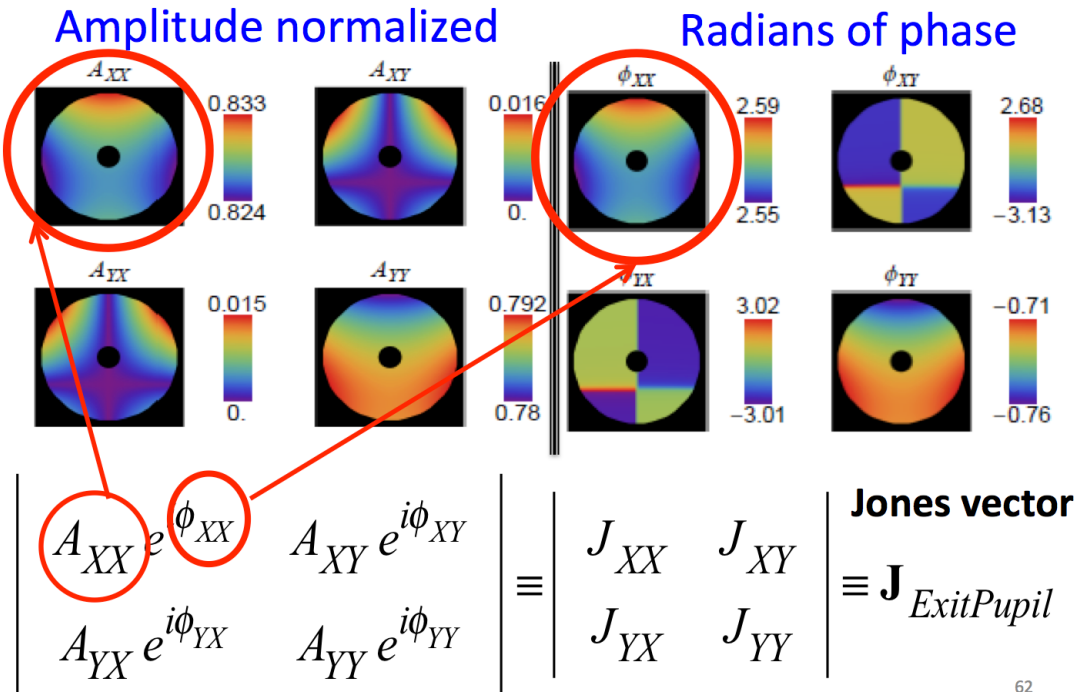

Figure 15. Amplitude and phase are shown plotted across the exit pupil of the three-mirror bent Cassegrain telescope system shown in figure 12. These 8 panels show the Jones vector amplitude (real) and phase (imaginary) terms across the exit pupil. The calculations were made assuming that the complex index of refraction was uniform across the surface of each mirror.

- **Shape of the four point spread functions**

A thermal white-light star at infinity on-axis illuminates this Cassegrain telescope, shown in Fig 12. The image plane irradiance is found using Equation 16 and is the linear superposition of the four amplitude PSF's[46] shown in Fig 16. Not visible at this scale is the fact that the centroid of each of the four PSF's are shifted slightly, one with respect to the other, to destroy rotational symmetry about the axis. If we examine the color coded wavefront maps in Fig 15

carefully, we see that the wavefront ϕ_{XX} is tilted relative to ϕ_{YY} which causes a slight translation at the image plane between the two PSF's: one for J_{XX} and one for J_{YY}. Also, the detailed shape of the on diagonal PSF's is not given by the classical Airy diffraction pattern derived from scalar theory, but rather they exhibit a core more broad in extent than is characteristic of the Airy pattern.

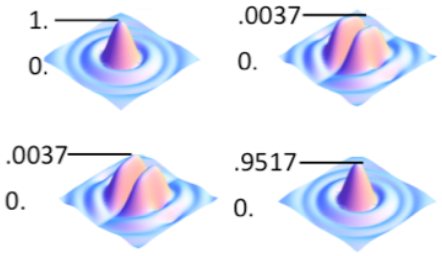

Figure 16, a single star on axis in object space produces the four-part amplitude response matrix (ARM), which, in turn gives the four PSF's given in Eq 17. Here we plot the amplitude (A) on the vertical axis for these complex elements, as they appear nearly super-posed at the focal plane of the Cassegrain telescope. The scale or size of each of these ARM elements is wavelength dependent. We refer the two-off diagonal highly structured PSF's as ghost PSF's.

The amplitudes presented in Fig 16 are given in Eq. 17 and show the terms within the amplitude response matrix (ARM). The functions shown in Fig. 16 are calculated by taking the modulus squared of these terms. The shapes of the off-diagonal ghost PSFs, I_{XY} and I_{YX} are highly irregular and show a "lumpy" structure that might be confused with an exoplanet. The spatial extent of each of these off-diagonal ghost PSFs, I_{XY} and I_{YX}, are twice as large as the spatial extent of the on-diagonal images.

In Fig 16, the two principal PSF images I_{XX} and I_{YY} (see Eq. 17) are shifted by 0.625 mas with respect to each other due to a linear variation of retardance at the mirror. With additional mirrors (like we have in the WFIRST-CGI) in the path will increase this separation. Each of the principal images, I_{XX} and I_{YY}, is slightly astigmatic, but with opposite astigmatism sign (rotated 90°). The PolAb analysis shows that the polarization crosstalk between X and Y polarized light, that is, the off-diagonal elements (I_{XY} and I_{YX}), which although weak, 0.0037 in amplitude, 10^{-5} in flux, has a much larger extent than the Airy disks of the principal components - additional mirrors (like we have in WFIRST-CGI) will increase the flux in the "ghost PSF's" calculated from the off-diagonal elements shown in Fig. 16. The intensities of these off diagonal profiles shown in Figure 16 above increases as the **square** of the number of mirrors and are dependent on ray path incidence angle, as well as the value of the metal thin film form birefringence.

Primary and secondary mirror coatings introduce astigmatism on-axis[47] which couples light into the orthogonal polarization state in Maltese cross type patterns, yielding the ghost PSFs. Focusing through fold mirrors introduces a linear variation of retardance, putting a different linear phase shift on the two principal components, shifting them in opposite directions! We derived eighteen scaling relations or design rules for these system parameters using PolAb theory within our published paper[10].

Note that our analysis so far is for perfectly isotropic thin films with uniform real and imaginary parts of the index of refraction. In section 2.9 we discuss the more realistic situation where thin films are anisotropic, because of form birefringence and the complex index changes with position across the mirror, or,

$$N(\lambda) = f(\lambda;\xi,\eta) \qquad \text{Eq. 18}$$

- **Location of the PSF images**

In the previous section, we showed that the image plane irradiance is the sum of four point-spread functions. In this section, we note that these PSF's are not perfectly super-posed upon each other at the image plane, but rather they are displaced slightly one from the other. This effect has implications for two applications: coronagraphy and astrometry.

Coronagraphy

The performance of the coronagraph depends on how perfectly the occulting mask matches the point spread function. But we have seen that the occulting mask image plane irradiance distribution is, in reality the incoherent sum of four independent PSF's, two highly distorted and the shape of the other two is not that of the typical Airy diffraction pattern.

Consider a Stokes imaging polarimeter located before the telescope of figure 2's focal plane measuring the PSF of an unpolarized star as a Stokes image. The PSFs for the *X*-polarized, $I_X = I_{XX}+I_{YX}$, and *Y*-polarized light, $I_Y = I_{XY}+I_{YY}$, at the focal plane are very close in form to the classical Airy diffraction pattern because the polarization-induced wavefront aberration, ϕ_{XX} and ϕ_{YY} in figure 15, is less than 8 milli-waves, and the amplitude apodization is less than 0.015. But these two PSF images are not exactly superposed; the peaks of I_X and I_Y are displaced from each other by 0.625 masec. The PSF cross-section through the maxima of I_X, I_Y, and $I_X - I_Y$ (the star's Stokes *Q* image), are shown in figure 17. The shift between the I_X and I_Y PSFs arises from the difference in slopes of the *s* and *p*-phases in the Fresnel coefficients, (red and blue tangent lines in figure 3(b)) which is the cause of the overall linear variations in ϕ_{XX} and ϕ_{YY}. Their difference $Q = I_X - I_Y$ is sheared from I_X and I_Y by 5.8 masec, as shown in figure 17, and is due to the shift between I_X and I_Y. These PSF's shifts and PSF's ellipticities are listed in table 1 for the bent Cassegrain telescope shown in Fig 12 which has a single 45°-fold mirror before the focal plane. The ellipticity of the PSF image was calculated by fitting an ellipse to the PSF at the half power points. Polarization aberrations cause the star images to be elliptical.

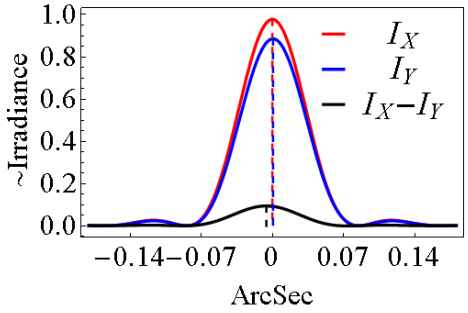

Figure 17. The cross-section profiles of the I_X and I_Y PSF images, one for each polarization and the profile of their difference are shown in red and blue in arc seconds from the center of the PSF. The black line shows Stokes Q image, the difference between the two PSFs.

Table 1 provides 1. quantitative assessment of the shape of the PSF, 2. the shear between the PSF in two orthogonal linear polarizations, 3. the flux in the off-diagonal elements in the ARM, 4 the radius of the encircled energy for the two on-diagonal PSF's and 5. the two off-diagonal PSF's. Note that the radius of encircled energy at 90% for the off-diagonal elements of the ARM are twice that for those on-diagonal elements. The ellipticity of the PSF is 7.5 x10^{-6}.

Table 1. The shape of the PSF is described by the following parameters: the PSF's flux, the radius of encircled energy, the PSF shears and the PSF ellipticity for *X* and *Y*-polarized incident light.

Characterize the shape of PSF	
PSF shear in object space:	
Between I_X and I_Y	0.625 masec
Between I_X and (Q=I_X-I_Y)	5.820 masec
Flux in PSF:	
$\frac{\text{flux of } I_{YX}}{\text{flux of } I_{XX}}$	0.0048%
$\frac{\text{flux of } I_{YY}}{\text{flux of } I_{XX}}$	90.6%
$\frac{\text{flux of } I_{YX}}{\text{flux of } I_{XX}}$	0.0046%
$\frac{\text{Peak of } I_Y}{\text{Peak of } I_X}$	90.6%
$\frac{\text{Peak of } (I_X - I_Y)}{\text{Peak of } I_X}$	$\frac{\text{Peak of } Q}{\text{Peak of } I_X} = 9.6\%$
Radius of 90% encircled energy in object space:	
$r_{XX} = r_{YY}$	0.15 arc sec
$r_{YX} = r_{XY}$	0.36 arc sec
Ellipticity of PSF:	
Unpolarized incident light	7.502 ×10^{-6}
X-polarized incident light	0.00199
Y-polarized incident light	0.00208

Astrometry

In astronomical applications involving the precise measurement of the location of the centroid of the PSF, distortions of the shape of the PSF are important. Most systems incorporate multiple folds[48,49]. These relay optics with multiple folds may increase the shear between PSF's polarization components. The variation of linear phase across the pupil is approximately linear, thus the shear between polarization components is linear in the F/#. As Clark & Breckinridge[71] showed, across the FOV, variations of PSF ellipticity and orientation are expected from polarization aberration.

The Fresnel polarization aberrations, unless corrected, may affect our ability to characterize exoplanets using space telescopes. At least two mitigation approaches have been suggested. These are discussed in a later section.

- **Detailed structure of the point spread function (PSF)**

Fig 18 (left) below shows a plot of the $\log_{10}$ of the irradiance in the meridional plane at the image for I_{XX} (the solid line) and I_{YX} (the dotted line) while Fig 18 (right) is a "face-on" map of I_{YX} with the classic Airy diffraction ring zeros superposed.

Note that the positions of the zeros in the PSF associated with I_{XX} are not superposed on those associated with I_{YX}. Therefore, ghost images could be misinterpreted as a "false alarm" candidate exoplanet.

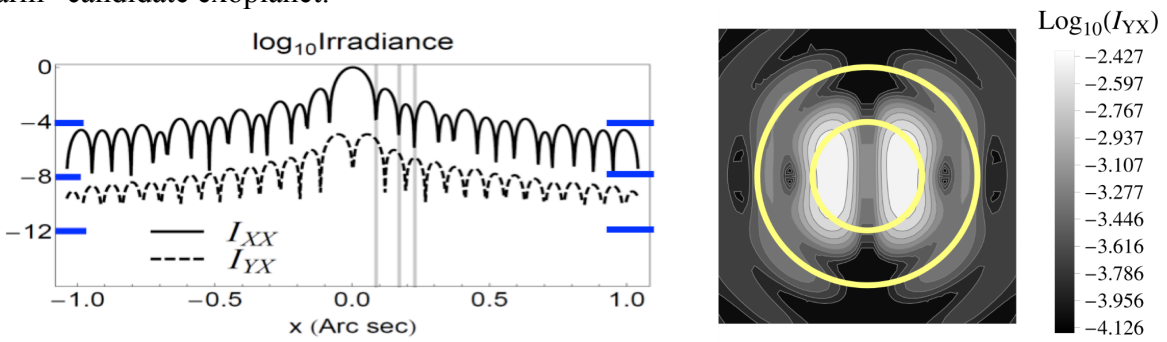

Figure 18 (upper) plots (solid line) of the $\log_{10}$ of the irradiance in the meridional plane at the image for the irradiance distribution. In the upper part of the figure, the lower dotted line shows the $\log_{10}$ irradiance for the irradiance distribution. The lower image in this figure is the "face-on" appearance of I_{YX} or the PSF Image of the off diagonal terms shown in Fig 16 and from Eq. 10. $\bar{\lambda} = 800$ nm D=2.4 m.

- **Polarization changes across the PSF**

To first order, the optical system of a telescope/coronagraph system is isoplanatic over the few arc second FOV, and the ~~fore-optics~~ PSF for the star is the same as that for the planet. We assume that the image plane central occulting mask suppresses the field from the star out to a distance of $\sim 3\lambda / D$. In the case of the 2.4 m Cassegrain system at λ=800-nm where $3\lambda / D \approx 0.2$ asec we find that the radius r of the 90% encircled energy is $r_{XX} = r_{YY} = 0.15$ asec and $r_{XY} = r_{YX} = 0.36$ asec. Radiation from the cross-product terms extends into a 0.2-asec coronagraph dark hole to create an irregular background pattern that will confuse exoplanet measurements and radiation will leak around the occulting mask that is designed using scalar theory. This will result in a system decrease in contrast between 10 and 10^{+3} to cause a space coronagraph to be no better than a ground-based coronagraph[46].

We define, by analogy to Eq. 8, the degree of polarization (DoP) at the image plane, x,y to be given by

$$D(x,y) = DoP = \frac{\left|E_{\perp}(x,y)\right|^2 - \left|E_{\parallel}(x,y)\right|^2}{\left|E_{\perp}(x,y)\right|^2 + \left|E_{\parallel}(x,y)\right|^2} \qquad \text{Eq. 19}$$

Figure 19, below, shows that the degree of polarization changes by almost a factor of 3 across the PSF at the detector plane of the 3-mirror bent Cassegrain shown in Fig. 11. In order to build an optimum Lyot coronagraph for this telescope requires that the complex occulting mask match the spatial distribution shown below. Scalar wave theory predicts no change in the DoP across the PSF. This figure clearly shows that the current scalar wave theory fails.

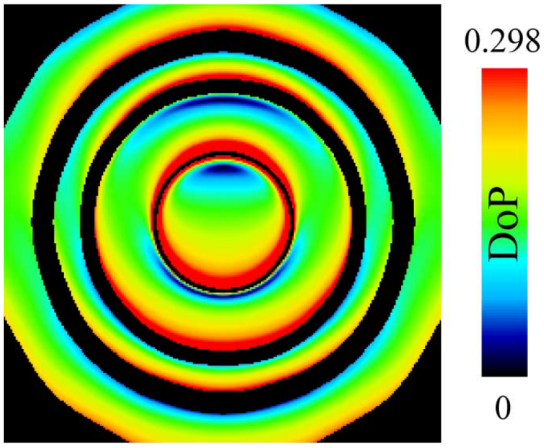

Figure 19 shows how the degree of polarization changes across the PSF of the 3-mirror Cassegrain telescope shown in Fig. 6. This was calculated using the POLARIS-M polarization ray-trace software. Scalar wave theory predicts no change. Therefore, a polarization (vector E&M) analysis is required to correctly model the end-to-end performance of space telescope/coronagraph systems.

The three-dimensional profile of the complex (amplitude and phase) occulting mask must match the electric field shown in Fig. 19 to maximize contrast. This topic is discussed further in section 2.10, below.

If the three-mirror bent Cassegrain telescope were to be used to feed a coronagraph, the coronagraph mask would need to match the amplitude and phase electric field pattern represented in Fig. 19, in order for the coronagraph optical system to have optimum performance. Calculations of the change of the degree of polarization across the PSF are important to the design, fabrication, test, alignment and understanding of occulting masks for HabEx and LUVOIR.

The three-mirror bent Cassegrain telescope shown in Fig 12 is not compatible with high contrast coronagraphy unless compensated with a complex mask whose complex transmissivity depends on the as-fabricated optical coatings.

- **Conclusions from the analysis of the 3-mirror bent Cassegrain**

Breckinridge, Lam and Chipman[46] used the POLARIS-M software to provide a detailed complex vector polarization analysis of a typical astronomical bent Cassegrain telescope comprised of an F/# 1.2 primary and a secondary mirror whose optical power is sufficient to give an F/#8 beam converging past a 45-degree flat mirror to a focal plane. The curvatures on the primary and secondary were designed to give zero geometric aberrations on axis. Coatings were assumed to be bare Al and wavelength 800nm. Several important facts about image

quality in astronomical telescopes were found[9,10] that affect high-contrast exoplanet coronagraphy and astrometry. Let $\gamma =$ the ratio of the peak of on-diagonal PSF's shown in Fig 16 to the off-diagonal PSF's shown in the same figure. That is, γ is the ratio of the terms in the amplitude response matrix: J_{XY} or J_{YX} to the peak of J_{XX} or J_{YY} respectively. We use the astronomers' convention that the higher the contrast, the worse the system is for planet characterization. The lowest contrast possible is the most desirable.

1. The image plane PSF is the incoherent sum of 4 point nearly super-posed spread functions: two normalized near 1, but distorted PSF's and two highly distorted "Ghost PSF's", with long "tails", but a factor, γ fainter at the peak by approximately $4x10^{-3}$ in amplitude as shown in Fig 16 above.
2. The magnitude of this factor γ depends on the wavelength and angles of incidence and the sign of the rays on each mirror in the path as well as the physical properties, of the highly reflective coatings on the mirrors. Increasing γ results in reduced contrast.
3. The number of fold mirrors in the optical system determines the factor γ which increases as the square of the number of "aligned" fold mirrors. Crossed fold mirrors (s-p at first becomes p-s at the next) at the same angle of incidence can compensate polarization. "Aligned" here means the number of mirrors which share their s-p orientation minus the number with the opposite p-s orientation. This is a possible method for reducing the magnitude of the cross-product terms in the ARM and desensitizing the system to the retardance polarization aberration.
4. The radius of the spatial extent of the 90% encircled energy of these two ghost PSF images is approximately twice as large as the mean radius of the two primary patterns: J_{XX} and J_{YY}.
5. The PSF images for two orthogonal linearly polarization components of the ARM (J_{XX} and J_{YY}) are shifted with respect to each other, causing the PSF image for un-polarized point sources to become slightly elongated (elliptical) with a centroid separation on the order of 0.6 mas. The result is that the inner working angle does not have rotational symmetry; it is position angle dependent on the sky, which degrades the angular resolution of the system.
6. The full-width half-maximum of the J_{XX} and J_{YY} is larger than that for the classic Airy pattern calculated using scalar wave theory. This fact increases the inner working angle to degrade the angular resolution of the system and reduce exoplanet science yield.

- **Summary**

The diattenuation maps and the retardance maps are for the 3-mirror bent Cassegrain telescope and do not include the coronagraph optics. The coronagraph optics accept the complex vector wavefront from the telescope at an image plane, where the occultation mask is located and optically processes the radiation to obtain the high contrast levels needed to characterize terrestrial exoplanet for LUVOIR and HabEx. In our work planned here, we will ray-trace a fore-optic system more realistic that the simple 3-mirror bent Cassegrain and add coronagraph optics for our analysis.

5.2.10 Polarization reflectivity isotropy (Form birefringence)

- **Introduction**

The reflectivity at a point on a metal mirror depends on its electrical conductivity at 10^{15} Hz. But the electronic properties of highly reflecting metal thin films are not completely isotropic, as we assumed above. The more isotropic we require the film to be the more difficult it is to fabricate and thus more expensive. The question is how anisotropic can the

thin films be on each of the reflecting elements in a telescope/coronagraph system and yet maintain the required 10^{-10} to 10^{-11} contrast requirement at the detector plane. This information is needed to specify thin film mirror coatings for HabEx and LUVOIR. A mirror substrate surface might be figured to wavefront error $\lambda/100$ but after coating, the wavefront error for the now highly reflecting mirror might jump to an unacceptable $\lambda/20$ [51]! Typical aluminum mirror coatings vary from 50 to 250 nm thickness. For large mirrors the evaporation sources are often placed close to the mirror, so that the distances on the mirror to the closest source is variable, thus leading to some nonuniformities of deposition thickness. Here we are raising the possibility of the issue of thickness variations on which we are not at present expert, but plan to become better informed during this research through interactions with those who have coated astronomical mirrors. The expected scale length is the distance between deposition sources, which would typically be about ¼ to 1/10 of the mirror diameter of a large mirror.

Equation 11 defines the vector transmittance, or in the case of a mirror reflectivity, $\vec{\tau}_2(\xi_2,\eta_2)$. We show here that it varies across the exit pupil. The physical phenomenon that produces this effect is called form birefringence. The birefringence properties of metal thin films used by astronomers to coat telescope mirrors may be explained in terms of the anisotropic electrical properties of the molecules of which the crystals are composed. Birefringence is the optical property of a material having a refractive index that depends on the polarization and propagation direction of light. These optically anisotropic materials are said to be birefringent (or birefractive). The birefringence is often quantified as the maximum difference between refractive indices exhibited by the material. Crystals with non-cubic crystal structures are often birefringent, as are plastics under mechanical stress (stress birefringence).

- **Electronic properties of metals and mirror reflection**

Low (1 to 20 cycles) spatial frequency changes in amplitude and phase reflectivity and transmission across any optical element in the optical system will have a profound change on the shape of the PSF for exoplanet coronagraphy. The electronic properties of the highly reflecting mirror are strongly dependent on the microcrystalline structure of the volume of matter a few microns below the surface of the mirror.

An optical ray incident on the metal surface penetrates into that surface[50] and the reflection occurs within the first few microns of the metal. The metal absorbs radiation, contributing to the phase changes in the reflected beam, which, in turn creates "noise" or aberrations in the image to reduce exoplanet coronagraph contrast. Classic E&M theory shows that the reflectivity of the mirror depends on the conductivity of a virtual charge within the metal.

Our analysis in section 2.2 through 2.8 above we assumed that polarization present across the complex wavefront is introduced only by changing ray angles across an isotropic metal reflecting surfaces. The electronic properties of metal mirror itself are assumed isotropic, that is they are independent of position across the surface of all optical elements in the system and appear uniform across the exit pupil. But this is not true for the scattered light levels required for terrestrial exoplanet coronagraphy.

The vector complex reflectivity of changes across the mirror caused by inhomogeneities introduced by the physical deposition process and its geometry are discussed in the literature[51],[52],[53],[54]. These changes have been well understood within the microcircuit industry which relies on stable UV single-frequency lasers to expose specially prepared photoresist in micro-lithography processes to create computer chips with very high quality and uniformity at 10 cm^2 scale sizes on very flat surfaces in a laboratory production environment.

Astronomical applications, however require deposition on steeply doubly-curved (1< F/# <2) and large area (10^5 cm^2) surfaces to be used in space. To achieve the high reflectivity

necessary for astronomical telescopes, the crystalline structure of highly reflecting Ag or Al metal thin films needs to be very uniform. The work proposed here, in section 6, will for the first time enable a quantitative assessment of the uniformity of as deposited highly reflecting thin films and determine the effects of anisotropy on exoplanet coronagraph contrast.

Horwitz[51] built upon the work of Smith and Purcell[55] to show experimentally that 1. Mirror coatings in general are not perfectly isotropic and 2. That unpolarized light becomes partially polarized upon reflection from an anisotropic mirror surface.

In section 2.4 we used $N = n + ik$ in the Fresnel equations and in the ensuing sections 2.5 through 2.8 showed the need for vector E&M and that the shape of the detector plane PSF, which determines contrast, is distorted. In reality telescope mirrors, because of their size and necessarily large coated surface are anisotropic. It is essential that we answer: what is the role of this anisotropy in system contrast and how much anisotropy can the primary mirrors of HabEx and LUVOIR have and still produce useful results.

To account for this anisotropy, we write the complex index of refraction at the jth surface within the telescope/coronagraph system as

$$N_j(\xi,\eta) = n_j(\xi,\eta) + ik_j(\xi,\eta) \qquad \text{Eq. 20.}$$

Where $n_j(\xi,\eta)$ is the spatial distribution of the real part of the index of refraction across the jth surface and $k_j(\xi,\eta)$ is the spatial distribution of the imaginary part of the index of refraction across the jth surface in the optical path of the telescope/coronagraph system. These are for the highly reflecting metal (for example Al or Ag) on the mirror surface. Fig. 20 shows a mirror with spatially varying *N*.

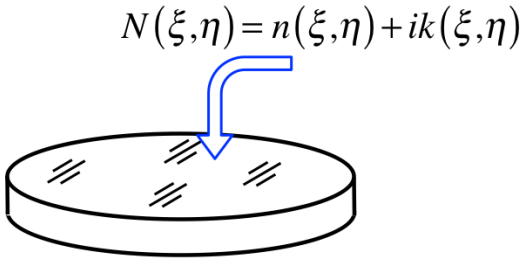

Figure 20. The real and imaginary parts of the index of refraction vary across the surface of a mirror. The amount of change depends on the process used to deposit the highly reflecting metal mirror. Without great care the complex reflectivity across the mirror will be position dependent and thus encode unwanted very small, but possibly significant wavefront errors into the system.

Polaris-M, the polarization ray-trace CAD program used in our studies, has the capability to insert fabrication anisotropies for each of the j=1 to j=k surfaces (see Fig 10) in any optical system, including coronagraph occulting masks, Lyot stops and special pupil apodizing functions as well as the primary, secondary, A/O mirrors and small fold mirrors.

- **Form birefringence - requirement**

Birefringence is the change of polarization state of light when it interacts with matter. Form birefringence creates unwanted polarization aberrations to introduce unwanted narrow-angle forward scattered light in coronagraphs. Form birefringence[56] is the birefringence

attributed to the structure of the matter that light interacts with in order to be reflected, as for example, by highly reflecting metal thin films.

Studies of the role of form birefringence in image quality for high contrast (10^{11}) coronagraphs is important to investigate in order to develop requirements for the allowable internal polarization as a function of retrievable contrast.

Horowitz[58] investigated one source of form birefringence in high reflectivity mirrors. He observed that by depositing Al onto a substrate at non-normal incidence resulted in the formation of an asymmetric crystalline microstructure within the metal. He measured the polarization reflectivity at normal incidence and observed a strong correlation between the angle of deposition and the degree of polarization of reflected light.

A second source of form birefringence is caused by the way the metal film is annealed as the atoms of the vapor strike the cold substrate. Fig 21 shows a sketch of the cross-section of a mirror substrate with a metal film deposition and an extended wavefront at normal incidence from above. The left-hand portion of the film has deposited itself as an amorphous film, whereas the right hand has crystallized into a periodic array of crystals. The electronic resistance at light frequency of ~10^{15}Hz is different in the amorphous part of the structure than it is in the columnar crystalline structure to cause changes in the polarization content across the wavefront of the reflected light.

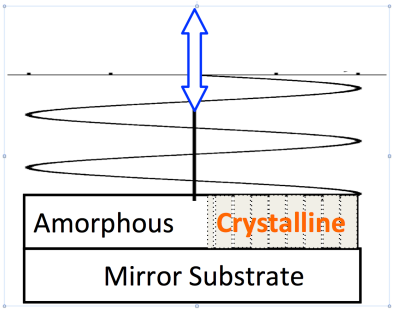

Figure 21 shows a drawing of the crossection of a metal mirror surface. An electromagnetic wave is incident from above onto the highly reflecting metal coating.

Figure 22 below shows a micro-fracto-graph of the fractured edge on an Aluminum film copied from Dirks & Leamy, This Solid Films, Vol. 47, 219-233, 1977. This figure shows the columnar structure of a thin metal film on a substrate.

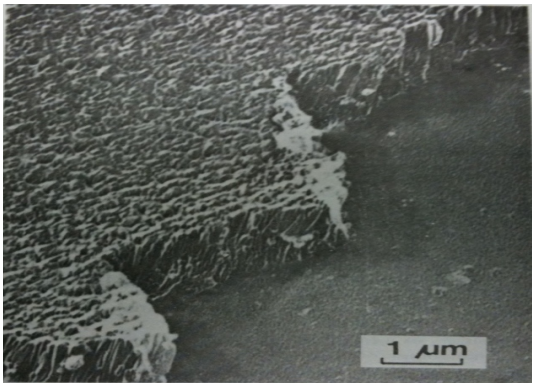

Figure 22 Microfractograph of the fractured edge on an aluminum film copied from Dirks & Leamy Thin Solid Films Vol. 47, 219-233 (1977)

- **Process methods used for telescope mirrors**

Large aperture telescope mirrors should exhibit noticeable form birefringence because of the way they are manufactured. Both ground and space mirrors such as the 4-meter at KPNO and the 8-meter Gemini are manufactured by depositing a thin metal film onto a substrate (typically glass) in a "clam-shell" vacuum chamber.

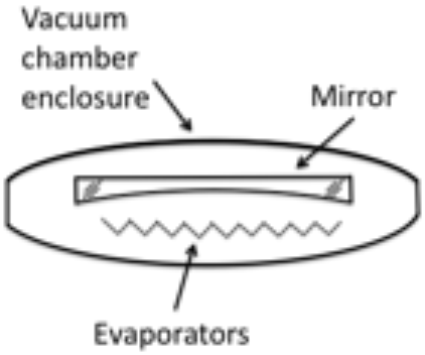

Figure 23 Typical clamshell evaporating chamber geometry used for large aperture telescope primary mirrors.

The deposition process is expected to introduce anisotropic defects due to columnar microstructure in the thin film coatings. Figure 22 shows the typical microstructure of an Al film[57]. Because of their size, large astronomical mirrors are coated in vacuum using clamshell evaporators similar to that shown in figure 23 with simple thermal sources such as hot filaments. However more sophisticated coating chambers, have been developed more recently[58.] Coating non-uniformity and polarization introduced by coating microstructure[59,60] are known to be typical of mirrors produced by thermal evaporation processes.

Anisotropic defects due to columnar microstructure are expected for several reasons. First the mirror is curved such that the incidence angles of deposited metal will have an overall variation across the aperture. Second, to minimize the size of the vacuum chamber enclosure, the evaporators are located close to the metal surface causing larger and more localized variations of incident angle. But detailed experimental investigations of astronomical mirrors, although proposed[61] have not been done to show the extent of polarization from large mirrors produced with new sophisticated and challenging deposition techniques.

For mirrors with thermally evaporated coatings or coatings "painted" on using ion-assisted deposition techniques we expect the spatial scale of the form birefringence structure imbedded into the metal reflecting surface to be centimeters on a meter-class optic. Adaptive optics can remove a portion of this, depending on the number of actuators and the amplitude of the phase excursions. For example, cm spatial structures require more than 100x100 actuators to control meter class optics. Clearly, a portion of the birefringence error can be compensated, but what remains unknown is the amplitude of the phase excursions and their spatial frequencies. Once we know these effects we can tolerance and specify them and recommend mitigation approaches.

- **Complex index is process dependent**

Dielectric materials like glasses, which are commonly used in lenses, prisms & windows are well mixed and homogeneous with a very uniform index of refraction for glasses in the optical regions of the spectrum. Dielectric materials have the imaginary part of the index of refraction equal to zero, that is *k* in the equation: $N = n + ik$ is zero. For example, the index of refraction, *n*, of Schott BK7 is uniform and stable to $1{:}10^{+6}$ in refractive index. The complex index of refraction for metal mirrors is not as reproducible and uniform as that for glass. It varies across the surface as well as from deposition to deposition. The fabrication processes for metal films is not as well controlled as that for dielectrics. This is particularly noticeable for large aperture optics.

Table 1, below shows how the real and imaginary parts of the index of refraction for Al vary from process to process. Column 1 gives the reference to the measurements, column 2 gives the published measurement of the real part of the index of refraction, n, and column 3 shows the published measurement of the imaginary part of the index of refraction, k.

Reference	n	k
Rakic[62]	0.99864	6.5823
Hageman & Gudat [63]	0.98192	6.4646
Rakic & Djunsic & Majewski [64]	0.95154	6.3586

Table 2 real and imaginary parts of the index of refraction, N, for Al at 546 nm wavelength as measured for different substrates by different observers.

Reference	n	k
Rakic[64] & Djunsic & Majewski	0.14462	3.1602
McPeak, Jayanti, Kress, Meyer, Iotti & Rossinelli[65]	.043656	3.5758
Babar & Weaver[66]	.051226	3.5433
Johnston & Christy[67]	.059097	3.5624

Table 3 real and imaginary parts of the index of refraction, N, for Ag at 546 nm wavelength as measured for different substrates by different scientific groups.

- **Mathematical background**

The optical properties of *birefringent materials* depend on the direction of the light's polarization, as compared to isotropic materials, which have identical properties in all directions. Isotropic and anisotropic materials are characterized by 3×3 *dielectric tensors* and 3×3 *gyrotropic tensors*. Ray tracing through birefringent materials is different from ray tracing isotropic materials. Rays refracting into anisotropic media are decomposed into two rays with different propagation directions and orthogonal polarizations. These two rays are *Eigenmodes* and propagate without change of polarization state.

Isotropic reflecting materials such as silver, gold, aluminum, and typical over coating materials with form birefringence behaves as spatially varying weakly uniaxial or biaxial

materials. The ray-tracing algorithm for ray intercepts on birefringent materials tracks the light field, amplitude and direction change through birefringent interfaces using the polarization ray-tracing matrix.

A *biaxial material* has three distinct principal indices, and there are four directions, plus and minus along two lines within the material having degenerate Eigenpolarizations. Unlike uniaxial material, biaxial material has two optic axes; thus, the label biaxial.

The *dielectric tensor* $\boldsymbol{\varepsilon}$ relates the variation of refractive index with the light's polarization state by relating **E** to **D** as given in Eq 21, below

$$\mathbf{D} = \varepsilon\mathbf{E} = \begin{pmatrix} D_x \\ D_y \\ D_z \end{pmatrix} = \begin{pmatrix} \varepsilon_{XX} & \varepsilon_{XY} & \varepsilon_{XZ} \\ \varepsilon_{YX} & \varepsilon_{YY} & \varepsilon_{YZ} \\ \varepsilon_{ZX} & \varepsilon_{ZY} & \varepsilon_{ZZ} \end{pmatrix} \begin{pmatrix} E_x \\ E_y \\ E_z \end{pmatrix} \qquad \text{Eq. 21}$$

Figure 24 below shows an electromagnetic wave propagating in a isotropic medium, of index *n*, (the vacuum of space, for example) striking a boundary with a birefringent material of index: n_F, n_M, n_s such as an inhomogeneous Al or Ag coating on a highly reflecting mirror.

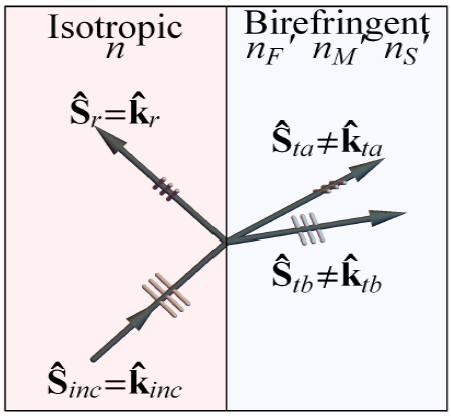

Figure 24. Notation for the theoretical development of the relationship of the dielectric tensor to mirror reflectivity.

The corresponding Fresnel amplitude transmission and reflection coefficients are more complex for birefringent intercept, since the refractive index varies with **E**. The necessary set of parameters for ray tracing comprises six 3×1 vectors: (**k**, **S**, **E**, **D**, **B**, **H**) and the associated refractive index of the ray. These are calculated by solving Maxwell's equations with appropriate boundary values. Let $\hat{\mathrm{k}}$ be the normalized propagation vector for a light ray and S be the Poynting vector. This Poynting vector is the same as $\hat{\mathrm{k}}$ in an isotropic medium, but differs in an anisotropic medium. "Eta-carrot" is the normal to a surface at a ray intercept, then the normalized refracted or reflected vector **k** at a birefringent material is given in Eq. 22:

$$\hat{\mathbf{k}} = \frac{n\ \hat{\mathbf{k}}_{inc} + \left(-n\ \hat{\mathbf{k}}_{inc} \cdot \hat{\boldsymbol{\eta}} \pm \sqrt{n^2 \left(\hat{\mathbf{k}}_{inc} \cdot \hat{\boldsymbol{\eta}} \right)^2 + \left(n'^2 - n^2 \right)} \right) \hat{\boldsymbol{\eta}}}{\left\| n\ \hat{\mathbf{k}}_{inc} + \left(-n\ \hat{\mathbf{k}}_{inc} \cdot \hat{\boldsymbol{\eta}} \pm \sqrt{n^2 \left(\hat{\mathbf{k}}_{inc} \cdot \hat{\boldsymbol{\eta}} \right)^2 + \left(n'^2 - n^2 \right)} \right) \hat{\boldsymbol{\eta}} \right\|} \qquad \text{Eq. 22}$$

Where n is the refractive index for the incident ray, n' is the refractive index of the exiting ray, the sign of the square root is + for refraction and – for reflection. This equation is the general form of the standard refraction and reflection equations generalized for anisotropy. The solution is complicated by the fact that $\hat{\mathbf{k}}$ is a function of n' which is not specified at the beginning of the calculation. So, the reflection and refraction algorithm must simultaneously solve for $\hat{\mathbf{k}}$ and n'.

A birefringence subroutine will be integrated into the Polaris-M polarization ray tracing code. This code uses a special 3x3 formalism called polarization ray tracing matrices, **P,** to generalize Jones matrices for polarization ray tracing. The **P** matrix keeps track of the resultant electric field direction, amplitude coefficients, and the mode direction in the global coordinates, which are preferred for polarization ray tracing. The resultant spatial distribution of **P** matrices is used to characterize the polarization aberrations of birefringent elements and of optical systems, and here would be applied to spatially varying form birefringence of telescope mirrors.

Interface	Reflected $(m, n)\rightarrow v=rc$ & $(m, n)\rightarrow w=rd$		Refracted $(m, n)\rightarrow v=ta$ & $(m, n)\rightarrow w=tb$	
Isotropic/Isotropic	$(s, p)\rightarrow s'$ $(s, p)\rightarrow p'$	$\Rightarrow (s, p)\rightarrow(s', p')$	$(s, p)\rightarrow s'$ $(s, p)\rightarrow p'$	$\Rightarrow (s, p)\rightarrow(s', p')$
Isotropic/Birefringent	$(s, p)\rightarrow s'$ $(s, p)\rightarrow p'$	$\Rightarrow (s, p)\rightarrow(s', p')$	$(s, p)\rightarrow v$ $(s, p)\rightarrow w$	

The isotropic-to-birefringent interface case uses the same s and p-incident basis as in the isotropic interface case. As shown the four exiting modes are rs, rp, ta, and tb; the two reflected modes reflect back to the incident isotropic medium and two refracted modes refract into the birefringent medium. The two-reflected s and p-modes share the same $\hat{\mathbf{S}}'$, while the two refracted birefringent modes, labeled with subscripts v and w in equation, split into two directions. So, $(m, n, v, w) = (s, p, s', p')$ in reflection, and (s, p, v, w) for refraction. If the refracting medium is biaxial, the two refracted modes are *fast*- and *slow*-modes; $(m, n, v, w) = (s, p, fast, slow)$. The definition of the coordinate system is shown in Fig 25 for refraction.

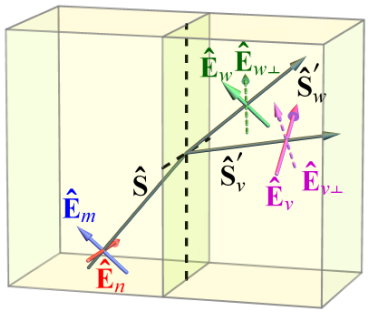

Figure 25 notation used in the theoretical development of the relationship between stress and the polarization state of broadband reflected white-light.

- **Mode coupling in refraction though an isotropic-to-birefringent interface:**

In Figure 25, we see that the incident ray with orthogonal modes, labeled as n (red) and m (blue), splits into two exiting modes as $v=ta$ (pink) and $w=tb$ (green) in two directions. In biaxial and uniaxial materials, $\mathbf{E}_v$ and $\mathbf{E}_w$ are linearly polarized.

The two refracted modes propagate in two different directions with $\hat{\mathbf{k}}_{ta} \neq \hat{\mathbf{k}}_{tb} \neq \hat{\mathbf{S}}_{ta} \neq \hat{\mathbf{S}}_{tb}$. The amplitude coefficients of the exiting modes from each incident mode are

$$\begin{pmatrix} a_{inc,s\to ta} \\ a_{inc,s\to tb} \\ a_{inc,s\to rs} \\ a_{inc,s\to rp} \end{pmatrix} = \mathbf{F}^{-1} \cdot \begin{pmatrix} \vec{\mathbf{s}}_1 \cdot \hat{\mathbf{E}}_{inc,s} \\ \vec{\mathbf{s}}_2 \cdot \hat{\mathbf{E}}_{inc,s} \\ \vec{\mathbf{s}}_1 \cdot \vec{\mathbf{H}}_{inc,s} \\ \vec{\mathbf{s}}_2 \cdot \vec{\mathbf{H}}_{inc,s} \end{pmatrix} \quad \& \quad \begin{pmatrix} a_{inc,p\to ta} \\ a_{inc,p\to tb} \\ a_{inc,p\to rs} \\ a_{inc,p\to rp} \end{pmatrix} = \mathbf{F}^{-1} \cdot \begin{pmatrix} \vec{\mathbf{s}}_1 \cdot \hat{\mathbf{E}}_{inc,p} \\ \vec{\mathbf{s}}_2 \cdot \hat{\mathbf{E}}_{inc,p} \\ \vec{\mathbf{s}}_1 \cdot \vec{\mathbf{H}}_{inc,p} \\ \vec{\mathbf{s}}_2 \cdot \vec{\mathbf{H}}_{inc,p} \end{pmatrix} \qquad \text{Eq. 23}$$

$\hat{\mathbf{E}}_{ta}$, $\hat{\mathbf{E}}_{tb}$, $\hat{\mathbf{E}}_{rs}$, and $\hat{\mathbf{E}}_{rp}$ can be calculated. The two **P** matrices for refraction are:

$$\left.\begin{aligned} \mathbf{P}_{ta} &= \begin{pmatrix} a_{inc,s\to ta}\hat{\mathbf{E}}_{ta} & a_{inc,p\to ta}\hat{\mathbf{E}}_{ta} & \hat{\mathbf{S}}_{ta} \end{pmatrix} \cdot \begin{pmatrix} \hat{\mathbf{E}}_{inc,s} & \hat{\mathbf{E}}_{inc,p} & \hat{\mathbf{S}}_{inc} \end{pmatrix}^T \\ &\text{and} \\ \mathbf{P}_{tb} &= \begin{pmatrix} a_{inc,s\to tb}\hat{\mathbf{E}}_{tb} & a_{inc,p\to tb}\hat{\mathbf{E}}_{tb} & \hat{\mathbf{S}}_{tb} \end{pmatrix} \cdot \begin{pmatrix} \hat{\mathbf{E}}_{inc,s} & \hat{\mathbf{E}}_{inc,p} & \hat{\mathbf{S}}_{inc} \end{pmatrix}^T, \end{aligned}\right\} \qquad \text{Eq. 24}$$

and the two **P** matrices for reflection are:

$$\begin{aligned} \mathbf{P}_{rs} &= \begin{pmatrix} a_{inc,s\to rs}\hat{\mathbf{E}}_{rs} & a_{inc,p\to rs}\hat{\mathbf{E}}_{rs} & \hat{\mathbf{S}}_{rs} \end{pmatrix} \begin{pmatrix} \hat{\mathbf{E}}_{inc,s} & \hat{\mathbf{E}}_{inc,p} & \hat{\mathbf{S}}_{inc} \end{pmatrix}^T \text{ and} \\ \mathbf{P}_{rp} &= \begin{pmatrix} a_{inc,s\to rp}\hat{\mathbf{E}}_{rp} & a_{inc,p\to rp}\hat{\mathbf{E}}_{rp} & \hat{\mathbf{S}}_{rp} \end{pmatrix} \begin{pmatrix} \hat{\mathbf{E}}_{inc,s} & \hat{\mathbf{E}}_{inc,p} & \hat{\mathbf{S}}_{inc} \end{pmatrix}^T. \end{aligned} \qquad \text{Eq. 25}$$

Since the two reflected modes share the same pair of $\hat{\mathbf{S}}_{rs} = \hat{\mathbf{S}}_{rp}$, and the couplings between *s* and *p*-states are zero for an uncoated surface ($a_{inc,s\to rp}$=$a_{inc,p\to rs}$=0). Therefore, $\mathbf{P}_{rs}$ and $\mathbf{P}_{rp}$ are combined to

$$\mathbf{P}_r = \begin{pmatrix} a_{inc,s\to rs}\hat{\mathbf{E}}_{rs} & a_{inc,p\to rp}\hat{\mathbf{E}}_{rp} & \hat{\mathbf{S}}_r \end{pmatrix} \cdot \begin{pmatrix} \hat{\mathbf{E}}_{inc,s} & \hat{\mathbf{E}}_{inc,p} & \hat{\mathbf{S}}_{inc} \end{pmatrix}^T, \qquad \text{Eq. 26}$$

When light refracts or reflects into an isotropic medium, the two modes combine to one **P** matrix because they have the same **S** direction. However, when light propagates into a birefringent medium, the incident ray splits into two directions and the exiting modes have two different **S**. In this case, two **P** matrices are needed to describe the two modes, which cannot be combined.

We can make analogy to stress birefringence. Optical materials undergo structural change at the molecular level due to various environmental conditions, such as temperature change or external stress. The microscopic structural change often induces optical birefringence, and as a result stress in optical elements affects the wavefront and point spread function. The associated stress induced retardance is generally undesirable, changing the wavefront aberration and polarization aberration in complex patterns. Thus, it is very useful to ray trace elements with stress birefringence to access the impact and calculate tolerances. Stress can easily become frozen into the material, particularly when one surface, such as the inner surface solidifies before the outer material, or vice versa.

In large telescope optics with form birefringence, the birefringence is expected to vary in a complex way depending on the location of the evaporative sources, the planetary motions used

during deposition, the shape of the mirror, and the temperature and contamination variations within the chamber.

- **Form birefringence State of the Art**

The polarization state of the complex wavefront reflected from a metal mirror depends not only on the angle of incidence and reflection (given by the Fresnel equations) but also on the physical properties of the deposition process, which are often characterized by the deposition angle, surface cleanliness, quality of the vacuum, geometry, and process methods such as ion assisted deposition. The polarization reflectivity properties of these anisotropic dielectrics and metal coatings were studied by Hodgkinson and his colleagues and the results published in a series of papers [57,68].

A module within Polaris-M will be written to calculate how the birefringence varies across the surface of an aluminized mirror.

5.2.11 Optical processing to maximize star extinction & minimize exoplanet absorption by the instrument

To minimize scattered light, the complex vector field at the image plane where the occulting mask is located must match the complex vector operator characteristic of the occulting mask. We use the formalism developed for optical processing of images[69]. From Eq. 17 we write the expression for the incoherent superposition of the four complex scalar fields representing each of the 4 incoherent elements of the ARM as:

$$\vec{u}^{-}(x_3,y_3) = \mathcal{F}\{J_{XX}\} + \mathcal{F}\{J_{XY}\} + \mathcal{F}\{J_{YY}\} + \mathcal{F}\{J_{YX}\}, \qquad \text{Eq. 27}$$

Where $\mathcal{F}$ is the Fourier transform operator, each of the four terms is complex and the superscript – sign on $\vec{u}$ refers to the complex electric field infinitesimally (ε) to the left (-) or in front of the of the image plane. Note that it has been shown[10] mathematically, confirmed observationally[70] and relationships verified[71] that the centroids of the four terms in Eq. 27 are displaced slightly one from the other.

Let the transmittance of the image-plane occulting-mask be represented by the complex transmittance, $\vec{\tau}(x_3,y_3)$, then the electric field infinitesimally (ε) to the right (+) of the complex occulting mask at the image plane is given by

$$u^{+}(x_3,y_3) = u^{-}(x_3,y_3)\cdot\vec{\tau}(x_3,y_3) \qquad \text{Eq. 28}$$

To achieve the contrast levels needed for terrestrial exoplanet spectrometry we need to minimize $u^{+}(x_3,y_3)$, over the wavelength bands of interest while maximizing the transmittance between the inner and outer working angle.

To further control the unwanted radiation, this process needs to be repeated at the exit pupil to create the optimum complex EM Lyot stop.

This is a form of EM field impedance matching both at the image-plane occulting-mask and at the exit pupil Lyot stop under the conditions to maximize the electric field of the exoplanet at the entrance aperture to the spectrometer and to minimize the electric field from the star.

5.2.12 Polarization aberration mitigation

Polarization aberration mitigation is particularly challenging for high performance exoplanet coronagraphs designed and built to characterize terrestrial exoplanets. Polarization aberrations, like geometric aberrations cannot be completely eliminated. Each optical surface, device and mask within an optical system contributes to polarization aberrations and we seek to minimize

the total effect of these aberrations as they appear at the detector plane by balancing the polarization contribution from each device, mask and optical surface. The challenges can be explained referring to Fig 22, which is Fig 1 repeated here for convenience.

Figure 26 below shows a schematic of the optical path or "circuit" for a typical Lyot coronagraph. Incoherent white-light from the primary star and its exoplanets, enters the optical system from the left and passes through the Fore-optics of the system which contain the primary and secondary mirrors, the A/O mirrors necessary to form the "dark-hole" at the detector plane and the fold mirrors needed to package the instrument into a volume to fit into a spacecraft. The region the fore-optics occupies is identified by the symbol **A**. This fore-optic system relays the white-light incoherent object space irradiance distribution, typically a star on axis onto a complex occulting mask located at a system image plane and positioned to mask or occult the bright parent star of the system understudy. The off-axis exoplanet light passes around the mask to continue through the system. The occulting mask has a complex transmittance indicated by **B**. Light from the star is attenuated by the complex transmittance of this occulting mask. Light passes through that section of the post-optics, labeled **C** in Fig 26 before the Lyot stop at **D**. The Lyot stop is a complex apodizer located at an image of the primary and is used to control the phase and amplitude of the complex EM field that is diffracted around the sharp edge of the primary mirror, secondary support shadows and the segment lines. After the Lyot stop the radiation reflects from the several mirrors needed for packaging into the spacecraft as it passes through region **E** of the post optics to strike the detector.

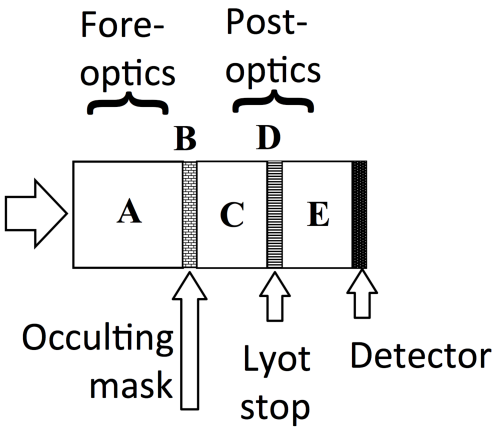

Figure 26. Optical schematic or circuit for a typical Lyot coronagraph. The source is to the left and light passes through regions A, B, C, D, E before it is absorbed by the detector, where the modulus squared of the resulting field is recorded.

The baseline solution, now used by the WFIRST-CGI team is to place a linear polarizer-filter over the focal plane in front of the detector to admit either perpendicular or parallel-polarized light. This will **not filter out or isolate one aberration** from the other because the light incident on the detector has already been corrupted by optics in regions A, C, and E as shown in Fig 1. The off-diagonal elements of the Jones Matrix shown in Eq. 10, that is J_{XY} and J_{YX} are created and modified in regions A, B, C, and E, and by the time the wavefronts get to the polarizing filter located just in front of the detector they are already corrupted. Wavefront errors cannot be isolated using filters. High levels of correction require phase and amplitude masks similar to those proposed by Clark and Breckinridge[72]

Optical designers have a variety of methods to change the polarization aberrations of any particular optical system, see Maymon & Chipman[73]. It is beyond the scope of this document to elaborate on these methods in detail. Fresnel and coating-induced polarization aberrations tend to

be of small magnitude with low order functional variation (constant, linear, quadratic, etc.) as reported in Chipman 1989a & 1989b. The following text summarizes several mitigation approaches:

(A) Reducing angles of incidence: Since the diattenuation and retardance are quadratic in the angle of incidence for modest angles, reducing the largest angles of incidence can significantly reduce polarization aberration. For example, fold mirror angles, can be reduced or the F/# of mirrors and lenses reduced.

(B) Reducing coating polarization: The optical coating prescriptions for antireflection coatings of lenses and reflection-enhancing coatings of mirrors, provide design degrees of freedom (thicknesses and materials) to adjust the diattenuation and retardance. In our experience, these coating prescriptions can be adjusted to moderately reduce the polarization properties, but cannot zero out diattenuation or retardance for substantial angle and wavelength ranges. The surfaces of antireflection-coated lens typically have one third or less the diattenuation of uncoated lens surfaces, providing great benefit. The reflection enhancing coatings for mirror often increase the retardance and diattenuation of metal mirrors in some wavebands.

(C) Compensating polarization elements: Polarization aberrations can be introduced in several ways. Simply placing a (spatially uniform) weak polarizer (diattenuator) and a weak retarder in the system could zero out the polarization aberration at one point in the pupil, leaving overall polarization aberrations smaller. A spatially varying diattenuator and retarder with polarization magnitude approximately equal to the cumulative diattenuation and retardance of figure 13 and figure 14 but orthogonally oriented, would nearly eliminate the polarization aberration. Such a polarization plate could be considered as the matrix inverse of the Jones pupil in Eq. 10. Such correction plates might be fabricated from liquid crystals polymers with spatially varying magnitude and orientation of diattenuation or retardance, similar to the vortex retarders used in coronagraphy (Clark & Breckinridge 2011, McEldowney, Shemo & Chipman 2008, Mawet et al. 2009). Wedged, spherical, and aspheric crystalline elements or element assemblies can provide a wide variety of compensating polarization aberrations (Chowdhury et al. 2004). Since polarization aberrations of telescopes and fold mirrors tend to be small, spatially varying anisotropic thin films, which can only provide small retardances, could provide another path toward compensation (Hodgkinson 1998).

(D) Crossed fold mirrors: Fold mirrors tilted about opposite axes, such that the *p*-polarized light exiting one mirror is *s*-polarized on the second, have a compensating effect for both diattenuation and retardance (Maymon & Chipman 1992 and McClain et al. 1992). A linear variation of polarization about the zero will still remain across the pupil.

(E) Compensating optical elements: The diattenuation of lenses has the opposite sign (greater *p*-transmission) than the diattenuation of mirrors. Thus, including lenses would reduce the diattenuation from the primary and secondary mirrors in the example system. Similarly, sets of coatings might be selected to have opposite retardance contributions. Despite several concerted attempts, one of the authors (Chipman) has not been able to change the sign of the diattenuation or retardance of an antireflection or reflection enhancing coating over a useful spectral bandwidth. In practice, this approach has never been very successful.

Considering these mitigation approaches, when novelty, fabrication issues, scattering, tolerances, and risk are balanced against the small magnitude of the polarization aberration, these cures can easily become worse than the problem.

To design optical systems, typically a merit function is defined to characterize the wavefront and image quality, and an optimization program adjusts the system's constructional parameters to find acceptable configurations. (1) If polarization ray tracing parameters are included in the merit function, parameters such as diattenuation and retardance, the optimizer can balance the polarization aberrations against the wavefront aberrations and other constraints, pushing the solutions toward reduced polarization aberration. (2) Similarly, if the coating and

polarization element constructional parameters are included in the optimization, the optimizer can explore the coating design space and polarization element configuration to find compensation schemes. For example, overcoated layers on aluminum will modify the polarization shown in figure 16. These two steps are complicated, but advanced users can apply these methods, often through the use of the optical design program's macro languages, to evaluate polarization mitigation strategies listed above.

5.2.13 Comparison metrics for software codes

- **Metrics considered**

Two metrics were considered for the comparison of the polarization ray-trace output of Polaris M with that of Code-V. One of these we call the **polarization coupling coefficient**, the other one we call the **four-component intensity profile.** The four-component intensity profile metric was selected.

- **Polarization coupling coefficient**

Today the effects of polarization aberration on images are commonly calculated using three available analysis programs. These are: CODE V, Zemax and Polaris-M. CODE-V and Zemax perform both polarization analysis and optical design optimization. Polaris-M was designed specifically for polarization analysis, and its optimization performance is in development. Polaris-M can take as input an optical design already optimized for minimum geometric (trigonometry) path-length errors. Here it is of interest to compare polarization aberration analyses generated by one code with that of another. This section identifies appropriate metrics for the comparison of the polarization computation provided by Code V with that provided by Polaris-M.

Our analysis given in section 5.2.7 titled **image formation in polarized light** shows that a single unpolarized point source in object space maps into four images or four independent (uncorrelated) nearly superposed point spread functions (PSFs). We showed in Equation 16, that we have four point-spread functions, one each for the uncorrelated complex scalar fields J_{XX}, J_{YY}, J_{YX} and J_{XY} and the detector plane point spread function is the linear, incoherent superposition of four PSF's as shown in Eq. 16, above, which is repeated here as Equation 29 for convenience.

$$I_3(x_3,y_3) = \underline{I_3(x_3,y_3)}\Big|_{XX} + \underline{I_3(x_3,y_3)}\Big|_{YY} + \underline{I_3(x_3,y_3)}\Big|_{YX} + \underline{I_3(x_3,y_3)}\Big|_{XY} \qquad \text{Eq. 29}$$

The subscript XX means X light entering the system polarized in the X direction mapped into the X direction or X<=X, and similarly for light in the Y direction. The subscript XY refers to light entering the system polarized in the Y direction that exits the system in the X direction, or Y<=X. Note that at the focal plane the terms $\underline{I_3(x_3,y_3)}\Big|_{XX}$ and $\underline{I_3(x_3,y_3)}\Big|_{XY}$ are intensities polarized in the X direction and that the terms $\underline{I_3(x_3,y_3)}\Big|_{YY}$ and $\underline{I_3(x_3,y_3)}\Big|_{YX}$ are intensities polarized in the Y direction. These intensities are integrated over the image plane (x_3,y_3) to give a value for how much the optical system polarizes the unpolarized radiation input light. The integrated intensities of each of the four PSF's is given by

$$\left.\begin{aligned} I_{XX} &= \int \underline{I_3(x_3,y_3)}\big|_{XX}\, dx_3\, dy_3 \\ I_{YY} &= \int \underline{I_3(x_3,y_3)}\big|_{YY}\, dx_3\, dy_3 \\ I_{XY} &= \int \underline{I_3(x_3,y_3)}\big|_{XY}\, dx_3\, dy_3 \\ I_{YX} &= \int \underline{I_3(x_3,y_3)}\big|_{YX}\, dx_3\, dy_3 \end{aligned}\right\} \qquad \text{Eq. 30}$$

The polarization analysis codes calculate a value for $I_{XX};\ I_{YY};\ I_{YX};\ I_{XY}$.

The intensity at the image plane as calculated by Code V is then

$$I_{cdV} = \begin{bmatrix} I_{XX}\big|_{cdV} & I_{XY}\big|_{cdV} \\ I_{YX}\big|_{cdV} & I_{YY}\big|_{cdV} \end{bmatrix} \qquad \text{Eq. 31}$$

And the intensity at the image plane as calculated by Polaris M is

$$I_{PM} = \begin{bmatrix} I_{XX}\big|_{PM} & I_{XY}\big|_{PM} \\ I_{YX}\big|_{PM} & I_{YY}\big|_{PM} \end{bmatrix} \qquad \text{Eq. 32}$$

We define a metric for the net polarization coupling caused by polarization aberrations to be C_P where:

$$C_P = \frac{I_{XY} + I_{YX}}{I_{XX} + I_{YY} + I_{XY} + I_{YX}} \ . \qquad \text{Eq. 33}$$

From Eq. 33 and Eq. 31 a coupling coefficient for the parameters calculated by Code V is found to be:

$$\left[C_P\right]_{CdV} = \frac{I_{XY}\big|_{cdV} + I_{YX}\big|_{cdV}}{I_{XX}\big|_{cdV} + I_{YY}\big|_{cdV} + I_{XY}\big|_{cdV} + I_{YX}\big|_{cdV}} \ . \qquad \text{Eq. 34}$$

From Eq. 33 and Eq. 32 a coupling coefficient for the parameters calculated by Code V is found to be:

$$.\left[C_P\right]_{PM} = \frac{I_{XY}\big|_{PM} + I_{YX}\big|_{PM}}{I_{XX}\big|_{PM} + I_{YY}\big|_{PM} + I_{XY}\big|_{PM} + I_{YX}\big|_{PM}} \ . \qquad \text{Eq. 35}$$

The numerator is the light exiting in the undesired cross polarization terms, while the denominator is the total quantity of light at the image. We define the difference between the

calculation of the two coupling coefficients. One from Code V and the other from Polaris M, to be $\left[C_P\right]_\delta$, where we take the modulus of the difference to give

$$\left[C_P\right]_\delta = \left|\left[C_P\right]_{CdV} - \left[C_P\right]_{PM}\right| \ . \qquad \text{Eq. 36}$$

This metric is not as precise a comparison as the one described under "Four-component intensity profile", which is used in the description of milestones.

- **Four-component intensity profile.**

Our team will use the optical prescription (surface figure, separations, and coatings) provided by the WFIRST-CGI to the ExoPlanet program office and apply Polaris-M to calculate the four-incoherent system PSF's described below.

We showed in Equation 16, that we have four point-spread functions, one each for the uncorrelated complex scalar fields J_{XX}, J_{YY}, J_{YX} and J_{XY} and the detector plane point spread function is the linear, incoherent superposition of four PSF's as shown in Eq. 16, above, which is repeated here as Equation 37 for convenience.

$$I_3(x_3,y_3) = \underline{I_3(x_3,y_3)}\Big|_{XX} + \underline{I_3(x_3,y_3)}\Big|_{YY} + \underline{I_3(x_3,y_3)}\Big|_{YX} + \underline{I_3(x_3,y_3)}\Big|_{XY} \qquad \text{Eq. 37}$$

To compare the polarization aberrations calculated by CODE-V with those calculated by Polaris-M we will compare the four profiles on the RHS of Eq. 37, as calculated by CODE-V with the same four profiles as calculated by Polaris-M.

The WFIRST-CGI project office will provide us with the Code-V calculated profiles for the four image intensities at the occulting-mask image plane. These are identified in the equation 38, below.

$$\left.\begin{aligned}\left\{I_3(x_3,y_3)\right\}_{Code-V} = &\left\{\underline{I_3(x_3,y_3)}\Big|_{XX}\right\}_{Code-V} + \left\{\underline{I_3(x_3,y_3)}\Big|_{YY}\right\}_{Code-V} + \\ &+\left\{\underline{I_3(x_3,y_3)}\Big|_{YX}\right\}_{Code-V} + \left\{\underline{I_3(x_3,y_3)}\Big|_{XY}\right\}_{Code-V}\end{aligned}\right\} \qquad \text{Eq. 38}$$

The University of Arizona College of Optical Sciences Polaris-M will be used to calculate the profiles for the four intensities at the occulting-mask image plane as shown in Eq 39.

$$\left.\begin{aligned}\left\{I_3(x_3,y_3)\right\}_{Polaris-M} = &\left\{\underline{I_3(x_3,y_3)}\Big|_{XX}\right\}_{Polaris-M} + \left\{\underline{I_3(x_3,y_3)}\Big|_{YY}\right\}_{Polaris-M} + \\ &+\left\{\underline{I_3(x_3,y_3)}\Big|_{YX}\right\}_{Polaris-M} + \left\{\underline{I_3(x_3,y_3)}\Big|_{XY}\right\}_{Polaris-M}\end{aligned}\right\} \qquad \text{Eq. 39}$$

Let $\delta(x,y)$ define the difference in the four component intensity profiles as follows:

$$\left.\begin{aligned}
\delta(x,y)_{XX} &= \left| \left\{ \underline{I_3(x_3,y_3)}\big|_{XX} \right\}_{Code-V} - \left\{ \underline{I_3(x_3,y_3)}\big|_{XX} \right\}_{Polaris-M} \right| \\
\delta(x,y)_{YY} &= \left| \left\{ \underline{I_3(x_3,y_3)}\big|_{YY} \right\}_{Code-V} - \left\{ \underline{I_3(x_3,y_3)}\big|_{YY} \right\}_{Polaris-M} \right| \\
\delta(x,y)_{YX} &= \left| \left\{ \underline{I_3(x_3,y_3)}\big|_{YX} \right\}_{Code-V} - \left\{ \underline{I_3(x_3,y_3)}\big|_{YX} \right\}_{Polaris-M} \right| \\
\delta(x,y)_{XY} &= \left| \left\{ \underline{I_3(x_3,y_3)}\big|_{XY} \right\}_{Code-V} - \left\{ \underline{I_3(x_3,y_3)}\big|_{XY} \right\}_{Polaris-M} \right|
\end{aligned}\right\} \quad \text{Eq. 40}$$

The four profiles of $\delta(x,y)$ given in Eq. 40 are the differences in the intensity profiles: Code-V minus Polaris-M and define a comparison metric to evaluate Code-V against Polaris-M. This metric will be used in Milestone # 1 to compare the polarization calculations of Polaris M with those of CODE-V.

5.3 CURRENT STATE OF THE ART

5.3.1 Introduction

The objectives of this TDEM are to provide the science community with

- An accurate vector E&M model and an assessment of the wavelength dependent contrast of the WFIRST-CGI coronagraph
- A quantitative understanding of the role of polarization in direct imaging exoplanet coronagraphs
- Requirements for the spatial distribution of the vector complex reflectivity and transmissivity of optical components.
- Polarization aberration mitigation methodologies and an assessment of contrast levels achievable with coronagraphs on LUVOIR and HabEx.

5.3.2 WFIRST-CGI polarization ray trace state of the art.

Tang[74] analyzed the WFIRST-CGI AFTA coronagraph fore-optic system and found a 37-nm P-V difference at 430-nm and a 9 nm P-V difference at 550-nm wavelength. This is for the wavefront directly in front of the star-image occulting mask after the 18-mirror reflections. He reports contrasts in the 10^{-8} regime, but does not specify the coatings. Other than this work there are no known open literature publications that quantify coronagraph performance as a function of instrument polarization. Our work will be the first.

There are no known quantitative digital model calculations of estimated contrast at the detector plane for any coronagraph type that take into account full polarization aberrations and the electronic structure of mirror reflecting surfaces. Our work will be the first.

We are told that Jim McGuire (JPL engineer) has made some calculations of polarization contrast at the detector plane using CODEV but no open literature or technical reports are available. As part of this polarization ray-trace activity we will compare our calculations with those of JPL. If disagreement exceeds three percent further investigation will be pursued.

Therefore, our work is the first-time NASA, and the science team community will have detailed quantitative insight into the role of polarization aberrations in image formation within space telescope exoplanet coronagraphs and how these aberrations may affect the quality of science data.

5.3.3 Polarization ray trace LUVOIR/HabEx state of the art

LUVOIR has a design for the primary and secondary. Their coronagraph design is under development and will be made available to us by October 2017. The LUVOIR telescope primary is segmented (gaps) and shadowed by a secondary support structure to complicate diffraction and possibly introduce unwanted polarization aberrations. There are no known publications on the subject of instrument polarization for LUVOIR architecture. There is some ongoing related work supported by S. Shaklan on the effects of secondary support shadows and segment gaps on exoplanet coronagraphy but there are no open-literature reports of that activity.

HabEx has a design, similar to that of Exo-C for the fore-optics and the design of the coronagraph is in development.

5.3.4 Characterize form birefringence to tolerance contrast

No research group has ever characterized form birefringence to tolerance exoplanet contrast, and thus discover the role of coating uniformity on exo-planet yield. This work will provide constraints on thin film uniformity based on required contrast. These requirements will lead to thin film fabrication specifications for large aperture primary mirrors. The state of the art for understanding how form-birefringence manifests itself in the anisotropy of the affects.

The polarization state of the complex wavefront reflected from a metal mirror depends not only on the angle of incidence and reflection (given by the Fresnel equations) but also on the physical properties of the deposition process that are often characterized by the deposition angle, surface cleanliness, quality of the vacuum, geometry, and process methods such as ion assisted deposition. The polarization reflectivity properties of these anisotropic dielectrics and metal coatings were studied by Hodgkinson and his colleagues in a series of papers[57].

A module within Polaris-M will be written to calculate how the birefringence varies across the surface of an aluminized mirror.

6.0 Milestone definitions

This section contains the milestone definitions

6.1 MILESTONE # 1

Conduct a polarization aberration analysis of the WFIRST-CGI optical system from object space to the occulting-mask image plane using Polaris-M software. Calculate the intensity profiles across the occulting-mask image plane for each of the four polarization terms: I_{XX}, I_{YY}, I_{XY} and I_{YX}. Calculate the difference between those profiles determined by JPL using Code-V and those profiles calculated by our group at OptSci using Polaris-M. We will analyze the WFIRST-CGI optical system from object space to the occulting-mask image plane system using PolAbTh. We expect any difference between Polaris-M, Code-V, and PolAbTh to be well within a 3% window.

If the difference exceeds +-3% our approach to understanding the difference is to compare the indices used for the metal and dielectric coatings & thickness and examine potential

coordinate system set up errors in Polaris –M. WFIRST-CGI has already been polarization ray-traced by using Code-V flight project engineers we are using this opportunity provided by the project to verify that the more computationally efficient and physically intuitive Polaris-M, and PolAbTh.

We think mutual agreement is likely between the two codes in point spread function calculations. We will be also applying Polaris-M to analyze the polarization aberrations in functional forms (see the PolAbTh appendix to ref 10) which Code V doesn't provide. This will enable a much deeper understanding of the polarization aberration buildup and structure of the polarized point spread function than could be provided by CodeV. We proposed to go beyond the Code V polarization ray trace results and thus provide the technology program with more value-added than simply using Code V.

We understand the algorithmic approach for the coating polarization ray trace in Code V. Prof. Chipman has used it since 1995 when it was introduced. Prof. Chipman has taught students the objective of the algorithm and has run and had students run simple examples, which produced qualitatively the correct results.

Algorithms may have branches, special cases, divide by zero handling, accuracy implementation issues, and other undocumented behaviors. Differences between the implementation of algorithms are expected at some level. We have had many discussions where many users have stated that they received or suspected that they received wrong answers from the Zemax coating and birefringent polarization ray trace. Similarly, we have had a few discussions where users have questioned Code V polarization results. Polaris-M may generate inaccurate results for this coronagraph analysis; we will have access to the source code, and powerful tools within Mathematica to analyze logical and accuracy issues which may arise. This contract provides an opportunity to make a careful comparison the polarization analysis in two codes, which has never been done before.

Deliverables from JPL to the TDEM15 team.

Baseline design input used by the University of Arizona team shall be compared to that used by JPL for polarization ray-tracing the WFIRST-CGI optics from the primary to the occulting mask and include:

1.1. Opto-mechanical prescription for the fore-optics in Code V "lens-deck".

1.2. Central wavelength and mirror coatings standard name or the real and imaginary parts of the index of refraction for isotropic coatings on the primary, secondary, A/O surfaces, fold and relay optics.

1.3. Filter wavelengths and filter bandwidths

1.4. Complex amplitude and phase transmittance of the pupil apodizing function.

1.5. Coordinate system and grid size of the Code V design.

1.6. Profiles for the four intensities at the image plane;

$$\left\{I_3(x_3,y_3)\right\}_{Code-V} = \left\{\underline{I_3(x_3,y_3)}\Big|_{XX}\right\}_{Code-V} + \left\{\underline{I_3(x_3,y_3)}\Big|_{YY}\right\}_{Code-V} + \left\{\underline{I_3(x_3,y_3)}\Big|_{YX}\right\}_{Code-V} + \left\{\underline{I_3(x_3,y_3)}\Big|_{XY}\right\}_{Code-V} \quad \text{Eq. 41}$$

2. Deliverables from the TDEM15 team to NASA/JPL in Excel, narrative, image or graphical format.

2.1. Verification that geometrical optical path lengths to match prior WFIRST ray tracing calculations to within 10 milliwaves to ensure same systems being analyzed.

2.2. Exit pupil amplitude and phase maps (image and data) as viewed from the occulting mask looking toward object space.
2.3. Complex point spread function (PSF) in front of the occulting mask at multiple wavelengths across the optical bandwidth. Verify amplitudes match prior calculations within 10% to verify that coating models and polarization algorithms are comparable.
2.4. Image of the polarization (complex amplitude and phase) changes across the PSF.
2.5. Diattenuation and retardance maps cumulative polarization aberration and individually for the primary, secondary, and other optical elements as graphics.
2.6. Evaluate second order polarization aberration contributions from surfaces and for cumulative wavefront and comment on the polarization aberration buildup or compensation.
2.7. Profiles for the four intensity profiles:

$$\left.\begin{aligned}\left\{I_3(x_3,y_3)\right\}_{Polaris-M} &= \left\{\underline{I_3(x_3,y_3)}\Big|_{XX}\right\}_{Polaris-M} + \left\{\underline{I_3(x_3,y_3)}\Big|_{YY}\right\}_{Polaris-M} + \\ &+\left\{\underline{I_3(x_3,y_3)}\Big|_{YX}\right\}_{Polaris-M} + \left\{\underline{I_3(x_3,y_3)}\Big|_{XY}\right\}_{Polaris-M}\end{aligned}\right\} \quad \text{Eq. 42}$$

2.8. A brief technical report discussing possible sources of differences between JPL and the U of A team results will be provided.

6.2 MILESTONE # 2

Collaborate as members of the LUVOIR and HabEx teams to conduct polarization aberration analyses of LUVOIR and HabEx optical systems from object space to the detector using Polaris-M software.

1. Deliverables from the LUVOIR and HabEx teams to the TDEM15 team at the College of Optical Sciences.
   1.1. Opto-mechanical prescription for the LUVOIR and HabEx telescope/coronagraph systems
   1.2. By consensus of the team: accept a baseline (Mark 1) opto-mechanical design for LUVOIR and accept a baseline (Mark 1) opto-mechanical design for HabEx telescope/coronagraph that has been geometric ray aberration optimized.
2. Deliverables from the TDEM15 team to NASA teams in Excel, narrative, image or graphical format.
   2.1. Verification that geometrical optical path lengths to match prior ray tracing calculations to within 10 milliwaves to ensure same systems being analyzed.
   2.2. Exit pupil amplitude and phase maps (image and data) as viewed from the coronagraph detector plane looking toward object space.
   2.3. Calculate the intensity profiles across the image plane for each of the four polarization terms: I_{XX}, I_{YY}, I_{XY} and I_{YX} for both LUVOIR and HabEx.
   2.4. Recommendations to maximize contrast and transmittance

6.3 MILESTONE # 3

Polarization reflectivity anisotropy. Use laboratory apparatus to measure the spatial distribution of the form birefringence from a large (3.8-m) mirror with a "typical" astronomical coating. Achieve a measurement sensitivity of 1-milli-fringe at 500nm.

Investigate the role of thin film fabrication errors, which are manifest in anisotropic complex reflectivity changes across mirror surfaces on three key performance parameters: polarization aberration, transmittance, and chromatic aberration within imaging telescope/coronagraph systems. The allowable tolerance to achieve the required image quality, transmittance and chromatic aberration performance of a space coronagraph will be investigated.

This measurement will give insight into the subject of coating anisotropy for typical large aperture astronomical mirrors. This anisotropy can be inserted into models of LUVOIR and HabEx to investigate the role of polarization anisotropy in limiting high contrast optical systems designed and built for characterization of exoplanets.

Approach:

- Form birefringence simulation
    - Adapt Polaris-M's anisotropic material ray tracing algorithm to analyze metal mirrors with form birefringence. The form birefringence is described by a spatially varying dielectric tensor, where a diagonal 3x3 tensor with equal complex elements indicates an isotropic metal film.
    - Use the form birefringence ray trace algorithm to calculate the perturbations to reflected phase and polarization as a function of the form birefringence magnitude.
    - Develop algorithms to relate the spatial frequency of form birefringence variations to the exoplanet contrast, and tolerance the form birefringence for low spatial frequencies.
    - Results of our numerical simulation will be compared to those theoretical calculations published by Hodgkinson[60] and McCall[75] to verify our approach.
- Spherical mirror form birefringence measurement
    - The physical deposition processes used to create every metal surface reflecting area results in subtle changes in the complex refractive index and its anisotropy causing small variations of phase and amplitude at different points across the surface of each mirror called "Form Birefringence". These tasks research potential impact on form birefringence and its possibility to cause changes in high contrast instruments.
    - Perform a quick and inexpensive polarization measurement to look for form birefringence the AL coating on an available 3.8 m spherical mirror at U Arizona's mirror laboratory. This will provide the first look, to our knowledge, at form birefringence in a large "astronomical-like" mirror. With this measurement, we are seeking to achieve moderate accuracy quickly on a readily accessible mirror, vs. performing a high precision measurement, which would require engineering, procurement, integration, and calibration. This measurement will provide a quick

experimental result for our research program, and provide experience and a basis for more accurate and detailed measurements.

- First, assemble a breadboard imaging polariscope with high extinction polarizers and scientific grade camera and develop mounts to integrate to hold the polariscope and perform the measurement. This can be accomplished with existing equipment in the Polarization Laboratory. Document the breadboard polariscope design, engineering build parameters, measurement process and the physical optics scientific measurement results to demonstrate the measurement technique, its accuracy and relevance to coronagraph contrast.
- Install the breadboard polariscope at the center of curvature of the mirror and map the light coupled between orthogonal polarizations, or if the coupled light is at our noise floor, place an upper limit on the coupled light. Look for indications that such coupled light is due to form birefringence or identify other possible causes, such as roughness, scattering, or contamination.
- Apply the results of the form birefringence simulations to estimate the magnitude of the mirror's form birefringence or place an upper limit.
- Investigate to see if we can translate the form birefringence measurements to a space-telescope coronagraph primary mirror. Calculate the intensity profiles across the image plane for each of the four polarization terms: I_{XX}, I_{YY}, I_{XY} and I_{YX}. Comment on the effects of form birefringence on exoplanet characterization.
- Perform statistical error analysis on the apparatus and on the measurements to assess the accuracy and precision of the spatial distribution of the form birefringence measurements across the "typical" astronomical large primary mirror.

7. Experiment description

7.1 Introduction

This section provides both a description of the experiment and a description of the engineering, science and technology environment that this work will be performed within.

7.1.1 Telescope primary mirror measurement

Develop a metrology breadboard to measure the spatial distribution of the form birefringence from a large (3.8-m) mirror with a "typical" astronomical coating. Apply the breadboard to estimate the spatial dependence of the polarization-coupling coefficient within as-built coronagraphs for LUVOIR and HabEx. Achieve a measurement sensitivity of 1-milli-fringe at 500nm.

This task will use the metrology geometry proposed in 2004 by Breckinridge[61]. A 3.75 m diameter spherical mirror with a high reflective metal coating and a radius of curvature of 25.5 meters is available to our team at the U of AZ Steward Observatory Mirror Lab. The polarization reflectivity across the aperture at spatial frequencies appropriate for coronagraphy will be measured. A schematic of the test is shown in Figure 27 (left). The effects of mirror-coating induced anisotropies on coronagraph system performance will be evaluated and mitigation options recommended. These physical measurements will be inserted into the POLARIS-M modeling code to determine the impact of this polarization aberration of the wavefront and image formation, and the magnitude of the form birefringence scaled to generate coating specifications and tolerances for high contrast imaging. This mirror is currently used part-time to test optical

surfaces at the Mirror Lab at the University of Arizona. It is permanently fixed near the ceiling of an optical test tower. Figure 27 (right) shows a schematic of the mirror lab testing facility.

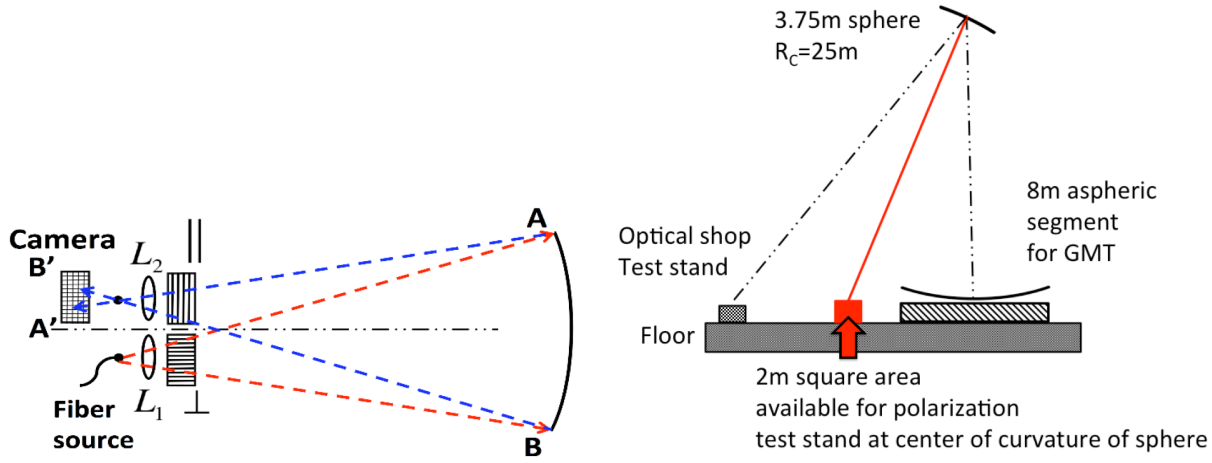

Figure 27 (Left) shows a large mirror at the right illuminated with linearly polarized from the left by light from a fiber optic point source, which fills the aperture from just below the center of curvature. A digital camera just above the center of curvature records an image of the mirror surface as viewed through a rotating polarizer. On the right, we see that the 3.75-meter spherical test mirror at the U of A mirror lab is hung facing down. For routine optical testing of the wavefront, light from the optical test stand to the left expands to fill and reflect from the 3.75-meter mirror onto the 8-meter mirror under test. The center of curvature of the test mirror is located in an open area between the optical shop test stand and the 8-meter mirror under test. This center of curvature is about 1 meter off the floor. A two-meter square area around the location of the center of curvature has been made available for our work.

The coating was deposited with a spatially varying non-normal angle, which varies across the mirror. Therefore, a distribution of form birefringence is anticipated. The test is done from the center of curvature to avoid the Fresnel effects encountered when light strikes a surface at an angle. Rays from the center of curvature strike and reflect from the curved surface at normal incidence.

In the absence of form birefringence, the polarization of rays from the center of curvature to should be unchanged by reflection, since the rays are incident very close to normal incidence; the Fresnel coefficients are equal in both polarizations, and the Fresnel diattenuation and retardance polarization aberrations would be zero. In Figure 27, (left) the numerical aperture of the fiber laser source is modified by lens L_1 to fill the spherical primary mirror at the right from its center of curvature. The light expands passing through a high-quality crystal polarizer aligned perpendicular to the meridional plane to fill the mirror under test. The light returning from the large spherical mirror passes through a second-high quality linear polarizer orthogonal to the linear polarizer in the out-going beam. Lens L_2 images the large telescope mirror onto the focal plane of the digital camera. Form birefringence will cause dark and light patches in the mirror image, and the orientation and ellipticity of the polarization of the reflected light is measured by rotating the polarizer 2. The measurement is repeated at several orientations of polarizer 1.

The mirror is used occasionally to test the off-axis mirrors being fabricated on the 8-meter grind, polish and figure station shown on the right. The optical test stand from which measurements are made on the 8-meter mirror is located to the left. The center of curvature of

the mirror is used very seldom and it has been made available for the brief polarization tests required in this proposal. A series of 8-meter off axis mirrors will be made for the GMT telescope project over the next several years, assuring that the 3.75-meter mirror will remain in position for several years. Other mirrors are also likely to come available for form birefringence measurement.

This test will demonstrate the likely inadequacy of current processes to meet the requirements imposed by a high-performance coronagraph. New processes unique to the needs of space coronagraphs may have to be developed for coating the primary mirror to control polarization-induced scattered light.

7.2. Laboratory form birefringence measurements

Space-based exoplanet coronagraphs need to be opto-mechanically packaged within a spacecraft faring. To achieve the long effective focal lengths necessary to build physically realizable occulting masks and to create the "dark-hole" require optical layouts with long path-lengths. But space-craft fairings which enclose the instrument need to be small to fit the telescope/instrument system into a cost-effective launch vehicle. These two requirements lead to large number of fold mirrors in the optical path. For example, the WFIRST-CGI system has 31 reflections to give a system transmittance of ~8%. As far as power collected the 2.4-meter telescope becomes an effective 5 cm aperture! Clearly technology that provides insight into how to reduce the number of reflections and to increase the reflectivity at each surface is important.

Small mirrors will have their form birefringence characterization in (1) our Mueller matrix imaging polarimeter (see Fig 36 on pp 61), and (2) Axometrics spectropolarimeter. The Mueller matrix will be measured at multiple orientations as the mirror is rotated about the normal, and the resulting information used to determine the dielectric tensor, and thus anisotropy, of the coatings using our technique of biaxial ellipsometry[76]

The results of these measurements will be used to develop high performance coating and processing specifications for future space coronagraphs.

7.3 Facilities

7.3.1 Introduction – the College of Optical Sciences

This effort is centered at the College of Optical Sciences, University of Arizona, Tucson, AZ. The College of Optical Sciences of the University of Arizona is described at http://www.optics.arizona.edu/

The academic program of the College of Optical Sciences of the University of Arizona and their facilities dedicated to this research in the optical sciences are described at

http://www.optics.arizona.edu/academics

The Polarization lab, its tasks, faculty, staff, equipment and capabilities are found at:

http://fp.optics.arizona.edu/chipman/

In addition, there is a vibrant academic program that includes a full two-semester graduate course in polarization theory, measurement and applications. Undergraduate students take a 3-unit hands-on polarization laboratory class. Graduate students can earn their MSc and

the PhD specializing in polarization aberrations, device development, image quality, and polarization instrument development.

7.3.2 The Polarization Laboratory.

The College of Optical Sciences of the University of Arizona facilities available to support this work are within the Polarization Laboratory (PL) of the Optical Engineering division, and faculty & staff members of the College. The software and hardware facilities are described here. The polarization lab occupies 750 square feet across 2 lab rooms. Professor Chipman has 5 graduate students, 2 undergraduates and an Associate Research Professor. The PI currently has funding from (1) JPL as a Co-PI for the MAIA space-borne imaging polarimeter due to launch in 2021, (2) from Goddard Space Flight as a Co-PI on the IIP "Compact Submm Wave & LWIR Polarimeters For Cirrus Ice Properties", and three polarization related contracts from industry.

The polarization lab at the College of Optical Sciences, University of Arizona, led by Professor Russell Chipman, Co-Investigator on this project, has several hardware and software tools that will support this coronagraph analysis including the following:

- The Polaris-M polarization analysis software,
- Four Mueller Matrix metrology systems: A UV, a visible, and a near IR imaging Mueller matrix polarimeters, and a commercial Axoscan spectropolarimeter,
- A remote sensing Stokes imaging photopolarimeter, the NASA "GroundMSPI flight hardware",
- A comprehensive collection of polarization elements, instruments, crystals, and devices.

The University of Arizona Polarization Laboratory is a recognized leader in polarization engineering and polarization measurement. Lead by Dr. Russell Chipman, our state-of-the-art polarization measurement facilities complement our modeling capabilities through ray tracing with measured components. Measurements assist in the verification of algorithms.

7.3.3 Optical Analysis Software.

The optical analysis work will be primarily performed using Polaris-M, with some supporting work performed with **Code V**. Optical designs for WFIRST-CGI and Habex will be delivered in Code V format and initially verified with Code V. **Zemax** is also available in the Polarization Laboratory.

7.3.4 The Polaris-M Optical Analysis Software.

The Polaris-M polarization ray trace software was developed specifically for in sophisticated polarization modeling. The core program and its modules are written in Mathematica. It has the standard features of commercial optical design software, as well as the capability to calculate the propagation of polarized light through uncoated and multilayer coated interfaces, such as uncoated lenses, enhanced reflection coatings for space, polarizing beam splitters, etc. realistic models of the on and off-axis characteristics of dielectric stacks on metals and crystal polarizers. For the WFIRST-CGI analysis, the unique capabilities for (1) biaxial materials, (2) anisotropic thin films, and (3) spatially varying thin films, will be applied to the simulation of form birefringence.

The original development of Polaris-M was supported under a grant of $1.2 million from the Science Foundation Arizona. A team of eight graduate students and scientists developed the

original code over three years. Since that initial grant, additional capabilities have been added to enable features specific to other projects. For this project, the required capabilities are already in place, but it is inevitable that additional enhancements will be required as this task moves forward.

In 2016 Polaris-M was licensed Airy Optics Inc., a startup founded by R. Chipman. Airy Optics is continuing the development and commercialization of Polaris-M. The Polarization Laboratory uses Polaris-M free of charge and accesses the most current versions, so there is no charge for this software to this TDEM contract.

Other commercial programs such as Code V and Zemax were originally designed for purely "conventional" geometrical ray tracing analysis, particularly for imaging systems, and polarization was later attached, but the polarization features are not as thoroughly integrated or as extensive as Polaris-M.

Some commercial software claims wide-ranging capabilities, but many polarization bugs have been documented or are suspected. Usually programs do not state in detail how the computations are done and which algorithms are used, leading to questions about accuracy. With Polaris-M we have access to the source codes, so testing and checking algorithms will be part of the project. Accuracy is particularly important for the WFIRST-CGI system, if we are to control unwanted radiation with high certainty to levels of 1 part in 10^8 or greater (for WFIRST-CGI) and 10^{11} or greater for Habex and LUVOIR.

7.3.5. Polarization Modeling Capabilities

Features of Polaris with particular application to the WFIRST-CGI analysis are detailed below.

- **Optical Thin Films**

Polaris incorporates a full suite of capabilities for analyzing multilayer thin films, which are calculated on the fly at ray intercepts during the ray trace. Figure 28 shows an example of the spectral and angle of incidence performance of an 18-layer high reflection coating. The diattenuation and retardance calculated by these routines are the polarization aberrations of greatest interest to coronagraph polarization analysis. Spatially varying coatings can be analyzed with coating prescriptions that vary across mirror apertures. Small low spatial frequency variations of refractive index of Al coatings resulting from the coating deposition process would introduce troublesome near angle diffracted light, with obvious implications for coronagraph performance.

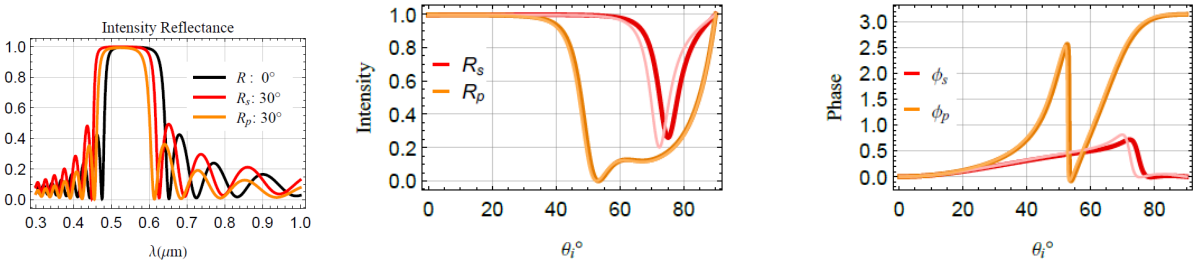

Figure 28 (left) Intensity reflectance of an 18-layer reflection enhancing coating versus wavelength. Intensity reflectance (middle) and phase change (right) of 18-layer reflection enhancing coating versus angle of incidence at 0.55µm (darker colors) and 0.7µm (lighter colors).

- **Polarization aberrations and Jones pupils**

Polaris performs ray-tracing using three-dimensional polarization ray tracing calculus algorithms for refraction, reflection, and interactions with birefringent crystals, diffraction gratings, polarizers and retarders, thin-films, and other polarizing media. Full polarization information in the form of a three-dimensional polarization ray trace matrix is calculated in the exit pupil and converted to arrays of Jones matrices called Jones pupils that characterize the optical system's polarization aberrations. Polaris-M can then further decompose the Jones pupils into polarization generalizations of Zernike polynomials. Both sequential and non-sequential ray tracing can be performed. The figure the result of a nonsequential ray trace of a solid corner cube and the polarization variation between subapertures.

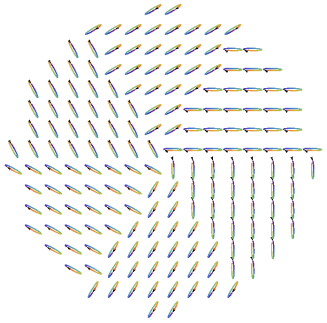

Figure 29 Polarization state exiting a solid hollow corner-cube retroreflector when circular polarization is incident.

- **Polarization point spread matrices and optical transfer matrices**

Polaris-M diffracts Jones pupils to obtain the point-spread function in the form of Jones matrices or Mueller matrices that describe image formation for all polarization states. These are further processed to calculate optical transfer matrices, since the spatial frequency response of these systems also depends on the incident and analyzed polarization states.

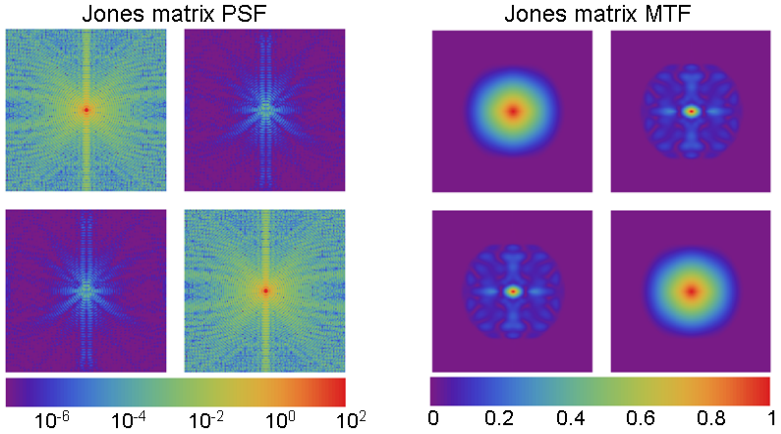

Figure 30 A Jones matrix point spread matrix (left) showing the effect of a realistic stress birefringence model on a lens' image (right). The associated modulation transfer functions (MTF) are shown for four combinations of entrance and exit pupil polarizers.

- **Anisotropic materials**

Polaris-M has sophisticated models of uniaxial, biaxial, and optically active materials. In particular, the amplitude coefficients for reflection and refraction into all the modes are exactly calculated, something no other software is at present performing. An example is shown below. This is important for WFIRST-CGI since one of our models for form birefringence is to treat the aluminum as a biaxial material with spatially varying indices and orientation, a simulation the other programs are not currently performing. Polaris-M also models multilayer films with anisotropic layers, such as the form birefringence, which might occur in layers overcoated on aluminum or silver astronomical mirrors, as is shown in Fig 31, below.

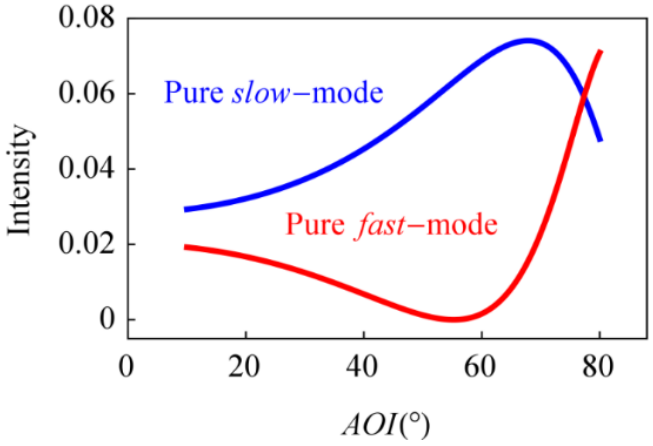

Figure 31 Intensity reflection coefficients from a particular biaxial crystal as a function of angle of incidence.

Summary of other capabilities are shown in Figs 32 and 33.

– **Ray doubling:** Ray doubling occurs reflecting and refracting from anisotropic materials, and the tracking of the resulting ray trees is handled automatically in Polaris-M, shown here in a pair of Glan-Taylor polarizers, and then in a biaxial crystal.

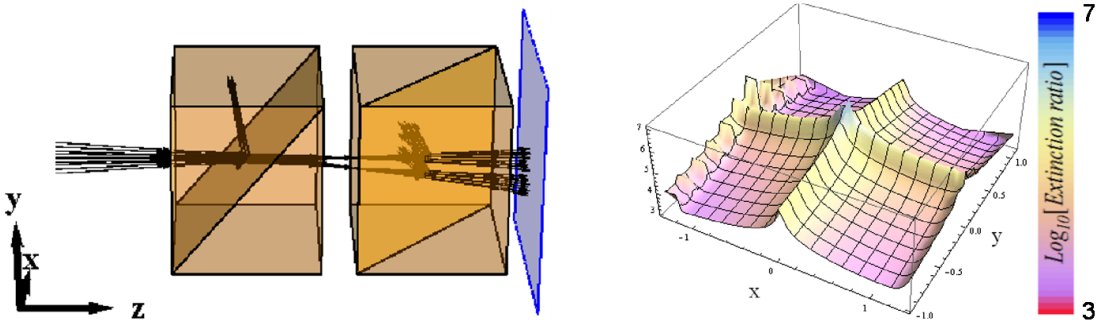

Figure 32 (left) Circularly polarized rays traced through two Glan-Taylor polarizers with crossed axes. (right) Extinction ratio varies considerably across a ±3° field of view.

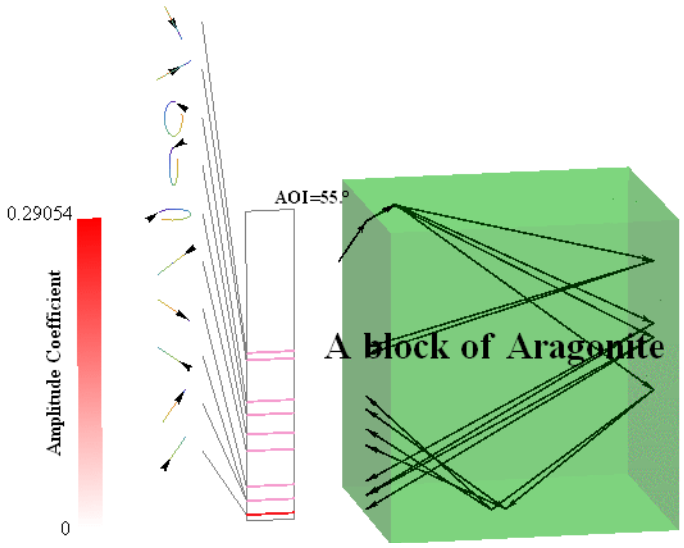

Fig 33 A single ray incident on a block of aragonite crystal reflects and splits multiple times before exiting the original surface. The exiting polarization ellipses and amplitudes (pink) are shown for each sequence of modes.

- **Stress Birefringence:** Stress data is imported from finite element modeling programs and operated on during the polarization ray trace. Effects of full stress tensors and stress gradients are computed and their effects on polarization evaluated in this example of a lens in a polariscope with index matching fluid. This is shown in Fig 34.

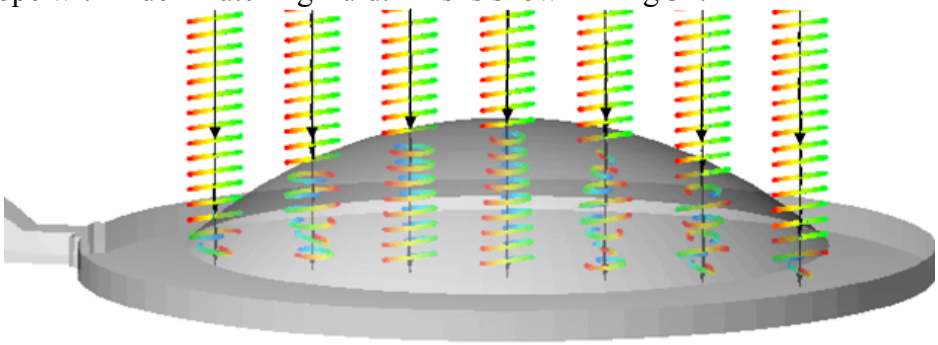

Figure 34 A line of rays propagating through a finite-element model of stress-birefringence in a lens. Polarization changes on propagation depend on local stress tensor. Element is in index matching fluid so rays are undeviated at surfaces.

- **Rigorous Coupled Wave Theory:** Realistic models of diffraction gratings, sub-wavelength structures, and holographic optical elements are calculated during the ray trace with an integrated RCWA routine, as seen in the tilted wire grid polarizer example shown in Fig 35, below:

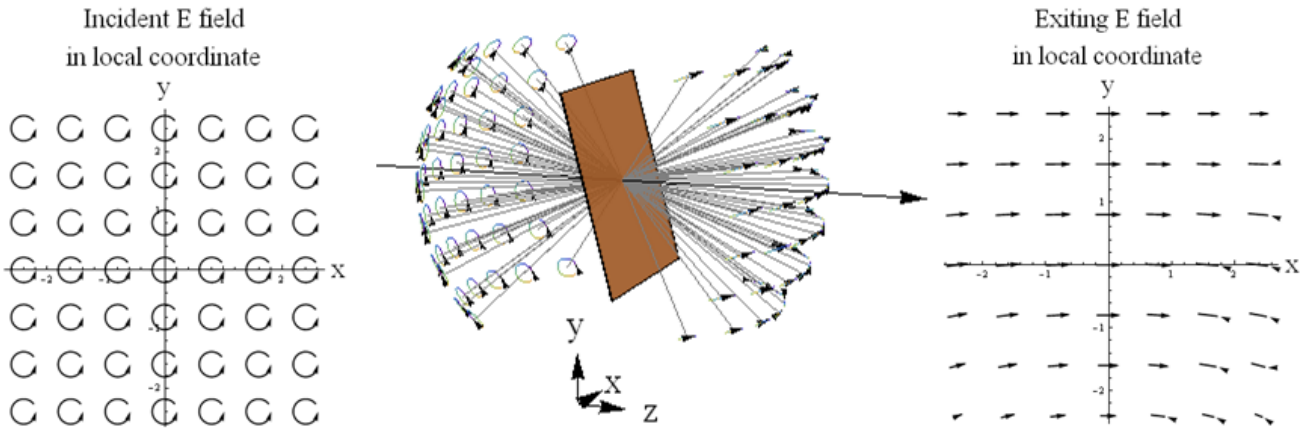

Fig 35. Focused circularly polarized rays' incident on a tilted wire grid polarizer show light leakage at large angles.

- **Low Polarization Thin-Film Coatings Design:** Design and verification of multi-layer thin-film coatings with low polarization properties and effective reflectivity performance to reduce polarization sensitivity and polarization aberrations.
- **Polarizer Models:** Realistic wire grid, crystal, and plastic sheet polarizers and crystal and diffractive retarders are constructed for accurate simulation of angle and wavelength effects.

All of the analysis work completed for the recent paper "Breckinridge, Lam and Chipman, Polarization aberrations in astronomical telescopes: the point-spread function. PASP 127:445-468 2015" was performed using Polaris M.

7.3.6 Mueller matrix polarimeters

The Polarization Laboratory contains one visible, one UV, and one near IR Mueller matrix spectral imaging polarimeters, custom instruments built within the laboratory. These Mueller matrix spectropolarimeters map the polarization properties of mirror coatings, beam splitters, optical subassemblies, and entire optical systems. The layout and measurement configuration are shown below along with a sample Mueller matrix data set of an injection-molded lens showing the measurement of the spatial variation of retardance. Our in-house Mueller matrix spectropolarimetry is used to measure mirror coatings, beam splitters, and optical subassemblies.

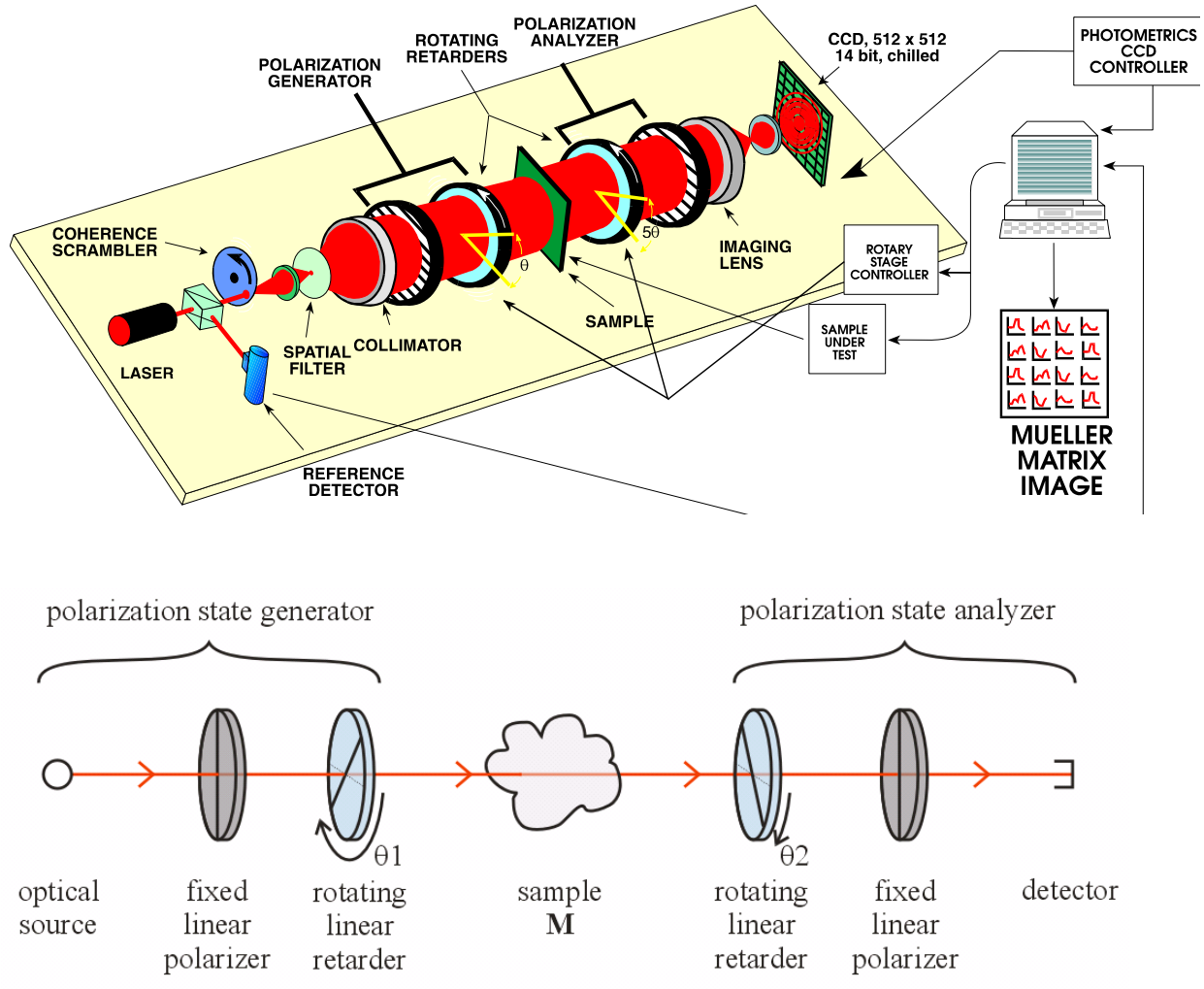

Figure 36 (Left) Schematic of the Mueller matrix imaging polarimeter, based on (right) the dual rotating retarder configuration.

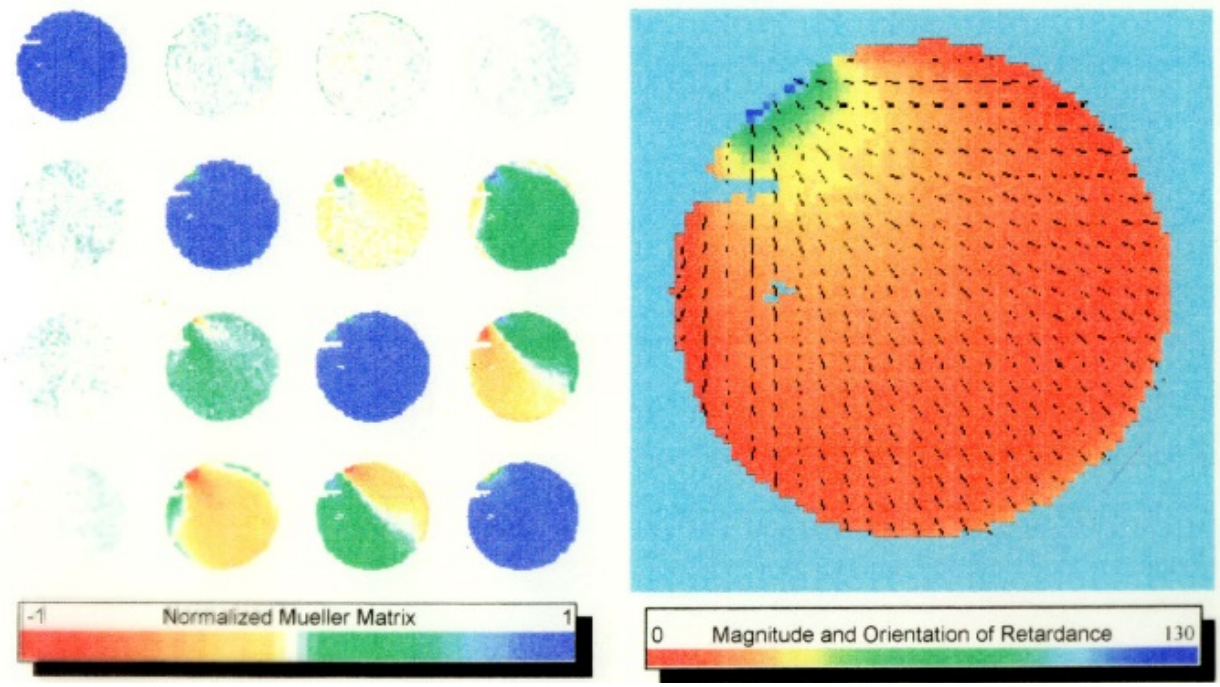

Figure 37 (Left) Example Mueller matrix image of an injection molded lens with stress birefringence, and (right) the corresponding retardance map.

Imaging polarimetry spatial resolution can be configured up to a spatial resolution of 0.6 µm/pixel. Samples up to several inches in size have been measured by stitching polarization images. Measurement capabilities include transmissive and reflective samples with any incident and exiting angles further than 10° from normal.

– **Biaxial Ellipsometry:** Complete characterization of the orientations and complex indices of refraction of general biaxial thin films and substrates.

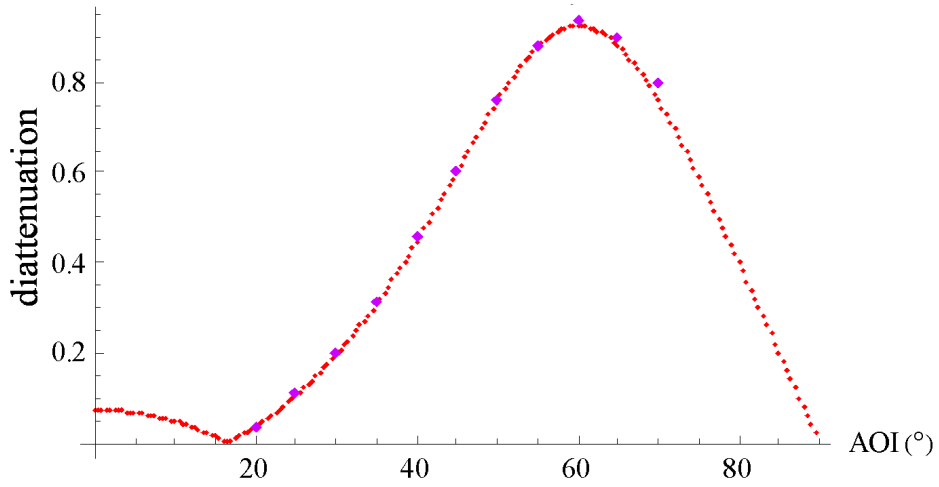

Figure 38: Comparison of polarization diattenuation measurement (purple dots) and ray-trace results (red line) for 293 nm of TiO_2 coated on to a crystal calcite substrate (✦= 550nm)

7.3.7 A COMMERCIAL AXOSCAN SPECTROPOLARIMETER

The Polarization Laboratory also has an AxoScan Mueller matrix spectropolarimeter from Axometrics (Huntsville, AL) that records four Mueller matrices per second and scans wavelength from 400 to 850 nm. This instrument is shown in Fig 39, below.

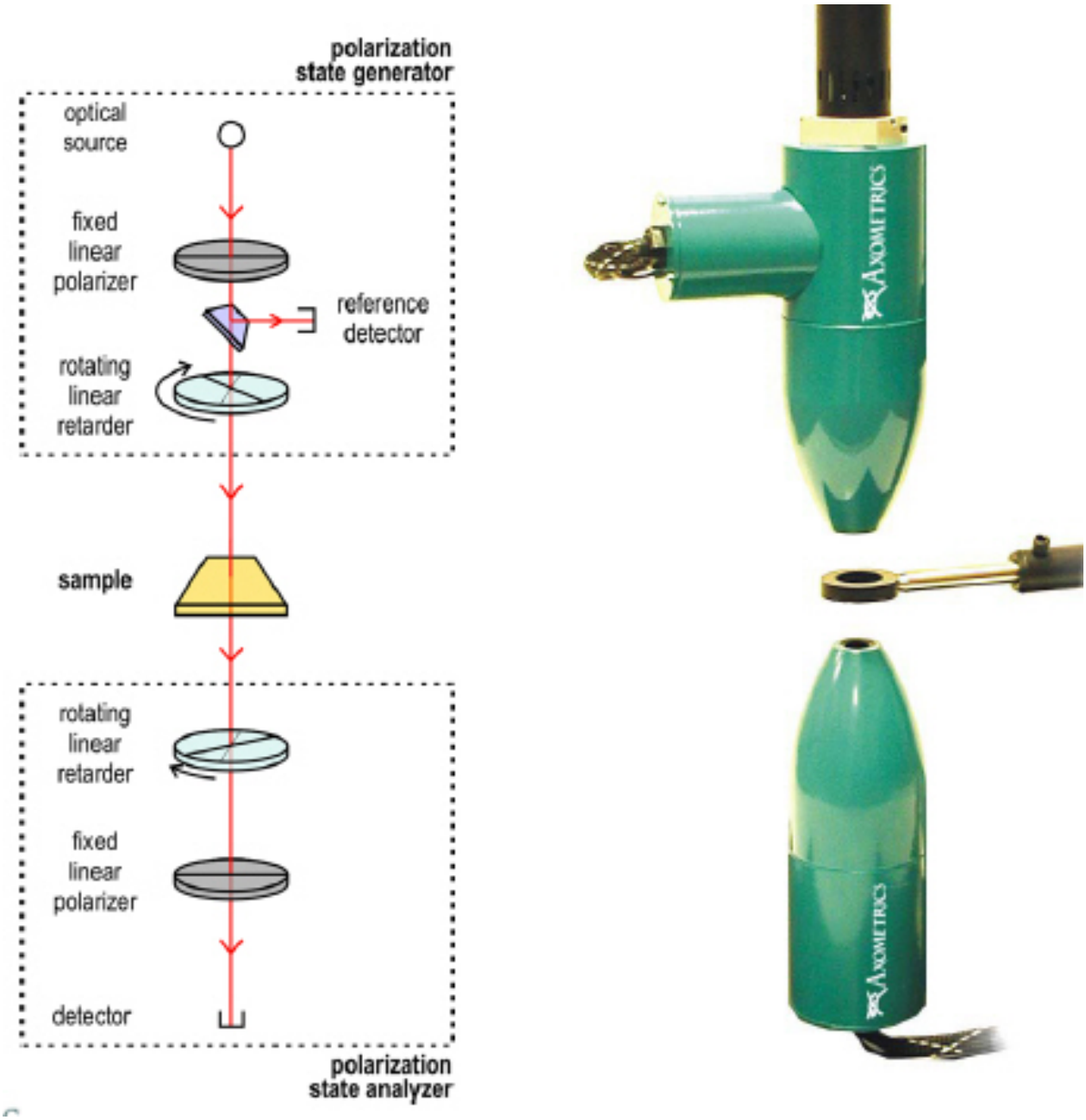

Figure 39 The Axoscan Mueller matrix spectropolarimeter is a flexible polarization characterization instrument.

In addition to these strong analysis and software capabilities the Polarization Laboratory has extensive polarization metrology apparatus currently supporting projects from NASA, industry, academia and other government agencies.

7.3.8 Polarization state generators

The Laboratory has built and delivered two Polarization State Generators (PSG) using tilted glass plates to generate low degree of linear polarization (DOLP) states. The first PSG used one plate. The second PSG uses two plates in a V configuration which compensates for angle on incidence, as the angle increases on the first plate, it decreases on the second. For stability, separate plate pairs were fabricated and mounted for each DOLP of 0, 1, 5, 10, and 20%. The PSG had an aperture of 48 mm and operates from 320 to 2200 nm. These are shown in Fig 40.

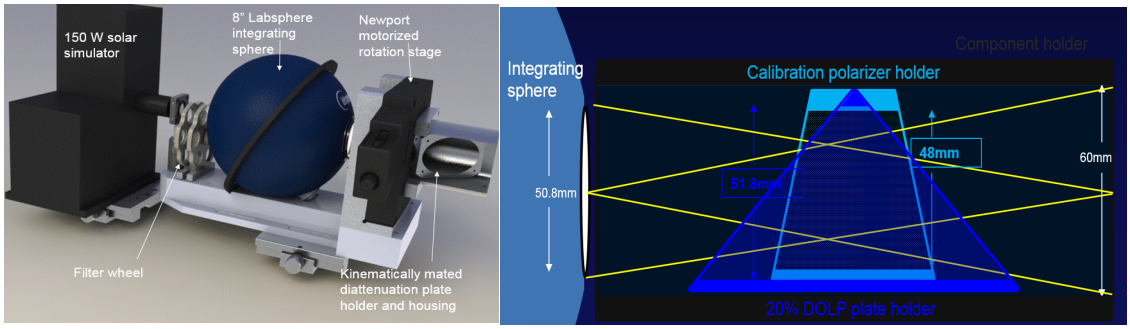

Fig 40. (left) Second generation polarization state generator for calibrating optics. (right) One of four pairs of plates in a V configuration for converting unpolarized light from the integrating sphere into a calibrated DOLP of 1%, 5%, 10%, or 20%.

8.0 Data measurement & analysis

8.1 Data for the form birefringence measurement will be made using the methods and apparatus described in section 7. Analysis of the data will be performed using the usual standards for data interpretation.

8.2 Output from the analyses performed for WFIRST-CGI & LUVOIR & HabEx will be in a form similar to that provided here in "**5.2.9 Quantitative analysis of a three-mirror bent Cassegrain: An Example" and in particular will include:**

1. Figures 13 and 14 retardance and diattenuation maps
2. Figure 15 exit pupil maps of amplitude and phase
3. Figure 16 Amplitude response matrix
4. Figure 17 cross section PSF profile
5. Figure 18 Log_{10} of intensity as a function of radial position in the image plane for any of the 4-polarization aberration PSF's.
6. Figure 18 Field distribution across PSF's
7. Other graphics as needed to provide both a quantitative as well as an intuitive understanding of the physics of image formation in exoplanet imaging coronagraphs.

9.0 Success Criteria

1. Introduction
2. **Four component intensity profiles**

Let $\delta(x,y)$ define the difference in the four component intensity profiles as follows:

$$\left.\begin{aligned}
\delta(x,y)_{XX} &= \left| \left\{ \underline{I_3(x_3,y_3)}\big|_{XX} \right\}_{Code-V} - \left\{ \underline{I_3(x_3,y_3)}\big|_{XX} \right\}_{Polaris-M} \right| \\
\delta(x,y)_{YY} &= \left| \left\{ \underline{I_3(x_3,y_3)}\big|_{YY} \right\}_{Code-V} - \left\{ \underline{I_3(x_3,y_3)}\big|_{YY} \right\}_{Polaris-M} \right| \\
\delta(x,y)_{YX} &= \left| \left\{ \underline{I_3(x_3,y_3)}\big|_{YX} \right\}_{Code-V} - \left\{ \underline{I_3(x_3,y_3)}\big|_{YX} \right\}_{Polaris-M} \right| \\
\delta(x,y)_{XY} &= \left| \left\{ \underline{I_3(x_3,y_3)}\big|_{XY} \right\}_{Code-V} - \left\{ \underline{I_3(x_3,y_3)}\big|_{XY} \right\}_{Polaris-M} \right|
\end{aligned}\right\} \qquad \text{Eq. 43}$$

The four profiles of $\delta(x,y)$ given in Eq. 43 are the differences in the intensity profiles: Code-V minus Polaris-M and define a comparison metric to evaluate Code-V against Polaris-M. This metric will be used in Milestone # 1 to compare the polarization calculations of Polaris M with those of CODE-V.

Unit intensity in the XX component of the PSF is assumed for the normalization. The calculated Code V and Polaris-M PSFs will vary over orders of magnitude. We proposed this simple metric to allow program management to have a straightforward yes/no test to identify a substantial disagreement.

If $\delta(x,y)$ exceeds 0.03 or 3%, a brief investigation into the cause will be made.

3. polarization reflectivity isotropy (form birefringence)

Develop a metrology breadboard to measure the spatial distribution of the form birefringence from a large (3.8-m) mirror with a "typical" astronomical coating. Apply the breadboard to estimate the spatial dependence of the polarization-coupling coefficient.

Achieve a measurement sensitivity of 1-milli-fringe at 500nm.

10. Schedule

1. WFIRST-CGI polarization ray trace.
   1.1. The electric field just in front of the WFIRST-CGI occulting mask image plane will be determined for a reference baseline design 1.0 using polarization aberration ray trace by June 30, 2017.
   1.2. The electric field at the detector plane of the WFIRST-CGI telescope/coronagraph system will be determined for a reference baseline design for the coronagraph that uses the same reference baseline design for the fore-optics in part 1.1. This will be completed within approximately an additional 8 weeks (~the middle of September, 2017) after receipt of the coronagraph design, including the profile for the occulting mask and the profile for the Lyot stop.

2. Polarization ray trace LUVOIR/HabEx
   2.1. As soon as the HabEx and LUVOIR teams have quasi-stable designs we will polarization ray trace them and report our results to the teams and report our results on a "real-time" basis.

3. Characterize form birefringence to tolerance contrast
   3.1. Schedule depends on the availability of the optical test facility at the U of A mirror lab. Under negotiation now, but access is expected within the next 6-months and we expect measurements and analysis results by November 1, 2017.

4. ExoPlanet imaging polarization mitigation
   4.1. During the course of our work we will provide the design engineering teams with recommendations on how to mitigate polarization aberrations during their work. Annual report will be prepared

11 Program office technology development plan

A. Close the gaps: This work addresses the technology needs described in the Technology Development Plan Rev B as follows.
B. From Table 3 in the Technology Development Plan Rev B, where our work supports: technologies: CG-2 (Suppress diffracted light $<10^{-9}$ at visible and IR wavelengths; CG-6 mirror segment phasing & control; CG-10 Mirror coatings

3	CG-2	**Coronagraph Demonstrations and Modeling**	Coronagraph optics and architecture that suppress diffracted starlight by a factor of $< 10^{-9}$ at visible and infrared wavelengths	Lab: 6×10^{-10} raw contrast at 10% bandwidth across angles of 3-15 λ/D demonstrated with a linear mask and an unobscured pupil in a static vacuum lab environment (Hybrid Lyot) $< 1.6\times10^{-9}$ raw contrast at 10% bandwidth across angles of 3-9 λ/D demonstrated with a circularly-symmetric mask and obscured pupil in a static vacuum lab environment (WFIRST) Flight: 10^{-4} raw contrast 540 nm at 10 λ/D (HST)	Coronagraph masks and optics capable of creating circularly symmetric dark regions in the focal plane enabling raw contrasts ≤ 10^{-9}, with minimal contribution from polarization aberration, IWA ≤ 3 λ/D, throughput ≥ 10%, and bandwidth ≥ 10% on obscured and segmented pupils in a simulated dynamic vacuum environment.

Polarization ray-trace analysis of optical systems will enable: 1. An accurate demonstration of coronagraph performance and 2. An accurate model of the instrument system performance. In the case of WFIRST-CGI this technology development work will enable the specification and development of an occulting mask whose performance, in terms of end-to-end system contrast, is optimum in the presence of polarization aberrations. Accurate modeling will enable polarization mitigation analysis and guidelines for the opto-mechanical layout and a more accurate calculation of science mission yield.

Priority	ID	Title	Description	Current Capabilities	Needed Capabilities
3	CG-6	**Mirror Figure/ Segment Phasing Sensing & Control**	Segmented or monolith large aperture mirrors require segment phasing and rigid-body sensing and control of the segments or the surface figure to achieve tight static and dynamic wavefront errors.	6 nm rms rigid body positioning error and 49 nm rms stability (JWST error budget) SIM and non-NASA: nm accuracy and stability using laser metrology No flight SOA; ground-based (Keck) achieved 6 nm positioning error in operations	Systems-level considerations to be evaluated but expect will require WFE stability less than 10 pm rms sensitivity and control over periods of tens of minutes

Polarization aberrations change the shape of the wavefront in a manner that cannot be completely corrected using figure sensing and control. Laser light used for optical metrology and wavefront sensing is linearly polarized and will "see" a slightly different OPD than the white-light science signal. Polarization aberrations may affect metrology accuracy. Although this is not specifically addressed in this work our polarization aberration study provides the tools for further analysis in this important area.

7	CG-10	**Mirror Coatings for UV/NIR/Vis**	Mirror coatings that enable high reflectivity to wavelengths as short as 90 nm	Al coating with combination of MgF_2, LiF, and/or AlF_3 overcoat: 90-120 nm: < 50% reflectivity 120-300 nm: 85% reflectivity 300 nm-2 µm: > 90% reflectivity Polarization differences between orthogonal polarization states, uniformity, and durability of coatings on large optics is unknown. Flight: HST uses MgF_2; 85% reflectivity λ > 120 nm; 20% reflectivity λ < 120 nm	A mirror coating that that achieves 90-120 nm: > 70% reflectivity 120-300 nm: > 90% reflectivity 300 nm-2 µm: > 90% reflectivity Polarization phase and amplitude difference < 1% between orthogonal polarization states.

The development of mirror coating requirements and fabrication specification for the dielectric/metal reflecting system will be supported within the frame work of high reflectivity isotropic films and their anisotropic component: form birefringence using polarization ray-tracing software applied to end-to-end coronagraph system.

A. A relation of this work to the planned Decadal Survey Testbed (see section B.1 of the Technology Plan Appendix) https://exoplanets.nasa.gov/exep/technology/technology-overview/ for a description)
    B. What is the relationship to ground-based coronagraphs?
        a. Coronagraphs are commonly used on the ground to image the solar corona. The new Daniel K. Inouye solar telescope, on Haleakela relies on polarization preserving optics for precision measurements of solar magnetic fields and to deliver high quality images. Polarization aberrations affect the quality of science data recorded with this telescope. Calculations of the magnitude of these effects and their mitigation are in progress now.
        b. Polarization aberrations will affect the performance of ground-based exoplanet coronagraphs. Depending on the number of mirrors, the coating properties of reflecting surfaces, and the opto-mechanical layout polarization effects may dominate system performance. Pursuing investigations of ground-based systems is out of scope of this work. However, the tools and mitigation methodologies developed under support of our investigation on space telescopes do have application to ground-based

12. List of Acronyms

Abbreviation	Meaning
&	and
A/O	Adaptive optics
AFTA	Astrophysics telescopes assembly
Ag	Silver
AJ	Astronomical Journal
Al	Aluminium
AO	Applied Optics
ApJ	Astrophysical journal
ARM	Amplitude response matrix
AZ	Arizona
BW	Optical bandwidth
CAD	Computer aided design
Caltech	California Institute of Technology
CDR	Critical design review
Co-I	Co-investigator
CODE V	Commercial ray-trace CAD program
COS	College of Optical Sciences
DOLP	Degree of linear polarization
E&M	Electricity & Magnetism
EISC	ExoPlanet Imaging System
ExoTag	ExoPlanet Program Technology advisory group
F/#	f-ratio number
Fore-optics	Those optical elements before the occulting mask image plane (OMIP)
GSFC	Goddard Space Flight Center - NASA
HabEx	Habitable Exoplanet Explorer
HZ	Hertz or cycles per second
IR	Infrared
JATIS	Journal of astronomical telescopes instruments and systems
JOSA	Journal of the Optical Society of America
JPL	Jet Propulsion Laboratory - NASA
LUVOIR	Large Ultraviolet Optical Infrared
mas	milli-arc second
MNRAS	Monthly notices of the Royal Astronomical Society
NASA	National Aeronautics and Space Administration
NIR	Near infrared
OPD	Optical path distance

Abbreviation	Meaning
OPL	Optical path length
OMIP	Occulting mask image plane
p	parallel (German: Parallelzweig)
pas	pico-arc second
PASP	Publications of the Astronomical Society of the Pacific
PDD	Probability Density Distribution
PDF	Probability density function
PDR	Preliminary design review
Phys. Rev.	Physical review journal
PI	Principal Investigator
pm	Picometer
PolAbT	Polarization aberration theory
POLARIS-M	Polarization ray-trace modeling program version M
Proc.	Proceedings
PRT	Polarization ray trace
PSF	Point Spread Function
PSR	Preship review
RV	Random Variable
s	senkrecht - German for perpendicular
SDT	Science definition team
SNR	Signal-to-Noise Ratio
SPIE	International society for optical engineering
STDT	Science and technology definition team
TMA	Three-mirror anistigmat
TPF	Terrestrial Planet Finder
U of A	University of Arizona
UV	Ultra-violet
vol.	Volume
WFIRST	Wide field infrared survey telescope
WFIRST-CGI	Wide field infrared survey telescope Coronagraph Instrument
WFIRST-WFI	Wide field infrared survey telescope Wide field instrument
Zemax	Commercial ray-trace CAD program

13. References

[1] Safonov, B. (2015) "On-sky demonstration of optical polar-astrometry", MNRAS **451**, 3161-3172.
[2] Breckinridge, J. B., T. G. Kuper and R. V. Shack (1984) "Space telescope low scattered light camera: a model," Optical Engineering, **23**, 816-820. also Proc. SPIE 331, 395-403, 1982.
[3] Breckinridge, J. B. and B. Oppenheimer (2004), "Polarization Effects in Reflecting Coronagraphs for White Light Applications in Astronomy," ApJ, **600**, pp. 1091 – 1098.
[4] Elias, N. M., and R. Bates and J. Turner-Vale (2004) "Polarization analysis for terrestrial planet finder coronagraph designs", Proc SPIE **5555** pp 248-257
[5] Carson, J. B. Breckinridge, J. Trauger, et. al. (2006) "The effects of instrumental elliptical polarization stellar point spread function fine structure" Proc. SPIE **6265**-3M.
[6] Balasubramanian, K. S. Shaklan, A. Give'on, E. Cady and L. Marchen (2011) "Deep UV to NIR space telescopes and exoplanet coronagraphs: a trade study on throughput, polarization, mirror coating options and requirements" Proc. SPIE **8151** 51511G
[7] Breckinridge, J. WFIRST-CGI science and technology definition team (STDT) 2nd meeting Spring 2011 GSFC
[8] Zimmerman, N. A. J. E. Riggs, N. J. Kasdin, et. al. (2016) "Shaped pupil coronagraphs: high contrast solutions for restricted focal planes", JATIS **2**, 011012
[9] Hong Tang, M. Rud, R. Demers, R. Goullioud, et. al. (2015) "The WFIRST/AFTA Coronagraph Instrument Optical Design", Proc. SPIE **9605** 960504
[10] Breckinridge, J., W.S.T. Lam and R. A. Chipman (2015) "Polarization aberrations in astronomical telescopes" Publ. Astron Soc. Of the Pacific **127**:445-468
[11] Chipman, R. A., Wai Sze T. Lam and J. Breckinridge (2015) "Polarization aberrations in astronomical telescopes" Proc SPIE **9613** doi:10.1117/12.2188921
[12] Sasian, J. (2015) "Introduction to Aberrations in Optical Imaging Systems", Cambridge University Press
[13] Grievenkamp, J. (2003) *Field Guide to Geometrical Optics*, SPIE Press, Bellingham WA.
[14] Goss, H. (2005) Handbook of Optical Systems, Vol **1**: Technical Optics, Wiley-VCH Verlag GmbH & Co.
[15] Slyusarev, G. G. (1969) Aberration and Optical Design Theory, Adam Hilger, Ltd. Bristol
[16] Gardner, I. C., "Application of the algebraic aberration equations to optical design," *Scientific Papers for the Bureau of Standards* **22,** 73–202, Washington, DC, United States Government Printing Office. (1927).
[17] Purcell, E. M. and D. J. Morin (2013) "Electricity and Magnetism", Cambridge University Press, 363 pages
[18] Goodman, J. W. (2005) "Fourier Optics" Roberts and Company book ISBN 9747077-2-4
[19] Gaskill, J. D. (1978) "Linear Systems, Fourier Transforms and Optics", John Wiley & Sons, NY 400 pages.
[20]Chipman, R. A. & W. T. Lam (2015) Balancing aberrations in crossed fold mirrors, Applied Optics, **54**, 3236 to 3245.
[21] Strong, J. (1958) "Concepts of Classical Optics", pp 178 section 8.9. W. H. Freeman, London,
[22] Born, M. & E. Wolf (1993) "Principles of optics", Pergamon Press– Fresnel Equations are derived on pp 627-633
[23] Ward, L. (1988) "Optical Constants of Bulk Materials and Films", Adam Hilger, Bristol and Philadelphia, 245 pp
[24] Thelen, A. (2002) "Design of Optical Interference Coatings" (McGraw-Hill, New York, 1988). AND H. A. Macleod, "Thin-Film Optical Filters" Institute of Physics, pp. 185–186. AND J.A. Dobrowolski, "Coatings and Filters," in Handbook of Optics, W.G. Driscoll and W. Vaughan, ed.(1978) (McGraw-Hill, New York), 8.1-8.124.
[25] R. M. A. Azzam and N. M. Bashara (2003) "Ellipsometry and Polarized Light", North Holland – Elsevier ISBN 0 4444 87016 4; 527 pages.
[26] Lyot, B. (1931), "Photography of the solar corona outside eclipse", COMPTES RENDUS HEBDOMADAIRES DES SEANCES DE L ACADEMIE DES SCIENCES Volume: **193** Pages: 1169-1172
[27] Jones, R. C. (1941) "A New Calculus for the Treatment of Optical Systems: I. Description and Discussion of the Calculus", JOSA, **31**, 488
[28] Wolf, E. (2007) "Theory of Coherence and Polarization of Light", Chapter 8, Cambridge University Press, 225 page book. And Goodman, J. W. (2015) "Statistical Optics", Wiley And Strong, J. D. (1958) "Classical Optics", Freeman, page 178 interference of polarized light,
[29] McGuire, J.P. Jr., R.A. Chipman (1990) "Diffraction image formation in optical systems with polarization aberrations I: Formulation and example", JOSA A., vol. 7, no. 9, pp. 1614-1626 (Sept. 1990).
[30] Bruegge, T. J. (1989), Proc. SPIE, **1166**, 165
[31] Chipman, R. A. (1989), "Polarization analysis of optical systems", Opt. Eng., **28**, 90 and 1989b, Proc. SPIE, **1166**, 79.
[32] Wolff, L. B. and D. J. Kurlander, (1990), "IEEE Computer Graphics and applications" vol. 10, 6, 44–55.

[33] Trolinger, J.D. Jr., R.A. Chipman, D.K. Wilson, (1991) "Polarization ray tracing in birefringent media", Optical Engineering, vol. **30**, no. 4, pp. 461-466.
[34] Yun, G., Crabtree, K. & Chipman, R., 2011a, Appl. Opt. **50**, 2855 & 2011b, Appl. Opt. 50, 2866
[35] McClain, S.C. , L.W. Hillman, R.A. Chipman, (1993) "Polarization ray tracing in anisotropic optically active media I, algorithms, & II, theory and physics", Applied Optics vol. **10**, no. 11, pp. 2371-2393.
[36] Chipman, R. A. and W. S. T. Lam (2015) "The Polaris-M ray tracing program", Proc. SPIE **9613**-18
[37] Kuboda, H. & Inoué, S. (1959), JOSA, **49**, 191
[38] Urbanczyk, W. (1986), Opt. Acta., **33**, 53
[39] McGuire, J. P. & Chipman, R. A. (1990), JOSA A, **7**, 1614 & 1991, JOSA A, **8**, 6
[40] Tu, Y., Wang, X., Li, S. & Cao, Y. (2012), Opt. Lett., **37**, 2061
[41] Chipman, R.A. , L.J. Chipman, (1989) "Polarization aberration diagrams, Optical Engineering", vol. **28**, no. 2, pp. 100-106.
[42] McGuire, J.P. , Jr., R.A. Chipman, (1994) "Polarization aberrations I: Rotationally symmetric optical systems and Polarization aberrations II: Tilted and decentered optical systems", Applied Optics, vol. **33**, no. 2, pp. 5080-5107.
[43] Reiley, D.J. , R.A. Chipman, (1994) "Coating induced wave front aberrations: On axis astigmatism and chromatic aberration in all reflecting systems", Applied Optics, vol. **33**, no. 10, pp. 2002-2012.
[44] I. C. Gardner (1927) "Application of the Algebraic Aberration Equations to Optical Design", NBS Scientific Papers Vol **22** # 550.
[45] Chipman, R. A. & Chipman, L. J. (1989), Opt. Eng., **28**, 2,
[46] Breckinridge, J. , W.S.T. Lam and R. A. Chipman (2015) "Polarization aberrations in astronomical telescopes" Publ. Astron Soc. Of the Pacific 127:445-468 - Figure 7:
[47] Reiley, D.J. , R.A. Chipman (1994) "Coating induced wave front aberrations: On axis astigmatism and chromatic aberration in all reflecting systems", Applied Optics, vol. **33**, no. 10, pp. 2002-2012
[48] Witzel, G., Eckart, A., Bucholtz, R. M. et al. 2011, A&A, **525**, A130, 1
[49] Goullioud, R., Zhao, F., Tang, H., & Wu, J. 2014, Proc. SPIE, 9143,
[50] Lotsch, H.K. V. (1968) "Refraction and Reflection of a Beam of Light at a Plane interface", JOSA, **58** pp551-561
[51] Horowitz, (1983) "Structural induced optical anisotropy in this films" PhD Dissertation, University of Arizona, Tucson AZ. 117 pages.
[52] Hodgkinson and Wilson (1988), "Microstructural-induced anisotropy in thin films for optical applications" Critical Reviews in Solid State and Material Sciences, Volume 15.
[53] Bielsa & Dupays & Fouche (2009), "Birefringence of interferential mirrors at normal incidence" Appl Phys. B **97**:457-463
[54] Bej & Tervo (2015) "All-optical control of form birefringence", IEEE conference
[55] Smith, S. J. & Purcell E. M. (1953) Visible light from Localized Surface Charges Moving Across a Grating. Phys Rev **92**, 1069, 10.1103/PhysRev.92.1069
[56] Born, M. and E. Wolf (1993) "Principles of Optics" - Form birefringence and absorption in crystals 6th ed. pp706-718.
[57] Dirks, A. G., and H. J. Leamy, "Columnar microstructure in vapor-deposited thin films", Thin Solid Films, **Vol.47**, 219-233 (1977).
[58] Boccas, M., et al., "Coating the 8-m Gemini telescopes with protected silver", Proc SPIE vol. 5494, pp. 239-253, (2004).
[59] Hodgkinson, I., et al., "Empirical equations for the principal refractive indices and column angle of obliquely deposited films of tantalum oxide, titanium oxide, and zirconium oxide", Appl. Optics, **37**(13), pp.2653-2659, (1998).
[60] Hodgkinson, I., et al., "Dispersion equations for vacuum-deposited tilted-columnar biaxial media", Appl. Optics **40(**4), pp. 452-457, (2001).
[61] Breckinridge, James B. (2004), "Image formation in high contrast optical systems: the role of polarization" Proc. SPIE vol **5487**, pages 1337-1345
[62] Rakic A. D. (1995) "Algorithms for the determination of intrinsic optical constants of metal thin films: application to Aluminium", Applied Optics **34**, 4755-4767.
[63] Hagemann, H-J., W. Gudat, and C. Kunz (1975) "Optical constants from the far infrared to the x-ray region: Mg, Al, Cu, Ag, Au, Bi, C, and Al_2O_3", *J. Opt. Soc. Am.* **65**, 742-744
[64] Rakić, A. D., A. B. Djurišic, J. M. Elazar, and M. L. Majewski. (1989) "Optical properties of metallic films for vertical-cavity optoelectronic devices", *Appl. Opt.* **37**, 5271-5283 (1998)
[65] K. M. McPeak, S. V. Jayanti, S. J. P. Kress, S. Meyer, S. Iotti, A. Rossinelli, and D. J. Norris.(2015) "Plasmonic films can easily be better: Rules and recipes", ACS Photonics **2**, 326-333.
[66] S. Babar and J. H. Weaver (2015). "Optical constants of Cu, Ag, and Au revisited", Applied Optics **54**, 477-481
[67] P. B. Johnson and R. W. Christy (1972). Optical Constants of the Noble Metals, Phys. Rev. **B6**, 4370-4379

[68] Gee, J. R., I. J. Hodgkinson and P. W. Wilson (1985) "Reflection anisotropy in evaporated Aluminium: Consequences for telescope mirror coatings". J. Vac. Sci. Technology vol 4, Jul/Aug 1986.
[69] Goodman J. W. (2005) "Fourier Optics" Chapter on optical matched filters, Roberts and Company book ISBN 9747077-2-4
[70] Safanov, B., (2015) "On-sky demonstration of optical polar-astrometry", MNRAS, **451**, 3161-3172
[71] Safanov, B., (2016) private communication
[72] Clark, N. , J. B. Breckinridge (2011) "Polarization compensation of Fresnel aberrations in telescopes", SPIE Vol **8146**, 11 pages
[73] Maymon, P. W. & Chipman, R. A. (1992), Proc. SPIE, 1746, 148
[74] Tang,H., M. Rud, R. Demers, R. Goullioud, et. al. (2015) The WFIRST/AFTA Coronagraph Instrument Design, SPIE 9605 #04 page 5.
[75] McCall' M. W. and C. Paterson (2009) Polarization properties of films in reflection and transmission: a new theorem on polarized light nano-structured thin films. SPIE Proc **7404**-04
[76] Beaudry, N.A., Zhao, Y., and Chipman, R.A., (2007) "Dielectric tensor measurement from a single Mueller matrix image", *JOSA A* 24, 814-824